POLITECNICO DI TORINO

CORSO DI LAUREA MAGISTRALE IN INGEGNERIA AEROSPAZIALE

DIPARTIMENTO DI INGEGNERIA MECCANICA E AEROSPAZIALE

TESI DI LAUREA MAGISTRALE

Numerical simulation of a sub-scale rocket combustor, carried out in the framework of CNES-DLR cooperation

---

Candidato:
Tony DI FABBIO

Relatori:
Prof. Dario PASTRONE
Dr. Victor ZHUKOV (DLR)
Jan VAN SCHYNDEL, M.Sc. (DLR)
Nikolaos PERAKIS, M.sc. (TUM)

Dicembre 2019

"Stay away from negative people. They have a problem for every solution."

Albert Einstein

"Il successo è l'abilità di passare da un fallimento all'altro senza perdere l'entusiasmo."

Winston Churchill

"La vita è un posto meraviglioso"

Anonimo

POLITECNICO DI TORINO

Abstract

Corso di Laurea magistrale in Ingegneria Aerospaziale
Dipartimento di Ingegneria Meccanica e Aerospaziale

Numerical simulation of a sub-scale rocket combustor, carried out in the framework of CNES-DLR cooperation

by Tony DI FABBIO

In recent years, *LOX/CH4* propellant combination has attracted a lot of attention due to various advantages compared to typical *LOX/H2* and *LOX/RP-1* rocket engines. The topic of the present work is to find a fast and reliable method to simulate turbulent and supercritical *LOX/CH4* combustion in a sub-scale combustor using Ansys Fluent. The combustion *EDM* model with a single-step reaction is applied. The turbulence is modelled using a *RANS* approach and the *SST* k-ω model is used for the turbulence closure. In order to account for real gas effects the Soave-Redlich-Kwong (*SRK*) real gas equation of state is employed. A liquid rocket engine operates at high pressures which are very close to the critical pressure of the propellants, where the thermodynamic properties deviate considerably from ideal behaviour. In order to simulate the behaviour of the propellants properly, an analytical study on the thermodynamic and transport properties at inlet condition is conducted.

Negli anni recenti, il motore a razzo a propellenti liquidi *LOX/CH4* ha attirato molte attenzioni dovuti a vari vantaggi rispetto ai tipici motori *LOX/H2* e *LOX/RP-1*. Lo scopo di questo lavoro è trovare un metodo veloce e affidabile per simulare la combustione turbolenta e supercritica tra ossigeno liquido e metano in un modello in scala di una camera di combustione usando Ansys Fluent. Il modello *EDM* di combustione con una singola reazione è applicato. La turbolenza è modellata usando l'approccio *RANS* e il modello *SST* k-ω è usato per la chiusura del sistema di equazioni. Il motore a razzo a propellente liquido opera ad alta pressione, molto vicina a quella critica dei propellenti, dove le proprietà termodinamiche deviano considerevolmente dal comportamento ideale. Per simulare propriamente il comportamento dei propellenti, uno studio analitico sulle proprietà termodinamiche e di trasporto alle condizioni d'iniezione è condotto.

Aufgrund verschiedener Vorteile im Vergleich zu typischen *LOX/H2* und *LOX/RP-1* Raketentriebwerken, erregte die *LOX/CH4* Treibstoffkombination in den letzten Jahren viel Aufmerksamkeit. Das Thema der vorliegenden Arbeit ist es, unter der Verwendung von Ansys Fluent eine schnelle und zuverlässige Methode zur Simulation der turbulenten und superkritischen *LOX/CH4* Verbrennung in einer Modellbrennkammer zu finden. Es wird ein *EDM* Modell mit einem Ein-Schritt Mechanismus angewendet. Zur Turbulenzmodellierung wird ein *RANS* Ansatz verwendet und das *SST* k-ω Modell wird zur Schließung verwendet. Um Realgaseffekte zu berücksichtigen wird die Soave-Redlich-Kwong (*SRK*) Realgasgleichung angewendet. Darüber hinaus arbeitet das Flüssigtreibstofftriebwerk bei hohen Drücken, welche nahe an den kritischen Drücken der Treibstoffe liegen, bei denen die thermodynamischen Eigenschaften beachtlich von dem Idealgasverhalten abweichen. Um das Verhalten der Treibstoffe genau zu simulieren, wird eine analytische Untersuchung der thermodynamischen Eigenschaften und Transporteigenschaften unter Einlassbedingungen durchgeführt.

Acknowledgements

I would like to express my deep gratitude to Dr. Victor Zhukov and Mr. Jan Van Schyndel, my DLR research supervisors, for their patient guidance, enthusiastic encouragement and useful critiques of this research work. Thank you for giving me this fantastic opportunity. It has been an amazing experience. Thank you twice, Jan, for helping me patiently with my English mistakes. I would also like to thank Matthias Dietz, my colleague in our crazy research team.
I would like to express my very great appreciation to Mr. Perakis Nikolaos (my TUM supervisor) for his valuable and constructive suggestions during the planning and development of this research work. His willingness to give his time so generously has been very much appreciated. Thank you to having give me the opportunity to be in DLR. You have suggested me to write my first email asking for master thesis in this special and unique place.
I would like to thanks specially Prof. Dario Pastrone who have accepted to be my supervisor at Politecnico di Torino. In particular, I attended 3 different propulsion courses with your teaching and you have been source of inspiration. I have to thank you if I have decided to continue my academic career with a PhD project.

I would like to thank my family. My parents have always supported me in all my important decisions. *"Grazie, mamma e papà, mi avete sempre dato la forza di continuare questo meraviglioso percorso e non avete mai esitato a supportarmi durante tutte le scelte avventate che mi hanno portato fin qui. Mi avete sempre consigliato di fare la scelta migliore per me, mi avete sempre incoraggiato e mai scoraggiato. Mi avete reso la persona che sono e se tutto questo è stato possibile, è stato anche merito vostro. Ringrazio anche i miei nonni, che tra un piano e l'altro, tra una partenza e l'altra, non hanno mai smesso di starmi vicino per trasmettermi la loro ammirazione e gioia. Ci tengo inoltre a ringraziare mio zio Carmine, soprattutto fonte di ispirazione etica e morale, e fino ad oggi unico ingegnere della famiglia. Zio, da oggi, ti informo che ti tocca condividere il titolo. Vorrei infine chiedere scusa al mio fratellino, scusa per essere un fratello assente, per essermi perso i tuoi anni forse più belli andando via di casa forse troppo presto. Purtroppo, crescendo scelte difficili vanno fatte e vanno affrontate con la massima decisione e concretezza. Sono sicuro che quando toccherà a te, saprai anche tu scegliere la strada migliore. Io sarò qui a supportarti. Ti voglio bene scemo e sempre forza Juve."*

I am also grateful to all my friends who have always supported me along the way. *"Ringrazio innanzitutto la "famiglia Einaudi". Ho incontrato e fatto amicizia con talmente tante persone che è impossibile non dimenticarsi qualcuno. Tutti mi avete donato qualcosa, mi avete insegnato qualcosa che resterà per sempre dentro di me. Ci tengo in particolare a ringraziare il Picchio (Valerio), l'ex Veggy (Beppe), l'Orso (Luca) ed Il Matto El Shaid (Matteo), siete stati una vera famiglia e so di poter contare sempre su di voi. Un ricordo va anche alla famiglia del mio primo collegio torinese "P.Borsellino".*
I would like to mention my Turin Football Team "Il Team Picco". *"Grazie ragazzi, mi avete regalato partite e momenti unici. Le nostre battaglie resteranno sempre con me. Un grazie speciale al capitano, non che mio Amico, Simone. Sei stata una delle prime persone che ho conosciuto a Torino, abbiamo studiato, riso, giocato, condiviso tanto insieme. Sappi che potrai contare sempre sul tuo Muro."*
When I come in Germany, I never thought I'd could meet a family here. *"Grazie mille ILR. Ragazzi e Ragazze, mi mancherete tanto, avete reso anche questo un posto meraviglioso, un po' come la vita direi.*

Finally, I need to thank the most important person in my life. *"No mamma, non sei tu, mi dispiace. Grazie Giorgia, grazie soprattutto per non aver mai tentato di frenarmi, grazie per avermi sempre lasciato libero di decidere cosa fosse migliore per me. Ho fatto tante esperienze, abbiamo superato tante prove e penso che il cammino insieme sia ancora lungo. La vita ci porterà ad affrontare tante altre dure decisioni ma il bello deve ancora venire. Grazie per esserci sempre stata. Ti amo. Il tuo, mio, nostro, Tono"*

Contents

List of Figures

List of Tables

List of Abbreviations

CFD	**C**omputational **F**luid **D**ynamics
DLR	**D**eutsches Zentrum für **L**uft- und **R**aumfahrt
CNES	**C**entre **N**ational d'**E**tudes **S**patiales
RLV	**R**eusable **L**aunch **V**ehicles
EDM	**E**ddy **D**issipation **M**odel
EOS	**E**quation **O**f **S**tate
VdW	**V**and **d**er **W**aals
PR	**P**eng **R**obinson equation of state
SRK	**S**oave **R**edlich **K**wong equation of state
RANS	**R**eynolds **A**veraged **N**avier–**S**tokes equations
FANS	**F**avre **A**veraged **N**avier–**S**tokes equations
CEA	**C**hemical **E**quilibrium **A**pplications
CERFACS	**C**entre **E**uropéen de **R**echerche et de **F**ormation **A**vancée en **C**alcul **S**cientifique
NIST	**N**ational **I**nstitute of **S**tandards and **T**echnology

Physical Constants

Oxygen molar mass	$W_{oxygen} = 32\,\mathrm{g\,mol^{-1}}$
Methane molar mass	$W_{methane} = 16\,\mathrm{g\,mol^{-1}}$
Nitrogen molar mass	$W_{nitrogen} = 3.76\,\mathrm{g\,mol^{-1}}$
Carbon Dioxide molar mass	$W_{CarbonDioxide} = 44\,\mathrm{g\,mol^{-1}}$
Water molar mass	$W_{Water} = 18\,\mathrm{g\,mol^{-1}}$
Gas constant	$R = 8.314\,47\,\mathrm{J\,mol^{-1}\,K^{-1}}$

List of Symbols

ν'_F	moles of fuel	mol
ν'_O	moles of oxidizer	mol
s	stoichiometric ratio	
Φ	equivalence ratio	
ROF	mixture ratio	
W	molar mass	$\mathrm{g\,mol^{-1}}$
Y	mass fraction	
X	mole fraction	
ρ	density	$\mathrm{kg\,m^{-3}}$
p	pressure	Pa
T	temperature	K
V	volume	$\mathrm{m^3\,kg^{-1}}$
$\dot{m}$	mass flow rate	$\mathrm{kg\,s^{-1}}$
c_p	specific heat capacity	$\mathrm{J\,kg^{-1}\,K^{-1}}$
c_p	molar specific heat capacity	$\mathrm{J\,mol^{-1}\,K^{-1}}$
h	mass enthalpy	J
h^m	mole enthalpy	J
e	energy	J
e_t	total energy	J
ΔH_f^o	enthalpy of formation	J
u	x-velocity	$\mathrm{m\,s^{-1}}$
v	y-velocity	$\mathrm{m\,s^{-1}}$
w	z-velocity	$\mathrm{m\,s^{-1}}$
U	mean flow velocity	$\mathrm{m\,s^{-1}}$
u'	root-mean-square turbulent velocity fluctuations	$\mathrm{m\,s^{-1}}$
ω	specific dissipation rate	$\mathrm{s^{-1}}$
k	turbulent kinetic energy	$\mathrm{m^2\,s^{-2}}$
ϵ	rate of dissipation	$\mathrm{m^2\,s^{-3}}$
I	turbulent intensity	%
μ	dynamic viscosity	Pa s
λ	thermal conductivity	$\mathrm{W\,m^{-1}\,K^{-1}}$
D	mass diffusivity	$\mathrm{m^2\,s^{-1}}$
V	diffusion velocity	$\mathrm{m\,s^{-1}}$
$\dot{\omega}$	reaction term	
$\dot{\omega_T}$	heat release	
Q	rate progress of reaction	$\mathrm{mol\,s^{-1}}$
A	pre-exponential constant	
K	forward or reversed constant	
E	activation energy	
T_a	activation temperature	
τ_{ij}	viscous stress	
σ_{ij}	total stress tensor	
q_i	heat flux	
δ_{ij}	Kronecker delta	
z	mixture fraction	
Z	compressibility factor	
Re	Reynolds number	

Re_y	turbulent Reynolds number
Sc_t	turbulent Schmidt number
Pr_t	turbulent Prandtl number
y^+	dimensionless wall distance

Chapter 1

Introduction

The simulation of the methane-oxygen combustion is one of the key-issue in the modern *CFD* study in the field of space transportation. The aim of the current work is the further development and validation of a combustion model to analyse *CH4/LOX* combustion. It consists on searching a fast and reliable method to simulate the behaviour of turbulent and critical combustion. The improvement of the obtained results will be done comparing the achieved results to further *CFD* simulations with different methods and/or software. Moreover, experimental data of the wall combustor temperature will be available. They can be used to verify the reliability of the employed method. The work is part of a collaboration between *DLR* and *CNES*, and it has been carried out at the DLR Institute of Space Propulsion.

Methane has been suggested as a feasible alternative hydrocarbon fuel for liquid rocket engines. It is the lightest and non-toxic hydrocarbon, which has shown advantages over larger hydrocarbons, including higher specific impulse around 370 seconds, better cooling capabilities and lower coking and sooting propensities. It offers the advantage of being a “soft cryogenic” because its vaporization temperature is much higher than that of hydrogen. It is easier to store and imposes fewer insulation and handling concerns. Moreover, the cost to extract methane from nature resource is 5 to 10 times cheaper than that to produce hydrogen. Therefore in the past years, the combustion of liquid oxygen (*LOX*) and gaseous methane (*CH4*) has drawn some attention for the development of high performance reusable launch vehicles (*RLV*) [3]. In this research field, the *LOX/CH4* reusable prototype engine Prometheus ("Precursor Reusable Oxygen Methane Cost Effective propulsion System") is considered as an essential first step towards the very low-cost European space launchers.

Experimental analysis is the conventional way to understand the quality of the design and to entail further improvements; however, it demands huge cost and time as well as manpower to setup such high-pressure combustion facility. With the development of advanced numerical techniques, Computational Fluid Dynamics (*CFD*) is a preferred choice of researchers for such difficult experiments. In fact, *CFD* modelling offers a means to reduce the amount of expensive hot-fire tests. Once validated, the numerical model can be applied to many other cases.

The combustion strongly modifies the flow field. The combustion science is briefly analysed and commented related to the current work in Chapter 2. Complex phenomena occur in turbulent flows: depending on the situation, turbulence may be either reduced or enhanced by flames. The special characteristics of the combustion case study lead to serious numerical difficulties: simulations must handle stiff gradients in temperature, species mass fractions and, accordingly, in velocity field. Because of the complexity of combustion and related phenomena, chemical reactions and fluid flow cannot be solved at the same time using brute force techniques, except in a few academic cases. Modelling and physical insight are required to build computational tools for reacting flows [28]. The variety of approaches for numerical combustion indicates that there is no consensus today on the best path to follow.
Kozubkovaá et al. [4] focused on the creation of the mathematical model of methane turbulent combustion usign Ansys Fluent 13.0 software. The mathematical model for species transfer with chemical reaction is described, where burning is based on stoichiometric equations of perfect combustion.
Sharma et al. [3] numerically investigated *CH4/LOX* combustion in a full-scale 120-element shear coaxial thrust chamber. In order to account for real gas effects *SRK* real gas equation of state is employed. The combustion is analysed with a non-premixed non-adiabatic steady

flamelet model and the *SST* k-ω model is used for the turbulent closure of the FANS equations.
Dr. Zhukov [40] focused on a *GO2/GH2* combustion chamber with a single shear coaxial injector. The turbulent flow in the combustion chamber is modelled using the *FANS* equations and the *SST* model for turbulence closure. The turbulent non-premixed flame is modelled using an extended eddy dissipation model.

To enhance the performance of liquid propellant rocket engine, combustion occurs in a high-pressure combustion chamber. Therefore, most of the future methane rocket engines under development could be operated at the supercritical pressure much higher than the critical pressure of oxygen (50.43 bar) and methane (45.99 bar). If pressure and temperature are above the thermodynamic critical points of one or both propellants, the combustion process is strongly influenced by the reactants behaviour. Near the critical point surface tension and enthalpy of vaporization are small and the interface separating the liquid and gas phases disappears. All these aspects produce some challenges in the development of the most appropriate mathematical models for the numerical simulations [3]. For this reason, a study is conducted on the thermodynamic and transport properties of the reactants at inlet condition in Chapter 4.

In the current work the commercial software Ansys Fluent 19.2 has been utilized. Programmes in the Ansys package are used to build the geometries and the meshes of injectors and combustor. Injectors and combustion chamber have been simulated in two different simulations. They have been coupled through the velocity profiles coming out of the injectors and imported in the combustion chamber. Most practical flames involve turbulent flow fields. Simulating turbulent combustion is a very complex challenge because various length and time scales must be taken into account, both to describe turbulent motions and chemistry (flame thicknesses and speed). The turbulent combustion of propellants in a non-premixed flames has been modelled using the *EDM* (Eddy-Dissipation Model) with a single-step reaction. The turbulence is modelled using a *RANS* approach and the *SST* k-ω model is used for the turbulence closure. The Ansys Fluent setup and the meshes are presented in Chapter 3.

Chapter 2

Combustion Science

Nowadays, 90% of energy is produced by combustion. For many reason, a world without combustion is unimaginable. If hypothetically combustion should stop tomorrow we would not have the energy for the entire society. In any case, it is very important to keep everything under control and manage the power of the chemical reactions. In rocket science, the combustion is essential and understanding its behaviour in profundity is one of the most important challenge for the future space exploration.

One of the main challenges regarding the combustion are surely the pollutants. Hydrocarbons C_nH_m are often burned and the following general reaction occurs:

$$C_nH_m + O_2 \rightarrow CO_2 + H_2O + (C_xH_y + CO + NO + soot + etc)$$

When hydrocarbons are burned carbon dioxide and water cannot be avoided (main products of the chemical reaction) but the other products, the pollutants, can be avoided. The reaction of the ideal combustion in Fig. 2.1 is the perfect one, with maximum efficiency and no presence of pollutants, that may be reached ideally.

FIGURE 2.1: Ideal Combustion Reaction

Various coupling mechanisms occur in combusting flow fields. The combustion science is composed by multiple sciences or research fields, as illustrated in Fig. 2.2, which make the combustion study unique and challenging.

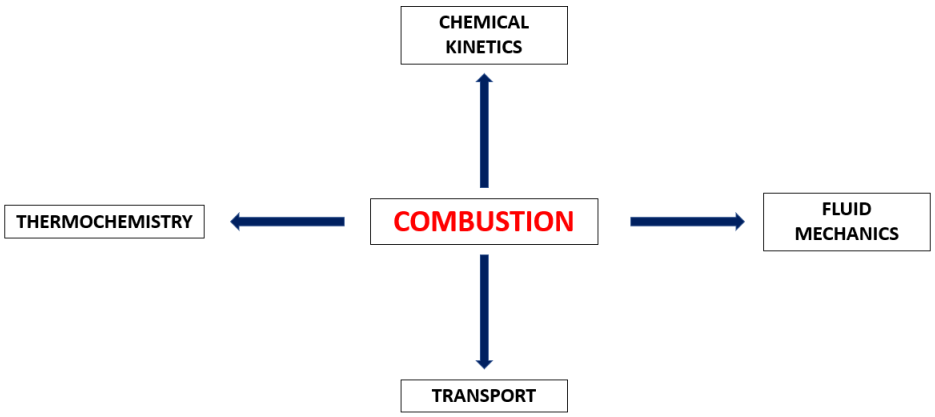

FIGURE 2.2: Multiple Research Fields

Each research field will be briefly explained to understand what it analyses. This part is very important to know what there is behind the commercial program applied in the development of the current work.

Thermochemistry Methane/pure oxygen (or air considering the nitrogen presence) combustion is treated. The main reaction in Eq. 2.1 is analysed in order to explain the main topic of the thermochemistry.

$$CH_4 + 2(O_2 + 3.76N_2) \rightarrow CO_2 + 2H_2O + 2 \cdot 3.76N_2 \tag{2.1}$$

The nitrogen does not react but it is present in the combustion reaction if air and not pure oxygen is injected. In the present project, pure liquid oxygen (LOX) is considered but sometimes particle of nitrogen are dissolved in the liquid oxygen caused by the conservation, storability method [33]. In any case, the nitrogen is not eliminated from the simulations and, as it will be explained in Section 2.3.3, it operates like a "bulk" quantity.

The global reaction equation without consider the presence of nitrogen is written as follows:

$$CH_4 + 2O_2 \rightarrow CO_2 + 2H_2O \tag{2.2}$$

The stoichiometric reaction occur when 1 mole of methane reacts with 2 moles of oxygen, but what happens if less or more than 1 mole of methane for 2 moles of oxygen are present?

- If less than 1 mole of CH_4 reacts with 2 moles of O_2, there is oxygen left in the products because there is not enough methane to burn all the oxygen. This case is called *Lean Combustion*.
- The so-called *Rich Combustion* takes place when more than 1 mole of CH_4 reacts with 2 moles of O_2. Unburnt hydrocarbons are left (CO too usually) because too much methane is present within the reactants. Generally, lean is better than rich because fuel is expensive and less pollutants are produced.

The thermochemistry describes only the initial and the final states. It is totally independent of the speed at which the reaction goes from the initial to the final state. One typical application is the *adiabatic flame temperature* computation that will be exposed in Section 2.2.

Chemical Kinetics The chemical kinetics studies the speed at which chemical reactions proceed. The reaction in Eq. 2.2 is discussed but the interest is focused on how much time this reaction needs to proceed.

In order to compute the correct value of the reaction rate, the intermediate reactions, behind the stoichiometric one, need to be taken into account. In the global reaction (Eq. 2.2) only the initial reactants and the final products are present. Therefore, it is possible to analyse only initial and final steps globally. In reality, between the products formation and the initial reactants many things happen and many species are created and consumed. These species that do not appear within the global reaction are called intermediate species. The reactions that describe these intermediate phenomena are called intermediate reactions [14]. Most of them take place in the flame front, as illustrated in Fig. 2.3.

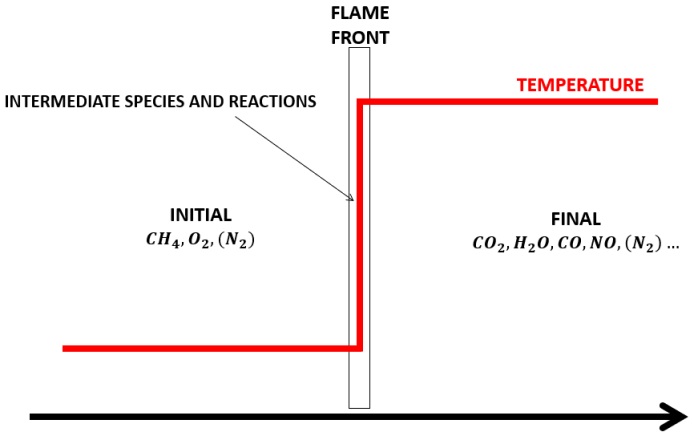

FIGURE 2.3: Location of Intermediate Species and/or Reactions

The most common tool to analyse the chemical kinetics is called *Chemkin*. It is a robust and mature chemistry simulation tool that has been used for a wide range of applications. *Chemkin* is a "cost-effective" solution for basic kinetics simulations that use small or reduced reaction mechanisms. It solves thousands of reactions combinations to develop a comprehensive understanding of a particular process, which might involve multiple chemical species, concentration ranges, and gas temperatures [8].
In the current work, as anticipated in Chapter 1, the *EDM* model with a single step reaction is applied to analyse the combustion. For this reason, *Chemkin* software will not be used, and how the chemical kinetics is taken into account will be explained in Section 3.1.2.

Transport and Equation of State Transport description is a specific issue for reacting flows: the thermal conductivity λ, the dynamic viscosity μ and the molecular diffusion coefficients must be specified for multispecies gases. Mass transfers of chemical species by molecular diffusion, convection and turbulent transport are also an important ingredient. The heat released by chemical reactions induces strong conductive, convective or radiative heat transfer inside the flow and with the surrounding walls [28].

The combustion process is governed by almost the "same equations" that describe the common aerodynamics, the so-called Navier-Stokes equations. However, the combustion is more complicated. The reactants burn and after many reactions (chemical kinetics) the products will be partially or totally formed. At high pressure and/or temperature conditions, the reactions will not proceed to 100%. During this process, the gas composition will change and it has to be taken into account. Therefore, the mass fraction of the N species present in the gas need to be computed, and the continuity species equations have to be considered.

Regarding the equations of state, the discussion will be profoundly developed in Chapter 4, where it will be explained why real gas effects are important and how it is difficult to model them in the simulations.

Fluid Mechanics and Mixing Gaseous combustion also requires the description of the flow field. The organization of the fluid in the chamber is determined by the mixing that derives from the laws of the fluid mechanics.

One important aspect of the combustion are the regimes. The regimes depend on how fuel and oxidizer are mixed and they are directly consequence of the flow field characteristics in the combustor. To first order flames can be[28]:

1. premixed or non-premixed;
2. laminar or turbulent;
3. stable or unstable.

Regarding the difference between premixed and non-premixed, the main characteristics of the two regimes can be differentiate as follows:

- *Premixed*
  - the most efficient
  - the most dangerous (bomb)
  - the least amount of pollutants

  First the reactants are taken, mixed and then the mixture is ignited when everything is ready. This method is very efficient but also very dangerous (just needs a spark to initiate the combustion).

- *Diffusion or non-premixed* (Section 2.4)
  - less efficient
  - less dangerous
  - more pollutants

The reactants are kept separately in different tanks, then at the last time they are mixed and burned simultaneously. This method is not the most efficient method but it is applied on the rocket engines for safety reasons.

The effect of the turbulence is another aspect of the combustion that should be taken into account. Turbulent or laminar flames can be generated . Most practical flames correspond to turbulent flows: turbulence enhances combustion intensity and allows the design of smaller burners. It also increases the modelling difficulties by orders of magnitude. For example, if the injected gases are turbulent, the flame will be too. The flame does not remain flat and the vorticity's effects becomes crucial. Moreover, the turbulence's effect generates a close loop because the vorticity gives more power to the fluid , the mass flow increase, the flow becomes more turbulent and the flame too. For this reason, the turbulence model is very important and different methods are available in literature. The turbulent viscous model will be treated in Section 2.3.5 and the choice of using the $SST\ k-\omega$ model will be explained in detail.

2.1 Combustion Terminology

The global reaction in Eq. 2.2 is considered and, in general terms, it can be written as follows:

$$\nu'_F F + \nu'_O O \rightarrow P, \tag{2.3}$$

where ν_F moles of fuel (methane) and ν_O moles of oxidizer (oxygen) react and generate products P (carbon dioxide and water vapor).

Some definitions and variables need to be introduced [28]:

- Stoichiometric Ratio (the perfect amount of oxygen to burn fuel)

$$s = \frac{\nu'_O W_O}{\nu'_F W_F} = \left(\frac{Y_O}{Y_F}\right)_{st} \tag{2.4}$$

  For a rocket engine that burns oxygen and methane, 2 moles of O_2 are necessary to burn 1 mole of CH_4 at stoichiometric condition. Therefore, a mixture of CH_4 and O_2 at stoichiometric condition is composed by 20% of methane and 80% of oxygen.

- Equivalence Ratio: what is truly present divided by what should be present at stoichiometry

$$\Phi = \frac{\frac{Y_F}{Y_O}}{\left(\frac{Y_F}{Y_O}\right)_s} = s \cdot \frac{Y_F}{Y_O} \tag{2.5}$$

  The Mixture Ratio (ROF) is the definition of what is truly present in the combustor

$$ROF = MR = \frac{Y_F}{Y_O} \tag{2.6}$$

In a multispecies gas it is very important to consider the effect of each single species. For this reason, some definitions for each species k are mentioned.

- Atomic Weight W_k
- Mass Fraction of species k: mass of species k divided by total mass

$$Y_K = \frac{m_k}{m} = \frac{m_k}{\sum_{k=1}^{N} m_k} \tag{2.7}$$

- Mole Fraction of species k: moles of species k divided by total moles

$$X_k = \frac{N_k}{N} \tag{2.8}$$

- Partial Density
$$\rho_k = \rho Y_k = m_k / V \tag{2.9}$$

- Partial Pressure (each species follows perfect gas law)
$$p_k = \rho_k \frac{R}{W_k} T \tag{2.10}$$

- Heat Capacity of species k
$$c_{p_k} \tag{2.11}$$

- Mole Heat Capacity of species k
$$c^m_{p_k} = c_{p_k} \cdot W_k \tag{2.12}$$

  In combustion science, when high temperatures are involved, it needs to be considered that c_{p_k} varies with temperature, as it will be explained in Chapter 4.

- Enthalpy of species k
$$h_k = \Delta H^0_{f,k} + \int_{T^0}^{T} c_{p_k} dT, \tag{2.13}$$

  where, $\Delta H^0_{f,k}$ is the enthalpy of formation of the species k at temperature T^0 and the integral part is the enthalpy needed to get from T^0 to T, the so-called sensible enthalpy[1].

- Molar Enthalpy of species k
$$h^m_k = h_k \cdot W_k = \Delta H^o_{f,k} \cdot W_k + \int_{T^o}^{T} c_{p_k} \cdot W_k dT = \Delta H^{o,m}_{f,k} + \int_{T^o}^{T} c^m_{p_k} dT \tag{2.14}$$

  The atomic weight, the mass and molar enthalpy of formation of single species k involved in the global reaction (Eq. 2.2) are shown in Tab. 2.1.

	$W_k \quad (kg/mol)$	$\Delta H^o_{f,k} \quad (kJ/kg)$	$\Delta H^{o,m}_{f,k} \quad (kJ/mol)$
CH_4	0.016	-4675	-74.8
O_2	0.032	0	0
H_2O	0.018	-13435	-241.8
CO_2	0.044	-8943	-393.509

TABLE 2.1: Atomic Weight and Enthalpy of Formation

In order to connect the thermodynamic variables with each other, the equation of state (EOS) has to be taken into account. In particular, to simplify the following computations, the Ideal EOS is considered and it is written as follows:

$$p_k = \rho_k R^* T, \tag{2.15}$$

where $R^* = R/W_k$, R is the gas constant and W_k is the atomic weight of the single specie. It becomes more complicated for the combustion case when a multispecies gas is considered.

After having introduced the variables for the single species k, mixing rules need to be defined. Therefore, the following variables are referred to the mixture (multispecies gas) [28]:

- Density (the sum of partial densities expressed in Eq. 2.9)
$$\rho = \sum_{1}^{N} \rho_k \tag{2.16}$$

[1] Note that if c_{p_k} is constant and enthalpy of formation is null, $h_k = c_p T$.

- Pressure (the sum of partial pressures expressed in Eq. 2.10)

$$p = \sum_{1}^{N} p_k \tag{2.17}$$

- Temperature T (the same everywhere)
- $p = \rho R^* T$ (ideal gas assumption also for the mixture) where $R^* = R/W$ and $W = \sum_1^N W_k X_k$ is the average molar mass of the mixture.
- Mass Enthalpy of the mixture (from Eq. 2.13)

$$h = \sum_{1}^{N} h_k Y_k \rightarrow h = \sum_{1}^{N} \Delta H^o_{f,k} Y_k + \int_{T^o}^{T} \sum_{1}^{N} (c_{p_k} Y_k) dT \tag{2.18}$$

  where $\sum_1^N (c_{p_k} Y_k)$ is the heat capacity of the mixture (average)

- Mole Enthalpy of the mixture $h^m = h \cdot W$ (from Eq. 2.14)

$$h^m = \sum_{1}^{N} h^m_k X_k \rightarrow h = \sum_{1}^{N} \Delta H^{o,m}_{f,k} X_k + \int_{T^o}^{T} c^m_p X_k dT \tag{2.19}$$

2.2 Adiabatic Flame Temperature

Different computational methods of the adiabatic flame temperature will be presented. The global reaction (Eq. 2.2) links the fresh reactants to the burnt gases or products (Fig. 2.4).

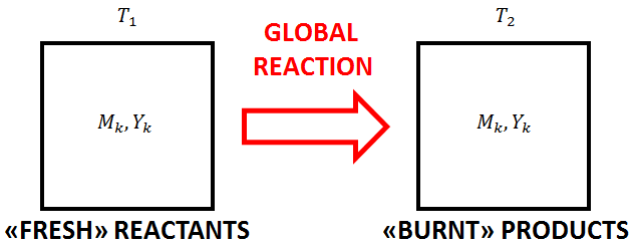

FIGURE 2.4: Global Reaction

If all the species involved in the reaction are written both in reactants and products side, Eq. 2.2 can be reformulated as follows:

$$CH_4 + 2O_2 + 0CO_2 + 0H_2O \rightarrow 0CH_4 + 0O_2 + CO_2 + 2H_2O \tag{2.20}$$

and, in general terms,

$$\sum \nu'_k M_k \rightarrow \sum \nu_k'' M_k$$

The global mole number is introduced as follows (product less reactants):

$$\nu_k = \nu_k'' - \nu'_k \tag{2.21}$$

ν_k is the balance of Eq. 2.20 and tells us what it is gained (+) and/or lost (-) due to the reaction.

Remembering that a deflagration combustion is under analysis, the pressure can be considered almost constant and the total enthalpy is conserved ($H(T_1) = H(T_2)$). The total enthalpy of reactants is equal to the total enthalpy of the product even if temperatures (T_1 and T_2) are different [2].

Recalling the definition of molar enthalpies of a single species k (Eq. 2.14), the total enthalpy for reactants and products can be written as follows:

$$H(T_1) = \sum_1^N \nu_k' \left(\Delta H_{f,k}^{0,m} + \int_{T^0}^{T_1} c_{p_k}^m dT \right)$$

$$H(T_2) = \sum_1^N \nu_k'' \left(\Delta H_{f,k}^{0,m} + \int_{T^0}^{T_2} c_{p_k}^m dT \right)$$

Considering the previous assumption $H(T_1) = H(T_2)$,

$$\sum_1^N \nu_k'' \int_{T^0}^{T_2} c_{p_k}^m dT - \sum_1^N \nu_k' \int_{T^0}^{T_1} c_{p_k}^m dT = \sum_1^N \left(\nu_k' - \nu_k''\right) \Delta H_{f,k}^{0,m} \tag{2.22}$$

the *molar heat of reaction* Q_m can be introduced as follows:

$$Q_m = \sum_1^N (\nu_k' - \nu_k'') \Delta H_{f,k}^{0,m} = -\sum_1^N \nu_k \Delta H_{f,k}^{0,m} \tag{2.23}$$

Q_m is equal to the sensible enthalpies of reactants less the sensible enthalpies of products. Each species k has the molar enthalpy of formation $\Delta H_{f,k}^{0,m}$ and the reaction has the molar heat of reaction Q_m as a function of the previous one [2].

Taking the global reaction in Eq. 2.2 into account, Q_m can be computed as follows:

$$Q_m = +1\Delta H_{f,k}^{o,m}(CH_4) + 2\Delta H_{f,k}^{o,m}(O_2) - 1\Delta H_{f,k}^{o,m}(CO_2) - 2\Delta H_{f,k}^{o,m}(H_2O) \rightarrow$$

$$\rightarrow Q_m = 951.909 \quad KJ/mol$$

951.909 kJ are realised each time 1 mole of methane is burned. Considering that 241 kJ are obtained each time 1 mole of hydrogen is burned, it seams that it is more convenient to burn methane. But, in reality, the *heat of reaction per unit mass* Q

$$Q = \frac{Q_m}{W_F} = \frac{951.909 \cdot 10^3}{0.016} = 59.49 \quad MJ/kg$$

shows that 59.49 MJ are produced each time 1 kg of methane is burned in respect to 120 MJ using hydrogen. So, with equal mass, it is more convenient to burn hydrogen because more energy is obtained. However, as said in the introduction Chapter 1, the interest of burning methane are multiple and it is essential to understand the behaviour of methane during the combustion process.

The adiabatic flame temperature can be computed with 3 different methods [2]:

1. Approximate "*by hand*"

   Assuming that $c_{p_k}^m$ does not change with temperature, Eq. 2.24 is derived from Eq. 2.22 to compute easily the adiabatic flame temperature

   $$T_2 = T_0 + \frac{\sum_1^N \nu_k' c_{p_k}^m (T_1 - T_0) + Q_m}{\sum_1^N c_{p_k}^m} \tag{2.24}$$

   Eq. 2.24 is correct if T is not large. If T changes a lot, the equation is completely wrong because a bad assumption on $c_{p_k}^m$ is done and the simple obtained results are often not acceptable.

2. *Tables*: a better method is to ignore T and work directly with the sensitive enthalpies

   $$H_s = \int_{T^o}^{T} c_{p_k}^m dT \qquad tabulated\ value$$

Recalling Eq. 2.22 and using the definition of H_s, Eq. 2.25 is derived as follows:

$$H_s(T_2)^2 - H_s(T_0)^2 = H_s(T_1)^1 - H_s(T_0)^1 + Q_m, \tag{2.25}$$

where T_1 (reactants initial temperature) is known and $H_s(T_1)^1$ is extracted from the tables. It is the same for $H_s(T_0)$ (reference temperature of both products and reactants). Moreover, Q_m was computed previously from Eq. 2.23, and $H_s(T_2)^2$ can be calculated from Eq. 2.25. Finally, T_2 is obtained from the tabulated tables. From literature [30], it can be found that $T_2 \approx 5000$ at stoichiometric condition.

3. *Numerical Codes*: for example CEA-nasa code [7] or CERFACS code [1]

$$T_2 = 3594.63k \quad CERFACS$$

$$T_2 = 3549.76k \quad CEA(LOX)$$

$$T_2 = 3579.44k \quad CEA(O2)$$

It is important to take the value obtained into account because it can be used for an extended EDM model in Ansys Fluent, as it will be explained talking about the possible outlooks in Chapter 5.

The numerical codes know all the species, all the reactions, not only the global reaction in Eq. 2.2. For this reason the adiabatic flame temperature is lower in respect to the other methods. In others words, the codes are aware of the chemical kinetic and they take the possible intermediate reactions and species that are behind the global one into account. The real phenomena that takes place in these conditions is the so-called *dissociation*. In fact, for example, the products of the *CH4/LOX* combustion are not only water and carbon dioxide as they are also broken into other molecules. When the *dissociation* appears, the temperature goes down because this phenomena consumes energy. This phenomena is not present when T is lower than $2500K$ and for this reason it does not appear if air combustion is studied (first two methods are fine). The third method (code) is really necessary when pure oxygen combustion is analysed ($T_2 > 2500K$) and one needs to consider all species.

2.3 Conservation Equations for Combustion

The governing equations for combustion are more complex than those used in classical aerodynamics. The general equations for a fluid flow, the so-called Navier-Stokes equations, plus the extension for combustion are presented. The Navier-Stokes equations are the basis of the FANS equations, exposed in Section 3.1.1, that are implemented and solved in Ansys Fluent.

By stepping back, if an aerodynamic case is analysed, just 5 variables are present

$$u_i \rightarrow 3\ velocities,\ \ \rho,\ \ p\ \ (or\ \ h,\ \ T,\ \ e)$$

and, for this reason, 5 equations are requested: continuity (1 scalar Eq. 2.3.1), momentum (1 vectorial Eq. 2.3.2 of 3 dimensions) and energy (1 scalar Eq. 2.3.4). Then the equation of state is fundamental for the closure of the equations system.
As said before, considering a combustion test case, an additional factor must be taken into account: the *composition* (Y_k, N variables/species and N species continuity equations). Therefore, 5 + N variables are present and 5 + N equations are necessary: N - 1 continuity species equations (Eq. 2.31) and one additional equation to compute the composition of the "bulk" quantity (Eq. 2.32).

In general, the equations controlling reacting flows differ from the usual conservation equations used for example for aerodynamics in various aspects[28]:

- since chemistry involves transforming species into other species, one additional conservation equation must be written for each species of interest. Furthermore, in each new conservation equation, source terms must be added to describe the evolution of species through chemical reactions;

- since the flow contains multiple species and large temperature differences, thermodynamical data, state equation and transport models must handle the full equations required for a multispecies mixture.

In order to write the equations, a simple infinitesimal volume in the combustion chamber is considered and mass, momentum and energy are conserved in the domain [15], illustrated in Fig. 2.5.

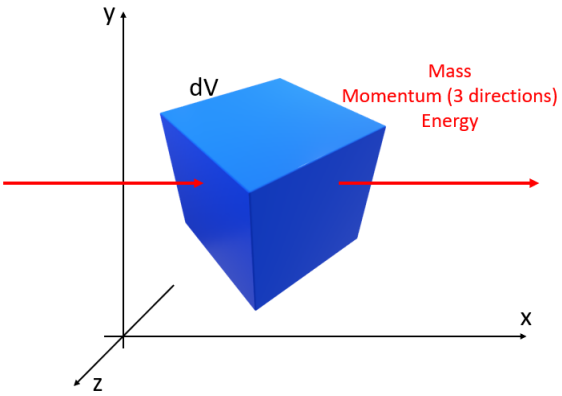

FIGURE 2.5: Infinitesimal Volume

2.3.1 Continuity

The law or principle of mass conservation is expressed in Eq. 2.26 [10].

$$\frac{\partial \rho}{\partial t} + \nabla(\rho u) = 0 \rightarrow \frac{\partial \rho}{\partial t} + \frac{\partial}{\partial x_i}(\rho u_i) = 0 \tag{2.26}$$

After some mathematical reformulation, Eq. 2.27 with total derivative is derived

$$\frac{D\rho}{Dt} = -\rho \frac{\partial u_i}{\partial x_i} \rightarrow \frac{D\rho}{Dt} = -\rho \nabla \cdot u \tag{2.27}$$

2.3.2 Momentum

Eq. 2.28 follows the conservation law of momentum. The difference between the momentum that leaves and enters into the domain is given by the viscous stress force into the fluid.

$$\frac{\partial}{\partial t}(\rho u_i) + \frac{\partial}{\partial x_j}(\rho u_i u_j) = -\frac{\partial p}{\partial x_i} + \frac{\partial \tau_{ij}}{\partial x_j} \rightarrow \rho \frac{Du_i}{Dt} = \frac{\partial \sigma_{ij}}{\partial x_i} \quad i = 1,2,3 \tag{2.28}$$

Where τ_{ij} is the *viscous stress* defined as follows:

$$\tau_{ij} = -\frac{2}{3}\mu \frac{\partial u_i}{\partial x_i}\delta_{ij} + \mu \left(\frac{\partial u_i}{\partial x_j} + \frac{\partial u_j}{\partial x_i} \right) \tag{2.29}$$

Moreover, the *total stress tensor* for Newtonian fluids is expressed as follows:

$$\sigma_{ij} = \tau_{ij} - p\delta_{ij} \tag{2.30}$$

where $\mu = \rho\nu$ is the dynamic viscosity, ν the kinematic viscosity and δ_{ij} the Kronecker symbol [28].

2.3.3 N-1 Species Equations

In order to study a combustion case, the composition of the fluid is crucial. The N-1 continuity equations of each single specie are written as follows:

$$\frac{\partial}{\partial t}(\rho Y_k) + \nabla(\rho(u_i + V_k)Y_k) = \dot{\omega}_k \tag{2.31}$$

In Eq. 2.31 many important terms and effects are found: mass of the single species is changing in time (ρY_k), flux, diffusion transport and production term.

Just N-1 species equations need to be computed because, remembering that

$$\sum_{k=1}^{N} Y_k = 1,$$

it is possible to find Y_N as follows:

$$Y_N = 1 - \sum_{k=1}^{N-1} Y_k \tag{2.32}$$

The N-specie is the so-called "bulk" quantity (nitrogen in the current work) in Ansys Fluent EDM model setup and its concentration is found knowing the concentration of the other species from the N-1 species continuity equations (Eq. 2.31).

Molecular Transport

V_k is the *diffusion velocity* related to the molecule process; molecules collide with each other and diffuse. This effect can be computed considering the kinetic theory. The molecular diffusion transport of the species k is described by the three components $V_{k,i}$ of the diffusion velocities V_k [28]. When pressure is constant (deflagration assumption) and the volume forces are negligible, the determination of the V_k's requires the inversion of the diffusion matrix:

$$\Delta X_p = \sum_{k=1}^{N} \frac{X_k X_p}{D_{kp}}(V_k - V_p) \tag{2.33}$$

where $D_{pk} = D_{kp}$ is the binary mass diffusion coefficient of species p into species k and X_k is the mole fraction of species k [28]. Moreover, if only two species are taken into account, Eq. 2.33 simplifies to *Fick's law* and Eq. 2.34 is derived

$$V_1 Y_1 = -D_{12} \nabla Y_1 \tag{2.34}$$

However, analysing the combustion, more than 2 species are involved and in the codes an extension of Fick's law is implemented:

$$V_k X_k = -D_k \nabla X_k, \tag{2.35}$$

where D_k is the diffusion coefficient of k in the mixture and not in a single species [15].

Production or Reaction Term

The term $\dot{\omega}_k$ in Eq. 2.31 contains the reaction's effect expressed in Fig. 2.6. For example, in one cell CH_4 and O_2 can enter but CO_2 and H_2O can leave because the reaction has taken place.

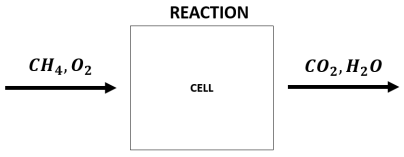

FIGURE 2.6: Cell Reaction

In general, a flow in which N species reacting through M reactions is considered. A way to count what is going on is needed. The reaction in Eq. 2.36 (j=1,..,M) can occur in both directions depending on temperature (dissociation phenomenon)

$$reactants \Longleftrightarrow products \rightarrow \sum_{1}^{N} \nu'_{kj} M_k \Longleftrightarrow \sum_{1}^{N} \nu_{kj}'' M_k \tag{2.36}$$

The reaction effect $\dot{\omega}_k$ is the sum of $\dot{\omega}_{kj}$, analysed for all the involved reactions. One needs to evaluate what is produced inside the different reactions to understand the global effect [14].

$$\dot{\omega}_k = \sum_{1}^{M} \dot{\omega}_{kj}$$

In the current work, since a single-step reaction is considered, $M = 1$ and $\dot{\omega}_k = \dot{\omega}_{kj}$ $(j \equiv 1)$. $\dot{\omega}_{kj}$ is the balance of species k in reaction j and, more in detail, can be written as follows:

$$\dot{\omega}_{kj} = Q_j W_k \nu_{kj} \tag{2.37}$$

$Q_j[moles/s]$ is the *rate progress of reaction j* and Eq. 2.38 shows the speed of reaction and the direction (left to right or right to left, products or reactants are produced or consumed respectively).

$$Q_j = K_j^{(f)} \Pi_k \left(\frac{\rho Y_k}{W_k} \right)^{\nu'_{kj}} - K_j^{(r)} \Pi_k \left(\frac{\rho Y_k}{W_k} \right)^{\nu_{kj}''} \tag{2.38}$$

N_k is the number of moles per volume and $K_j^{(f)}$, $K_j^{(r)}$ are forward and reverse constant linked to the rate of reaction in one direction or the other.
$K_j^{(f)}$ and $K_j^{(r)}$ can be found from Eq. 2.39

$$K_j^{(f)} = A_j^{(f)} T^{\beta_j} e^{-\frac{E_j}{RT}} = A_j^{(f)} T^{\beta_j} e^{-\frac{T_{aj}}{T}}, \tag{2.39}$$

where $A_j^{(f)}$ is the pre-exponential constant, E_j the activation energy (or the activation temperature $T_{aj} = E_j/R$) and β_j the temperature exponent [2] [14]. In order to find the reverse reaction constant, the *equilibrium constant* (Eq. 2.40) can be used

$$K_C = \frac{K_j^{(f)}}{K_j^{(r)}} \tag{2.40}$$

The production term $\dot{\omega}_k$ will be further explained in Section 3.1.2, where it will be contextualized to the Eddy-Dissipation-Model used in Ansys Fluent ($\dot{\omega}_k$ will be mentioned as $R_{i,r}$).

2.3.4 Energy

The energy balance equation may take various forms depending whether the variable chosen for numerical resolutions is the energy (e), the enthalpy (h) or the temperature (T) and whether the formation enthalpy is included or not [28]. Tab. 2.2 summarises their different definitions based on what kind of variable is used.

	Enthalpy	Energy
sensible	$h_s = \int_{T^0}^{T} c_p dT$	
sensible+chemical	$h = \sum_{k=1}^{N} h_k Y_k$	$e = h - p/\rho$
total		$e_T = e + \frac{1}{2} u_i^2$

TABLE 2.2: Energy Equation Variables

[2] The *Chemkin* format for the chemical scheme of the reaction contains these factors too. For each forward reaction, these three parameters must be specified.

All the different forms are derived from the equation of the *total energy* e_t

$$\rho \frac{D}{Dt} e_t = -\frac{\partial}{\partial x_i} q_i + \frac{\partial}{\partial x_j}(\sigma_{ij} u_i), \tag{2.41}$$

where σ_{ij} is the total stress tensor (Eq. 2.30) and q_i the *heat flux* expressed as follows:

$$q_i = -\lambda \frac{\partial T}{\partial x_i} + \rho \sum_{k=1}^{N} Y_k h_k V_{k_i} \tag{2.42}$$

Eq. 2.42 is the sum of Fourier's law and an additional term for combustion, the species are diffusing and also coupling its own enthalpies.
Eq. 2.43 of the kinetic energy $\left(\frac{1}{2} u_i^2\right)$ has to be derived from the Eq. 2.28.

$$\rho \frac{D}{Dt}\left(\frac{1}{2} u_i^2\right) = u_i \frac{\partial}{\partial x_j} \sigma_{ij} \tag{2.43}$$

Then, it is possible to find Eq. 2.44 of energy $e = e_t - \frac{1}{2} u_i$ (sensible + chemical) [10],

$$\rho \frac{De}{Dt} = -\frac{\partial}{\partial x} q_i + \sigma_{ij} \frac{\partial u_i}{\partial x_j}, \tag{2.44}$$

and consequently Eq. 2.45 of enthalpy $h = e + p/\rho$

$$\rho \frac{Dh}{Dt} = -\frac{Dp}{Dt} - \frac{\partial}{\partial x_i} q_i + \tau_{ij} \frac{\partial u_i}{\partial x_j} \tag{2.45}$$

Eq. 2.46 of sensible enthalpy ($h = h_s + \sum_1^N \Delta H^o_{f,k} Y_k$) is derived from Eq. 2.45 as follows:

$$\rho \frac{Dh_s}{Dt} = \frac{\partial}{\partial x_i}\left(\lambda \frac{\partial T}{\partial x_i}\right) - \frac{\partial}{\partial x_i}(\rho \sum_1^N h_{s,k} Y_k V_{k_i}) + \tau_{ij} \frac{\partial u_i}{\partial x_j} + \frac{Dp}{Dt} + \dot{\omega}_T, \tag{2.46}$$

where $\dot{\omega}_T$

$$\dot{\omega}_T = -\sum_1^N \Delta H^o_{f,k} \dot{\omega}_k \tag{2.47}$$

is the heat release in the global reaction. The species source terms due to chemical reactions $\dot{\omega}_k$ induce a heat release term defined by $\dot{\omega}_T$. N reaction rates for each species are present but only one global heat release that generates the temperature increase.
In order to see directly the effects of the heat release (Eq. 2.47) on the temperature field, Eq. 2.48 of temperature is written as follows

$$\rho c_p \frac{DT}{Dt} = \frac{\partial}{\partial x_i}\left(\lambda \frac{\partial T}{\partial x_i}\right) + \frac{Dp}{Dt} + \tau_{ij} \frac{\partial u_i}{\partial x_j} - \frac{\partial T}{\partial x_i} \rho \sum_1^N V_{k_i} Y_k c_{p_k} + \dot{\omega}'_T \tag{2.48}$$

where one can find the heat flux given by diffusion, pressure term, power of viscous stress, the problem of diffusion velocity and the reaction term [10]. In this case the reaction term becomes

$$\dot{\omega}'_T = -\sum_1^N (\Delta H_{f,k} + h_{s,k}) \dot{\omega}_k$$

Eq. 2.48 is the general equation which gives the temperature of any flame (considering assumptions).

2.3.5 Viscous Model SST

The SST $k - \omega$ model is one of the most commonly used models. This includes two additional transport equations to represent the turbulent properties of the flow. In fact, it is an

empirical model based on model transport equations for the turbulence kinetic energy (k) and the specific dissipation rate (ω), which can also be thought of as the ratio of ϵ to k, where ϵ is rate of dissipation of turbulence energy. The transport variable k determines the energy in turbulence and ω determines the scale of turbulence [35]. The specific turbulence dissipation (ω) is the rate at which turbulence kinetic energy is converted into thermal internal energy per unit volume and time. Sometimes ω is also referred to as the mean frequency of the turbulence [34].

There is no strict mathematical definition of the specific turbulence dissipation, ω. Instead it is most often defined implicitly using the turbulence kinetic energy (k) and the turbulence dissipation (ϵ) as follows [35]:

$$\omega = \frac{\epsilon}{k\beta^*},$$

where β^* is a model constant, most often set to:

$$\beta^* = C_\mu = 0.09$$

The turbulent energy k is given by:

$$k = \frac{3}{2}(UI)^2, \tag{2.49}$$

where U is the mean flow velocity and I is the turbulence intensity. The turbulence intensity gives the level of turbulence and it can be defined as follows:

$$I = \frac{u'}{U}, \tag{2.50}$$

where u' is the root-mean-square of the turbulent velocity fluctuations [35]. The root-mean-square of the turbulent velocity fluctuations is given as:

$$u' = \sqrt{\frac{1}{3}\left(u_x'^2 + u_y'^2 + u_z'^2\right)} = \sqrt{\frac{2}{3}k} \tag{2.51}$$

The mean velocity U can be calculated as follows:

$$U = \sqrt{U_x^2 + U_y^2 + U_z^2} \tag{2.52}$$

The turbulent intensity at the core of a pipe for a fully developed pipe flow can be estimated as follows:

$$I = 0.16 Re_{d_h}^{-\frac{1}{8}}, \tag{2.53}$$

where $Re_{d_h} = \frac{\rho u d_h}{\mu}$ is the Reynolds number for a pipe of hydraulic diameter d_h.
The specific turbulent dissipation rate can be obtained as follows:

$$\omega = C_\mu^{-\frac{1}{4}} \frac{\sqrt{k}}{l}, \tag{2.54}$$

where C_μ is a turbulence model constant which usually takes the value 0.09, k is the turbulent energy and l is the turbulent length scale [35]. The turbulence length scale describes the size of large energy-containing eddies in a turbulent flow. For a fully developed pipe flow this can be given as follows:

$$l = 0.07 d_h \tag{2.55}$$

Transport Equations for the Viscous Model

The turbulence kinetic energy (k) and the specific dissipation rate (ω) are obtained from the following transport equations [36]:

$$\frac{\partial}{\partial t}(\rho k) + \frac{\partial}{\partial x_i}(\rho k u_i) = \frac{\partial}{\partial x_j}\left(\Gamma_k \frac{\partial k}{\partial x_j}\right) + G_k - Y_k \tag{2.56}$$

$$\frac{\partial}{\partial t}(\rho\omega) + \frac{\partial}{\partial x_i}(\rho\omega u_i) = \frac{\partial}{\partial x_j}\left(\Gamma_\omega \frac{\partial \omega}{\partial x_j}\right) + G_\omega - Y_\omega \tag{2.57}$$

As the $k-\omega$ model has been modified over the years, production terms have been added to both the k and ω equations, which have improved the accuracy of the model for predicting free shear flows [35]. G_k represents the generation of turbulence kinetic energy due to mean velocity gradients. G_ω represents the generation of ω. Γ_k and Γ_ω represent the effective diffusivity of k and ω, respectively. Y_k and Y_ω represent the dissipation of k and ω due to turbulence.

As it will be described in Section 3.2.1, the $k-\omega$ model can be used for boundary layer problems, where the formulation works from the inner part through the viscous sub-layer, till the walls; hence the $k-\omega$ SST model can be used as a low Reynolds flow applications without extra damping functions [36].
The SST (Shear Stress Transport) formulation also switches to a $k-\epsilon$ behaviour in the free-stream. Therefore avoiding that the $k-\omega$ model is very sensitive to inlet free-stream turbulence properties. The $k-\omega$ SST model also shows good behaviour in adverse pressure gradients and separating flow. It does produce some large turbulence levels in regions with large normal strain, like stagnation regions and regions with strong acceleration [35].

2.4 Diffusion Flame

The fuel which burns is equal to the fuel which diffuses to the flame. The amount of fuel that burns is completely governed by diffusion.

The combustor illustrated in Fig. 2.7 has two inlets, one for the oxidizer and one for the fuel with specific different initial conditions. A simple mixture zone is not present in the combustor because the flame starts as soon as the two jets come into contact with each other. A liquid never burns immediately because it first has to vaporize. Moreover, the mixture of methane and oxygen is not an hypergolic one, so it needs to be ignited by an energy source. However, for the current work, the previous considerations can be neglected and the assumption that the flame starts as soon as the fuel and oxidizer come into contact is taken. A long combustor is needed to have the flame completely developed and/or in order to get a well-mixed mixture in the end of the combustor [28].
The following variables are illustrated in Fig. 2.7:

- $\dot{m}_1$ and $\dot{m}_2$ are the injected mass flow rates of fuel (methane) and oxidizer (liquid oxygen) respectively;
- Y_F^0 and Y_O^0 are the initial mass fractions of methane in the fuel and oxygen in the oxidizer at inlet condition. In the current work, pure methane and pure liquid oxygen are injected, so $Y_F^0 = Y_O^0 = 1$.
- T_F^0 and T_O^0 are the injection temperatures of fuel and oxidizer. Typically for rocket application, the initial temperatures can be very different.

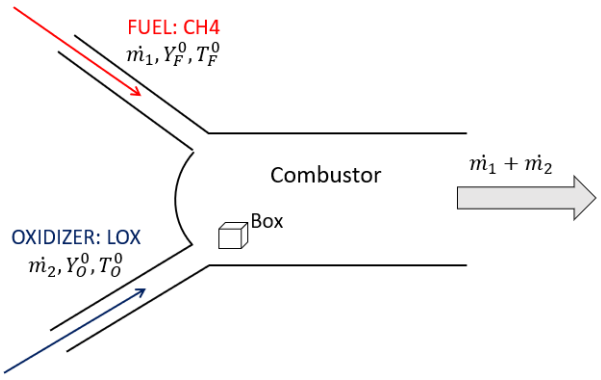

FIGURE 2.7: Combustor - Diffusion Flame

The definition of *equivalence ratio* (Eq. 2.5) was given in Section 2.1 as follows:

$$\Phi = s\frac{Y_F^0}{Y_O^0}$$

where s is the stoichiometric ratio (Eq. 2.4). However, the previous relation is exact and reliable for premixed flames, it is not good for diffusion flames. In fact, Y_F^0 and Y_O^0 should be taken at the same point. Considering diffusion flames, in different point, there are different combustion conditions. In a diffusion flame, the situation is more complex because fuel and oxidizer mix and burn at the same time. As a result, very lean mixtures are created in the vicinity of the oxidizer stream while very rich zones will be found near the fuel stream: the local equivalence ratio defined with Eq. 2.5 using local mass fractions may vary between zero (in lean zones) and infinity (in rich zones).
It is still useful to define a global equivalence ratio (Eq. 2.58) to characterize the overall behaviour of the combustor but this quantity controls only the global burner behaviour and not the local flame structure [28].

$$\Phi_g = s\frac{\dot{m}_F}{\dot{m}_O} \tag{2.58}$$

where, $\dot{m}_F$ and $\dot{m}_O$ are the fuel and oxidizer mass flow rate respectively. The diffusion flames do not care about the equivalence ratio Φ but the global equivalence ratio Φ_g. The link between the two quantities is given as follows:

$$\Phi_g = s\frac{\dot{m}_1 Y_F^0}{\dot{m}_2 Y_O^0} = \Phi\frac{\dot{m}_1}{\dot{m}_2}$$

The study of diffusion flames is divided into two different sections:

1. "Pure Mixing" problem (Section 2.4.2), in which the reactions are not taken into account;
2. Combustion problem (Section 2.4.3).

First of all, the definition of the mixture fraction z is presented because it is fundamental to explain the diffusion flames' theory.

2.4.1 Mixture Fraction

The mixture fraction z is a useful quantity to study mixing and diffusion flames. Considering non-reacting mixing between the two streams, the local mixture may be described at any point of the combustor as the result of a mixing between stream 1 and stream 2 in proportion z and $1 - z$ respectively [28].

The *mixture fraction* is introduced as follows:

$$z = z_F = \frac{Y_F}{Y_F^0} \tag{2.59}$$

Consequently the following variables are defined: $z_O = \frac{Y_O}{Y_O^0}$ and $z_{TOT} = z_F + z_O$.
Based on the species equations (Eq. 2.31) it is possible to prove that $z_{TOT} = 1$ everywhere [3]:

1. if $z_{TOT} = 1$ at $t = 0$, no gradient and time derivatives are present and z_T will not change
2. if $z_{TOT} \neq 1$ at $t = 0$ and a "long time" is waited, z_{TOT} will be equal to 1 everywhere. A diffusion problem/effect is analysed without additional term or source and at the boundaries there are the same amount of the quantity $z_{TOT} = 1$. After a certain period, this quantity will diffuse in all the domain and z_{TOT} will be homogeneously equal to unity.

[3] It will be checked in Chapter 5.2.1 when the results of the mixing simulation are analysed.

The mixture fraction is a well defined concept when some fundamental assumptions are done [16]:

- $D_K = D$, constant diffusion coefficient of the species within the mixture;
- Lewis number = $\frac{\lambda}{\rho c_p D} = 1$, heat and mass diffuse at the same way;
- low Mach Number;
- no heat losses.

Moreover, this concept is also easily extended to one-step chemical reactions, as it will be explained in Section 2.4.3.

A small box in the combustor illustrated in Fig. 2.7 sees the mass m_1 coming from the stream 1 (fuel) and the mass m_2 coming from the stream 2 (oxidizer). The total mass will be $m_1 + m_2$ and the mass of fuel $m_1 Y_F^0$. The fuel mass fraction at this point is

$$Y_F = \frac{m_F}{m_{TOT}} = \frac{m_1 Y_F^0}{m_1 + m_2}$$

and the mixture fraction z

$$z = \frac{Y_F}{Y_F^0} = \frac{m_1}{m_1 + m_2}$$

describes the mixture in mass between the 2 streams.

The mixture fraction z can be local or global. In combustion both are used. The local z is the z at one point and the field of z describes everywhere the fluid's properties. The global mixture fraction z_g instead can be defined by

$$z_g = \frac{\dot{m}_1}{\dot{m}_1 + \dot{m}_2} \tag{2.60}$$

looking at the flow rate globally injected into the system.

2.4.2 "Pure Mixing" Problem

The fuel and the oxidizer are injected but they don't ignite. The combustion is not considered and only the mixing will be analysed. Stream 1 (fuel) meets stream 2 (oxidizer) and a complete mixed flow leaves the combustor. The mixing could happen in a turbulent way or not. The mixture variable z treated in Section 2.4.1 can describe the mixing case.

Recalling Eq. 2.31 of continuity of the species k without reaction term and considering the assumption that D_k (diffusion term) is equal for all species ($D_K = D$), it can be shown that after some mathematical reformulations a simple solution for this problem exists [28]. If the mixture fraction z is known, all mass fractions are known. In fact, the following linear relations between mixture fraction z and species mass fraction are found as follows:

$$Y_F = Y_F^0 z \tag{2.61}$$

$$Y_O = Y_O^0 (1 - z) \tag{2.62}$$

The previous relations (Eq. 2.61 and 2.62) are plotted in Fig. 2.8 and they form the so-called mixing lines (linear in z-space). Any point in the mixture must be on these lines when no combustion takes place [28].

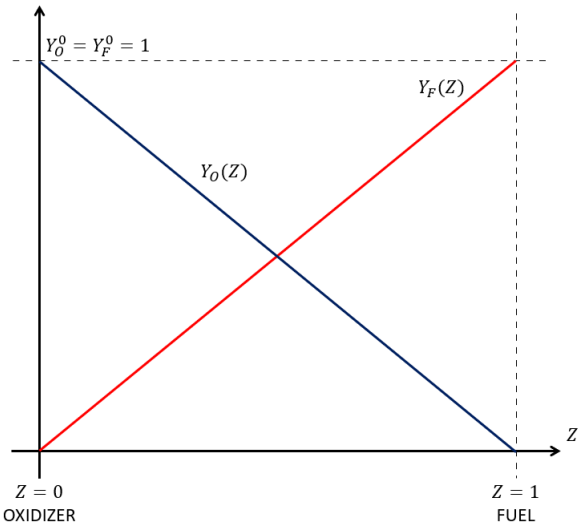

FIGURE 2.8: Mixing Lines in z-space

Eq. 2.48 of Temperature without source terms and with the assumptions done before is considered. It can be demonstrated that the mixing temperature is a weight average between the two injection temperatures as follows [28]:

$$T = zT_F^0 + (1 - z)T_O^0 \tag{2.63}$$

Fig. 2.9 shows the temperature lines following Eq. 2.63 in z-space.

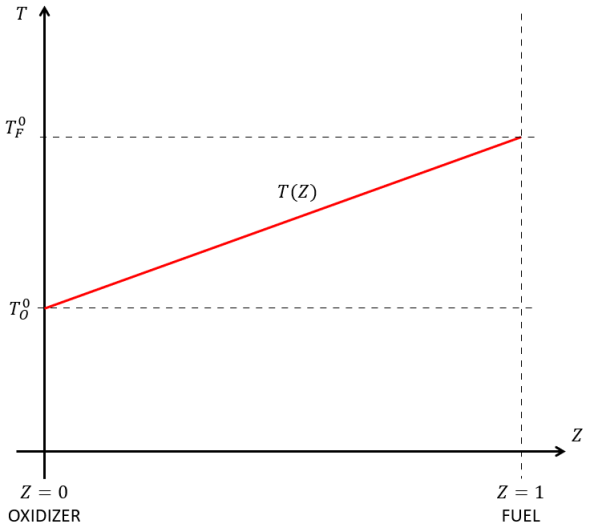

FIGURE 2.9: Mixing Temperature in z-space

2.4.3 Combustion Problem

First of all, two additional assumptions are necessary to get similar results for the combustion case study:

- Combustion with a *single-step* reaction [16] (simple *EDM* model);
- *Infinitely fast chemistry*: chemistry is faster than all the other mechanism (convection and diffusion for example). Y_F and Y_O cannot exist simultaneously at one point. If chemistry is very fast, the combustion is very fast and the reactions cannot exist at the same point [28].

The equations of species (fuel and oxidizer) and the equation of temperature are taken into account with the presence of the reaction rate. The global reaction has to be taken into account, and as explained in Section 2.3.3, the reaction term contains the combustion's effects.

The flame is infinitely thin and it is located on the stoichiometric surface. Only at the frame front itself $Y_F = Y_O = 0$ is found. These singular points have to be present.
Fig. 2.10 shows the mass fraction of fuel and oxidizer in the z-space (curve function of z) and it is possible to see how the singular point divides the combustion in two parts: lean and rich side [28]. Moreover, Fig. 2.11 shows the temperature in the z-space.

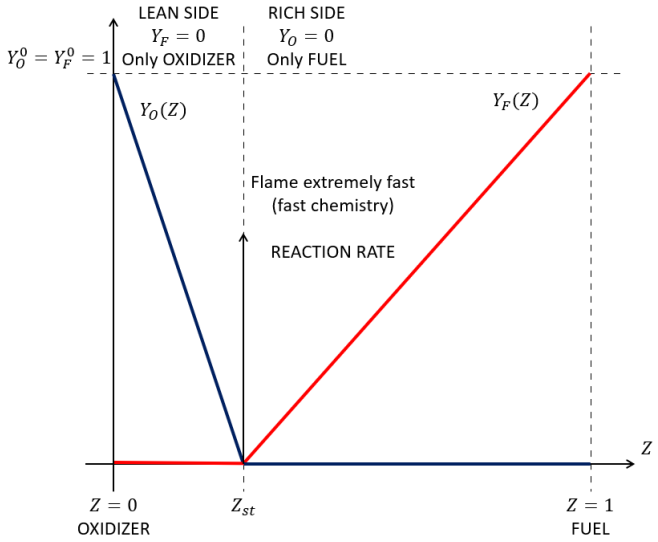

FIGURE 2.10: Combustion Mass Fractions in z-space

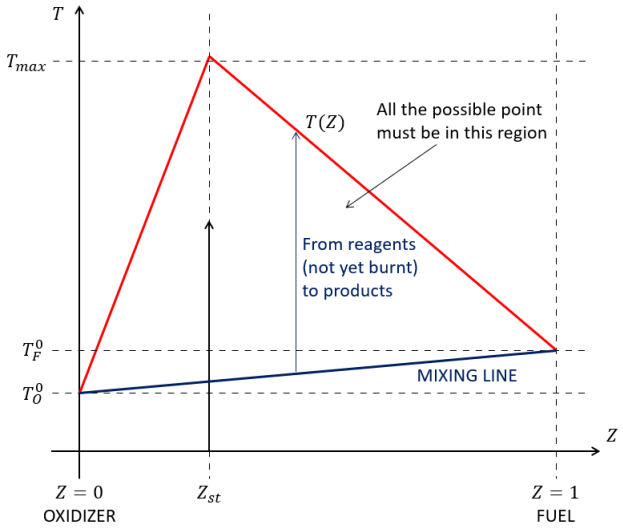

FIGURE 2.11: Combustion Temperature in z-space

The previous plots in Fig. 2.10 and 2.11 follow different relations considering lean and rich combustion:

- Lean Side (place in which no fuel is present $Y_F = 0$)

$$Y_O = Y_O^0(1 - \frac{z}{z_{st}}) \tag{2.64}$$

$$T = zT_F^0 + (1 - z)T_O^0 + \frac{QY_F^0}{c_p}z \tag{2.65}$$

- Rich Side (place in which no oxidizer is present $Y_O = 0$)

$$Y_F = Y_F^0(\frac{z - z_{st}}{1 - z_{st}}) \tag{2.66}$$

$$T = zT_F^0 + (1-z)T_O^0 + \frac{QY_F^0}{c_p} z_{st} \frac{1-z}{1-z_{st}} \tag{2.67}$$

In the expressions of temperatures (Eq . 2.65 and 2.67) the first part is the mixing temperature (Eq. 2.63) and the second is the increasing temperature due to combustion. The lines showed in Fig. 2.10 and 2.11 are well satisfied from experiments and it will be confirmed in Chapter 5.2.1.

Chapter 3

Modelling and Numerical Setup

After having explained theory behind the combustion science, the Fluent solver will be briefly presented in Section 3.1 to understand how the commercial code utilizes the mathematical and physics laws exposed in Chapter 2. Moreover, the adopted computational domain will be introduced in Section 3.2, and the computational resources are described briefly in Section 3.3.

3.1 Ansys Fluent Solver

Ansys Fluent solver 19.2 is the commercial code used to simulate the behaviour of the fluid. Ansys Fluent will solve the governing integral equations, exposed in Section 3.1.1, of the conservation of mass, momentum, energy and other scalars such as turbulence and chemical species. In both cases a control-volume-based technique is used that consists of [31]:

- Division of the domain into discrete control volumes using a computational grid.
- Integration of the governing equations on the individual control volumes to construct algebraic equations for the discrete dependent variables, unknowns, such as velocities, pressure, temperature, and conserved scalars.
- Linearization of the discretized equations and solution of the resultant linear equation system to yield updated values of the dependent variables.

Ansys Fluent allows you to choose one of the two numerical methods:

- pressure-based solver;
- density-based solver.

The two numerical methods employ a similar discretization process, called finite-volume, but the approach used to linearize and solve the discretized equations is different [31].

In both methods the velocity field is obtained from the momentum equations. In the density-based approach, the continuity equation is used to obtain the density field while the pressure field is determined from the equation of state. On the other hand, in the pressure-based approach, the pressure field is extracted by solving a pressure or pressure correction equation which is obtained by manipulatingthe continuity and momentum equations [31]. Meanwhile the density is derived from the *EOS* knowing all the other thermodynamic variables. For these considerations, in current work, knowing the conditions of the methane injector and oxygen, the choice to utilize the pressure-based solver is taken. As it will be explained in Chapter 4, the propellants are injected close to the critical conditions, this means that a lot of instabilities could appear in the density computation. In order to predict the density correctly, a study on different real gas *EOS* will be conducted in Section 4.2 and the selected method will be applied in Ansys Fluent to compute directly the density of the mixture. On the contrary, the pressure in the chamber should be fairly stable in a deflagration case and it will be extracted from the governing equations.
Moreover, DLR already own a density-based solver [1] and it might be interesting to compare different simulations results of the same test case.

[1]The DLR-TAU Code is a CFD software package for solving the Euler or Reynolds-averaged Navier-Stokes equations (*RANS*)

3.1.1 RANS Governing Equations

Reynolds Averaged Navier-Stokes equations (*RANS*) technique solves only for the mean values of each quantity. The balance equations for Reynolds or Favre (i.e. mass-weighted) quantities are obtained by averaging the instantaneous balance equations. Then, closure rules are required to model the features of the unsteady turbulence motions: a turbulence model to describe the flow dynamics and a turbulent combustion model to predict heat release and chemical species consumption and production [28]. The advantages of the RANS approach can be resumed as follows:

- "coarse" numerical grid
- geometrical simplification
- "reduced" numerical costs

and the drawbacks:

- only mean flow field
- models required

FANS Governing Equations

Ansys Fluent does not discretize and solve directly the governing equations exposed in Section 2.3, but the flow in the combustion chamber has been modelled as a steady state solution of the Favre-averaged Navier–Stokes equations, a density weighted averaging procedure, that is used in variable density flows like combustion.
In Favre averaging, the density weighted time averaging is applied to most flow field variables except for density and pressure. A typical flow field variable ϕ is decomposed to $\phi = \tilde{\phi} + \phi''$, where $\tilde{\phi}$ is the Favre averaged flow variable, ϕ'' is the density weighted fluctuation. To obtain the averaged governing equations, velocity vector, enthalpy and temperature are decomposed using Favre averaging as $u_i = \tilde{u_i} + u_i''$, $h = \tilde{h} + h''$ and $T = \tilde{T} + T''$. Density and pressure are decomposed using regular time averaging $\rho = \overline{\rho} + \rho'$ and $P = \overline{P} + P'$ [3].

The Favre averaged Navier-Stokes equations are derived from the conservation equation discussed in Section 2.3 and they are written as follows:

Continuity

$$\frac{\partial \overline{\rho}}{\partial t} + \frac{\partial}{\partial x_i}\left(\overline{\rho}\tilde{u_i}\right) = 0 \tag{3.1}$$

Momentum

$$\frac{\partial}{\partial t}\left(\overline{\rho}\tilde{u_i}\right) + \frac{\partial}{\partial x_j}\left(\overline{\rho}\tilde{u_i}\tilde{u_j}\right) = -\frac{\partial \overline{P}}{\partial x_i} + \frac{\partial}{\partial x_j}\left(\overline{\tau_{ij}} - \overline{\rho u_i'' u_j''}\right) \tag{3.2}$$

Energy

$$\frac{\partial}{\partial t}\left(\overline{\rho}\tilde{h}\right) + \frac{\partial}{\partial x_j}\left(\overline{\rho}\tilde{h}\tilde{u_j}\right) = \\ = \frac{\partial \overline{P}}{\partial t} + \tilde{u_j}\frac{\partial \overline{P}}{\partial x_j} + \overline{u_j''}\frac{\partial \overline{P}}{\partial x_j}\frac{\partial}{\partial x_j}\left(\overline{\lambda\frac{\partial T}{\partial x_j}} - \overline{\rho h'' u_j''}\right) + \overline{\tau_{ij}}\frac{\partial \tilde{u_i}}{\partial x_j} + \overline{\tau_{ij}\frac{\partial u_i''}{\partial x_i}} \tag{3.3}$$

Where, $\overline{\tau_{ij}}$ is the shear stress tensor and $\overline{\rho u_i'' u_j''}$ is a Reynolds stress term given by

$$\overline{\tau_{ij}} = \mu\left(\frac{\partial \tilde{u_i}}{\partial x_j} + \frac{\partial \tilde{u_j}}{\partial x_i}\right) - \frac{2}{3}\mu\frac{\partial \tilde{u_k}}{\partial x_k}\delta_{ij} \tag{3.4}$$

$$-\overline{\rho u_i'' u_j''} = \mu_t\left(\frac{\partial \tilde{u_i}}{\partial x_j} + \frac{\partial \tilde{u_j}}{\partial x_i}\right) - \frac{2}{3}\mu_t\frac{\partial \tilde{u_k}}{\partial x_k}\delta_{ij} - \frac{2}{3}\overline{\rho}k\delta_{ij} \tag{3.5}$$

For turbulence closure the SST $k-\omega$ turbulence model is chosen, as explained in Section 2.3.5. The transport equation for the turbulent kinetic energy k and the turbulent vorticity ω are given as,

$$\frac{\partial}{\partial t}\left(\overline{\rho}k\right)+\frac{\partial}{\partial x_j}\left(\overline{\rho}\tilde{u_j}k\right)=\frac{\partial}{\partial x_j}\left[\left(\mu+\sigma_k\mu_t\right)\frac{\partial k}{\partial x_j}\right]+\tau_{ij}^t\frac{\partial \tilde{u_i}}{\partial x_j}-\beta^*\overline{\rho}\omega k \tag{3.6}$$

$$\begin{aligned}\frac{\partial}{\partial t}\left(\overline{\rho}\omega\right)+\frac{\partial}{\partial x_j}\left(\overline{\rho}\tilde{u_j}\omega\right)=\\ =\frac{\partial}{\partial x_j}\left[\left(\mu+\sigma_{\omega 1}\mu_t\right)\frac{\partial \omega}{\partial x_j}\right]+\frac{C_\omega\overline{\rho}}{\mu_t}\tau_{ij}^t\frac{\partial \tilde{u_i}}{\partial x_j}-\beta\overline{\rho}\omega^2+2(1-F_1)\frac{\overline{\rho}\sigma_{\omega 2}}{\omega}\frac{\partial k}{\partial x_j}\frac{\partial \omega}{\partial x_j}\end{aligned} \tag{3.7}$$

where, τ_{ij}^t is the turbulent stress term expressed as follows:

$$\tau_{ij}^t=-\overline{\rho u_i'' u_j''} \tag{3.8}$$

Similarly μ_t, β^*, $\sigma_{\omega 1}$, C_ω, β and $\omega_{\omega 2}$ are model constants; μ is the molecular viscosity and the function F_1 blends the model coefficients of the $k-\omega$ model in boundary layers with the transformed $k-\epsilon$ model in free shear layers and free stream zones[3].

Coupled and Pseudo-transient Method

The pressure-based solver allows you to solve your flow problem in either a segregated or coupled manner. Ansys Fluent provides the option to choose among five pressure-velocity coupling algorithms: SIMPLE, SIMPLEC, PISO, Coupled [29].

Coupled uses the pressure-based coupled solver. Using the coupled approach offers some advantages over the non-coupled or segregated approach. The coupled scheme obtains a robust and efficient single phase implementation for steady-state flows, with superior performance compared to the segregated solution schemes. This pressure-based coupled algorithm offers an alternative to the density-based and pressure-based segregated algorithm with SIMPLE-type pressure-velocity coupling. For transient flows, using the coupled algorithm is necessary when the quality of the mesh is poor, or if large time steps are used. The coupled algorithm solves the momentum and pressure-based continuity equations together. The full implicit coupling is achieved through an implicit discretization of pressure gradient terms in the momentum equations, and an implicit discretization of the face mass flux [29].

The coupled method is employed in the current work and all the equations have been solved initially using a first-order up-wind advection scheme to help the convergence of the simulation. Then, when a stable solution is reached, it is possible to use a second-order up-wind advection scheme for some equations. In general following the literature, the first order scheme has been used because of divergence in the solver during use of the high resolution scheme. The reason of the divergence is numerical dispersion due to high gradients of temperature and mass fractions [41].

3.1.2 Combustion Model

Ansys Fluent calculates with "time averaging values of the species local mass fractions" $\overline{Y_i}$. They are described by similar balancing equation as in the case of the species equation, which have this shape in conservative form that derives from Eq. 2.31

$$\frac{\partial}{\partial t}(\rho\overline{Y_i})+\frac{\partial}{\partial x_i}(\rho\overline{u_i}\overline{Y_i})=-\frac{\partial}{\partial x_i}\overline{J_{i'}}+R_{i'} \tag{3.9}$$

where ρ is density, $\overline{u_i}$ is time-averaging component of the flow velocity. On the right side $R_{i'}$ is the rate production[2] of species i through chemical reactions [4].

[2]The production rate $\dot{\omega}_k$ was introduced in Section 2.3.3

Distribution of species can be carried in different assumptions. Usually the distribution can be distinguished for laminar and turbulent flow. In turbulent flows the mass diffusion for species i' is expressed in the following form:

$$J_{i'} = -\left(\frac{\mu_t}{Sc_t}\right)\frac{\partial \overline{Y_{i'}}}{\partial x_j} \tag{3.10}$$

Sc_t is the turbulent Schmidt number and it is defined as follows:

$$Sc_t = \frac{\mu_t}{\rho D_t},$$

where μ_t is the turbulent viscosity and D_t is the thermal diffusivity [4]. While the turbulent Schmidt number Sc_t models the mass transfer, the turbulent heat transfer is modelled by the turbulent Prandtl number Pr_t.

$$Pr_t = C_p\frac{\mu_t}{k_T}$$

The value of 0.7 has been recommended for the turbulent Schmidt number in axisymmetric turbulent free round jets [5]. The turbulent Prandtl number has been set to the default value of 0.9, which has been extensively validated for heat transfer predictions in CFX [12].

The reaction or production rate $R_{i'}$ that appears as source terms in Eq. 3.9 is computed in Ansys Fluent, for turbulent flows, by one of three models[39]:

- Laminar finite-rate model: the effect of turbulent fluctuations are ignored, and reaction rates are determined by Arrhenius kinetic expressions.
- Eddy-dissipation model (Section 3.1.2): reaction rates are assumed to be controlled by the turbulence, so expensive Arrhenius chemical kinetic calculations are avoided. The model is computationally cheap, but, for realistic results, only one or two step heat-release mechanisms should be used.
- Eddy-dissipation-concept (*EDC*) model: detailed Arrhenius chemical kinetics can be incorporated in turbulent flames. Note that detailed chemical kinetic calculations are computationally expensive.

As said many times, *EDM* is chosen for this work. In this model, constant activation energy and pre-exponential factor, discussed in 2.3.3, have significant effects on the results. In the specialized literature there exist many variants of these constants. In this case, the constants of one-equation model by Zambon Chelliah are used[4]:

- Pre-exponential factor: $1,35 \cdot 10^{20} \quad [cm^3 \cdot mol^{-2} \cdot s^{-1}]$,
- Activation energy: $30000 \quad [cal \cdot mol^{-1}]$.

Eddy-Dissipation-Model

The employed model is based on the assumption of a thin flame (i.e., chemical reactions are infinitely fast), and the rate of chemical transformations is limited by the mixing rate. Most fuels are fast burning, and the overall rate of reaction is controlled by turbulent mixing. In non-premixed flames, turbulence mixes fuel and oxidizer into the reaction zones where they burn quickly. In such cases, the combustion is said to be mixing-limited, and the complex, and often unknown, chemical kinetic rates can be safely neglected[39].

In the used model, chemical transformation occurs in a single-step global reaction (Eq. 2.2)

$$CH_4 + 2O_2 \rightarrow CO_2 + 2H_2O$$

in which the reaction rate is proportional to the rate of eddy dissipation:

$$Reaction\ rate \propto \epsilon/k,$$

where ϵ is the turbulence eddy dissipation, and k is the turbulent kinetic energy [40].

Since the propellants are injected separately in the combustion chamber, the combustion process is limited by the mixing. The advantages of the eddy-dissipation model (*EDM*) are its simplicity and robustness, but to achieve acceptable results, the model should be extended, especially for the case of rocket combustion. As introduced in Section 2.2, at high temperatures ($T > 3000K$), the dissociation of H_2O becomes important, namely, the fraction of H_2O in a chemical equilibrium mixture is significantly less than 100% in the burned gases in rocket engines. The direct use of Eq. 2.2 gives a flame temperature near 5000 K, as it will be demonstrate with the combustion simulations in Section 5.2.2, whereas the flame temperature in rocket combustion chambers using methane amounts to around 3500 K, as calculated in Section 2.2.

Using the eddy-dissipation model, the average rate of production of species i due to reaction r, $R_{i,r}$, is given by the smaller of the two expressions below [39]:

$$R_{i,r} = \nu'_{i,r} M_{w,i} A \rho_i \frac{\epsilon}{k} min \left(\frac{Y_R}{\nu'_{R,r} M_{w,R}} \right) \tag{3.11}$$

$$R_{i,r} = \nu'_{i,r} M_{w,i} A B \rho_i \frac{\epsilon}{k} \frac{\sum_P Y_P}{\sum_j^N \nu''_{j,r} M_{w,j}}, \tag{3.12}$$

where

- Y_P is the mass fraction of any product species, P
- $Y_{\mathcal{R}}$ is the mass fraction of a particular reactant, $\mathcal{R}$
- A is an empirical constant equal to 4.0
- B is an empirical constant equal to 0.5
- ρ_i is the density of i' species.

In Eq. 3.11 and 3.12, the chemical reaction rate is governed by the large-eddy mixing time scale, k/ϵ. Combustion proceeds whenever turbulence is present ($\epsilon/k > 0$), an explicit ignition source is not required to initiate combustion. This is usually acceptable for steady-state non-premixed flames. The eddy-dissipation model requires products to exist in order to initiate the reaction. However, if you converge a mixing solution first, where all product mass fractions are zero, you may then have to patch products into the reaction zone to ignite the flame [39]. This method is necessary when the real gas *SRK* simulations are initialized from the mixing solutions.

In the eddy-dissipation model, every reaction has the same, turbulent rate, and therefore the model should be used only for one-step (reactant $\rightarrow$ product), or two-step (reactant $\rightarrow$ intermediate, intermediate $\rightarrow$ product) global reactions. The model cannot predict kinetically controlled species such as radicals.

3.2 Computational Domain

The employed *CFD* code uses the finite volume element method. The numerical simulations of the flow inside the chamber have been carried out in a three-dimensional domain, which represents a sector of 45 degrees. The domain sector of the axisymmetric combustion chamber is shown in Fig. 3.1. Fig. 3.2 shows the 3D combustion chamber with a "coaxial" injector in the center.

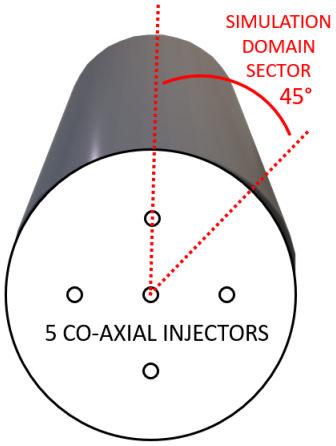

FIGURE 3.1: Combustion Chamber Domain

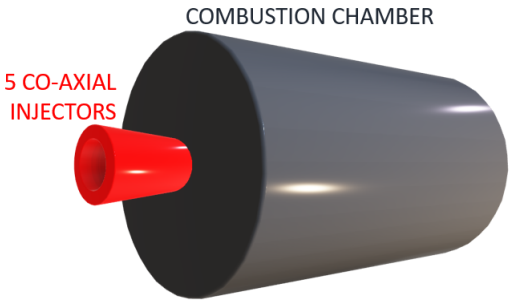

FIGURE 3.2: Combustor and Injector Domain

In previous studies [26], it was found that, for the flame of a coaxial injector, the simulation results depended on the velocity profile in the (outer) annular passage of coaxial injector and that a uniform velocity profile resulted in a wrong spreading angle and poor convergence at the grid nodes near the oxygen post tip. Therefore, also parts of the injectors have to be simulated. The outlet profiles of the injectors are imported as inlet profiles in the combustion chamber simulation. The 5 coaxial injectors have the geometry showed in Fig. 3.3.

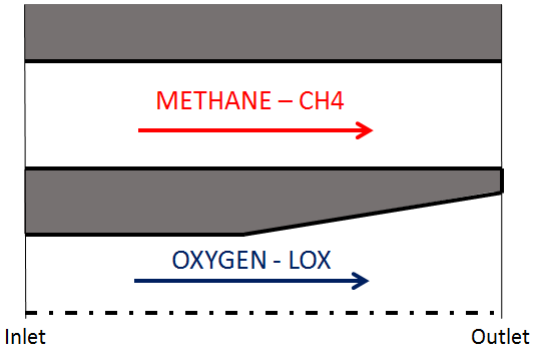

FIGURE 3.3: Coaxial Injector Geometry

As it can be seen in Fig. 3.3, the methane part has a constant area while the oxygen one has the last part near the chamber in which the area increases, which creates a complex behaviour of the liquid oxygen. In Section 5.1 the injectors simulations results will be presented and discussed.

The simulations were performed on different meshes types. All meshes were generated using the computer program Meshing from the package Ansys CFD. Regarding the injectors,

the mesh is totally hexahedral structured with refinement near the wall to capture the right velocity profile of the stream, as Fig. 3.5 and 3.7 show. Moreover, the methane and oxygen injector meshes are illustrated in Fig. 3.4 and 3.6. The meshes of the 180 degrees sectors of injectors are illustrated because they will be used to compare *NIST* and *SRK EOS* simulations.

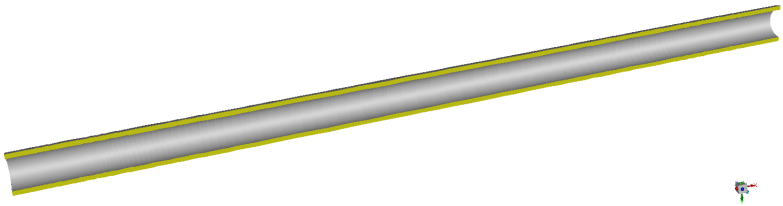

FIGURE 3.4: Methane Injector Mesh - 180 degrees

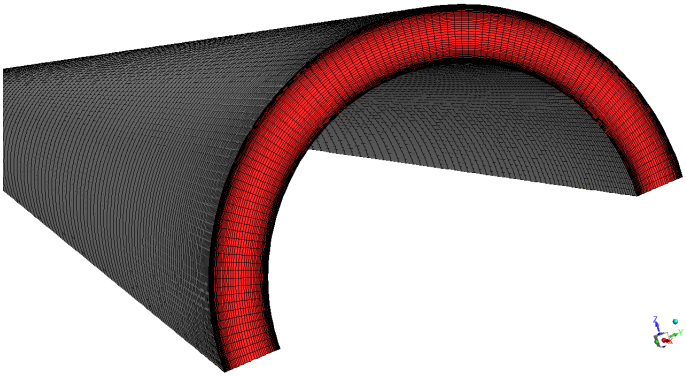

FIGURE 3.5: Methane Injector Mesh Outlet - 180 degrees

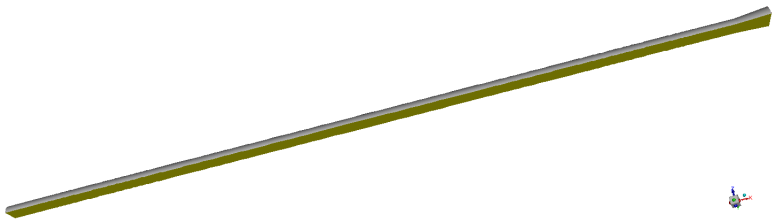

FIGURE 3.6: Oxygen Injector Mesh - 180 degrees

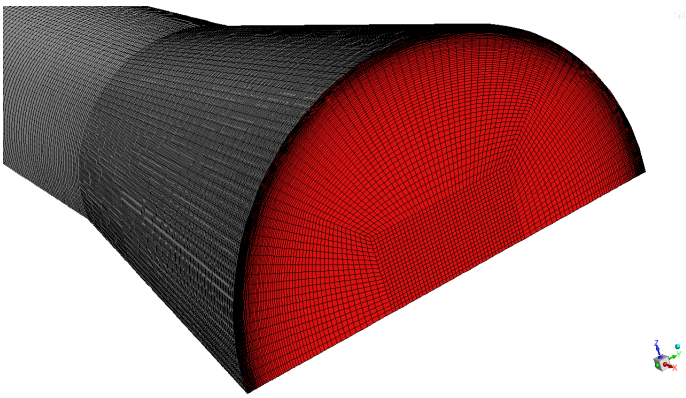

FIGURE 3.7: Oxygen Injector Mesh Outlet - 180 degrees

The mesh consists of about 1.5 millions nodes for the methane injector and 2.5 millions nodes for the oxygen injector. In both cases, the total number of nodes are refereed to the sector of 180 degrees showed previously. Hexahedral layers near the walls grow with an expansion ratio of 1.1 and the smallest spacing between the nodes is located near the wall and it is equal to 1 μm.
During the meshing of the injectors, the attention was given to obtain reliable outlet profiles. For this reason, a mesh convergence study was not conducted and the simulations are performed with a huge number of nodes.

In the combustion chamber a "mixed" mesh is constructed. The flame and the wall interaction are captured with hexahedral structured mesh, whereas the remaining domain is unstructured, as it can be seen in Fig. 3.9 and 3.10.

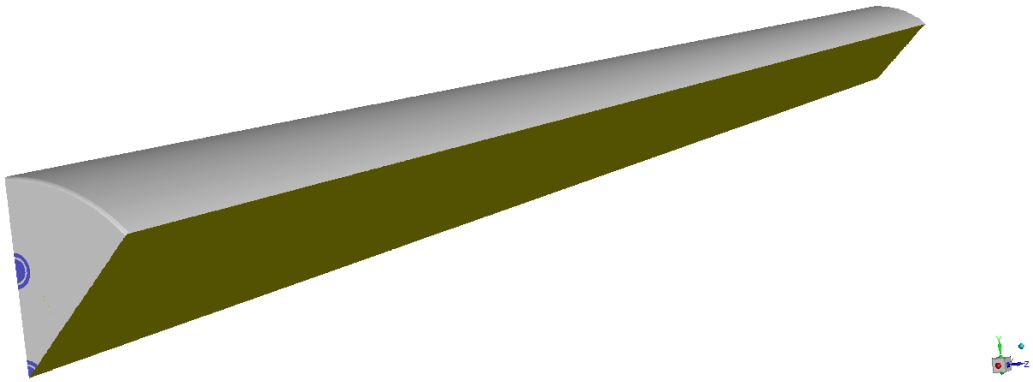

FIGURE 3.8: Combustion Chamber Mesh - 45 degrees

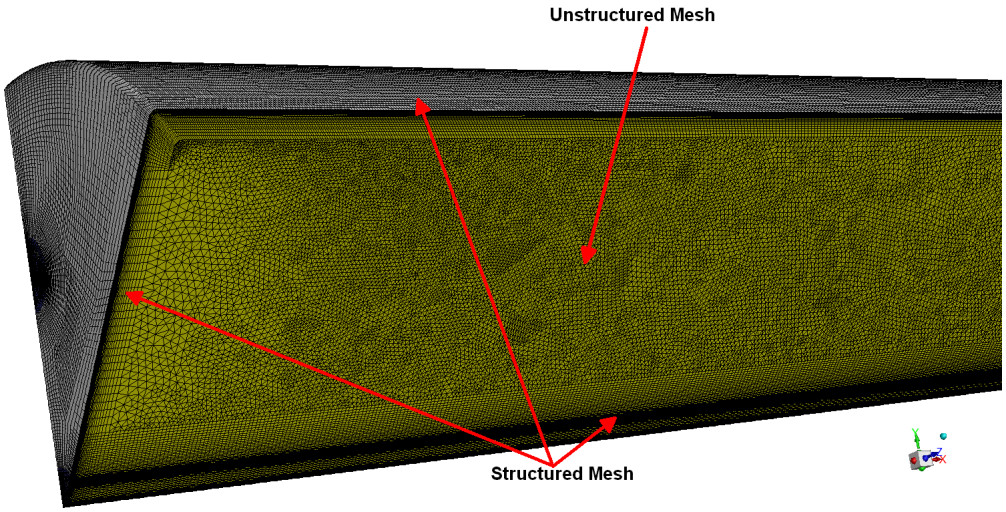

FIGURE 3.9: Combustion Chamber Mesh Symmetry 1 - 45 degrees

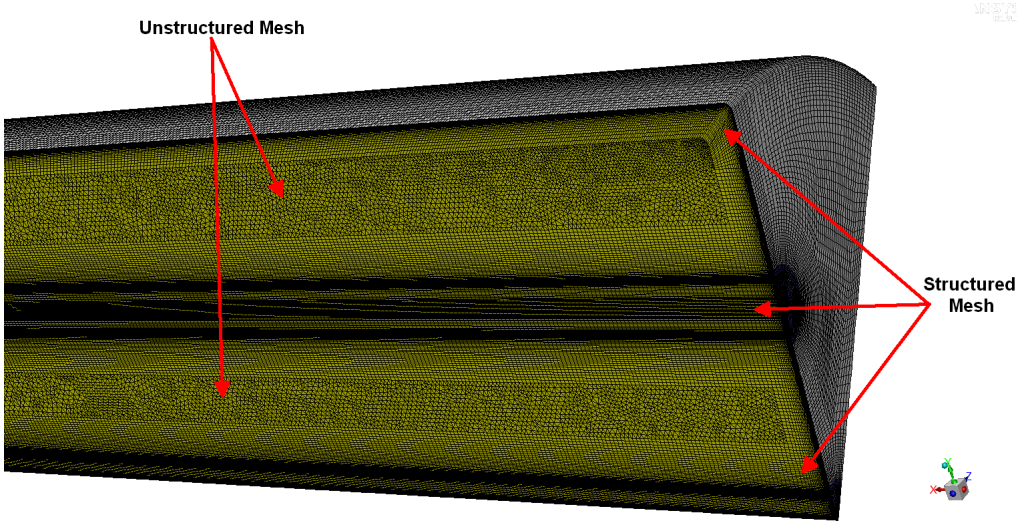

FIGURE 3.10: Combustion Chamber Mesh Symmetry 2 - 45 degrees

Following previous experience in *CFD* simulations [40], the generated meshes were refined near the injector post and around the shear layer between the jets of the fuel and oxidizer; here, the spacing reaches down to 1 μm. In the base mesh, the spacing between the nodes varies from 1 μm to 1 mm, and most of the mesh elements are stretched in the axial direction. The smallest spacing is located on the side walls, for reasons that will be explained in Section 3.2.1, but the coarsest part of the mesh is located in the final part of the chamber, close to the outlet surface. Hexahedral layers near the walls grow with the expansion ratio of 1.1. In the whole domain, the expansion ratio does not exceed a value of 1.2. The base mesh consists of about 10 millions nodes.

3.2.1 Modelling Flow Near the Wall

Turbulent flows are significantly affected by the presence of walls. Obviously, the mean velocity field is affected through the no-slip condition that has to be satisfied at the wall. However, the turbulence is also changed by the presence of the wall in non-trivial ways. Very close to the wall, viscous damping reduces the tangential velocity fluctuations, while kinematic blocking reduces the normal fluctuations. For this reason, there are strong gradients in the dependent variables. Toward the outer part of the near-wall region, however, the turbulence is rapidly augmented by the production of turbulence kinetic energy due to the large gradients in mean velocity[24].

The representation of these processes within a numerical simulation raises the following problems:

- How to account for viscous effects at the wall.
- How to resolve the rapid variation of flow variables that occurs within the boundary layer region.

Numerous experiments have shown that the near-wall region can be largely subdivided into three layers, as it can be seen in Fig. 3.11. In the innermost layer, called the "viscous sublayer", the flow is almost laminar, and the (molecular) viscosity plays a dominant role in momentum and heat or mass transfer. In the outer layer, called the fully-turbulent layer, turbulence plays a major role. Finally, there is an interim region between the viscous sublayer and the fully turbulent layer where the effects of molecular viscosity and turbulence are equally important [24].

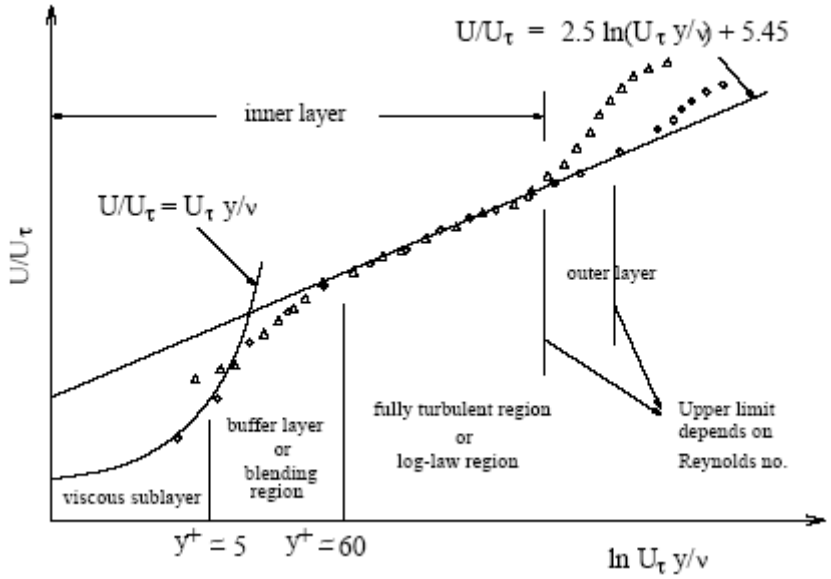

FIGURE 3.11: Subdivisions of the Near-Wall Region [24]

Assuming that a logarithmic profile reasonably approximates the velocity distribution near the wall, it provides a means to numerically compute the fluid shear stress as a function of the velocity at a given distance from the wall. This is known as a "wall function" and the logarithmic nature gives rise to the well known "log law of the wall".

The log-law, which is valid for equilibrium boundary layers and fully developed flows, provides upper and lower limits on the acceptable distance between the near-wall cell centroid and the wall [23]. The distance is usually measured in the dimensionless wall units, as for example

$$y^+ = \frac{\rho u_\tau y}{\mu}, \tag{3.13}$$

where u_τ is the friction velocity, defined as $\sqrt{\frac{\tau_w}{\rho}}$ [24] and y is the wall-normal distance calculated at the cell centers [11].

The *SST k- ω* model in Ansys Fluent is available as low Reynolds number models as well as high Reynolds number model. The low Reynolds number method resolves the details of the boundary layer profile by using very small mesh length scales in the direction normal to the wall (very thin inflation layers). Note that the low-Re method does not refer to the device Reynolds number, but to the turbulent Reynolds number, which is low in the viscous sublayer.

The following mesh requirements are recommended[23]:

- When the model is employed with the intention of resolving the laminar sublayer, y^+ at the wall-adjacent cell should be on the order of $y^+ = 1$. However, a higher y^+ is acceptable as long as it is well inside the viscous sublayer $(y^+ < 4\ to\ 5)$.
- At least 10 cells within the viscosity-affected near-wall region ($Re_y < 200$) should be present to be able to resolve the mean velocity and turbulent quantities in that region. In Ansys Fluent, the turbulent Reynolds number is defines as follows:

$$Re_y = \frac{\rho y \sqrt{k}}{\mu} \tag{3.14}$$

However, if the low-Re Corrections option in viscous model dialogue box is enabled, then the intention is to resolve the laminar sublayer. For cases where the laminar sublayer is adjacent to wall cells, it should be constructed so as to result in y^+ being in the range of 1.

The fulfilment of these requirement will be confirmed in Chapter 5 when the results are

discussed. In particular, the laminar sublayer is solved only in the injectors simulations to obtain reliable outlet profiles. However, it is neglected in the combustor simulations for this first analysis in order to reduce the computational costs.

3.3 Computational Resources

The simulations are launched using the cluster system of the DLR site of Lampoldshausen. The cluster system is an unified one and in total it consists of 58 nodes with 8 processors each. Unfortunately, a single job can allocate maximum 10 nodes with 80 processors and it will run maximum 72 hours (3 days). Moreover, the Fluent licence are very expensive and consequently the number of available nodes for Ansys Fluent jobs was approximately 80.

Chapter 4

Real Gas Effects

The density computation, the transport properties (dynamic viscosity and thermal conductivity) and thermodynamic property (heat capacity) will be analysed and commented. In order to predict the real behaviour of the fluid it is very important to model properly these properties knowing the inlet condition of the propellants.

4.1 Ideal Gas EOS

An ideal gas is a theoretical gas composed of many randomly moving point particles whose only interactions are perfectly elastic collisions. The ideal gas concept is useful because it obeys the ideal gas law, the following simple equation of state:

$$\frac{p}{\rho} = \frac{RT}{M} \tag{4.1}$$

Using the ideal gas law (Eq. 4.1), one needs to make a couple assumptions [25]:

1. The volume taken up by the imaginary ideal gas molecules is ignored;
2. The gas molecules do not attract or repel each other.

Generally, a gas behaves more like an ideal gas at higher temperature and lower pressure, as the potential energy due to intermolecular forces becomes less significant compared with the particles' kinetic energy, and the size of the molecules becomes less significant compared to the empty space between them.

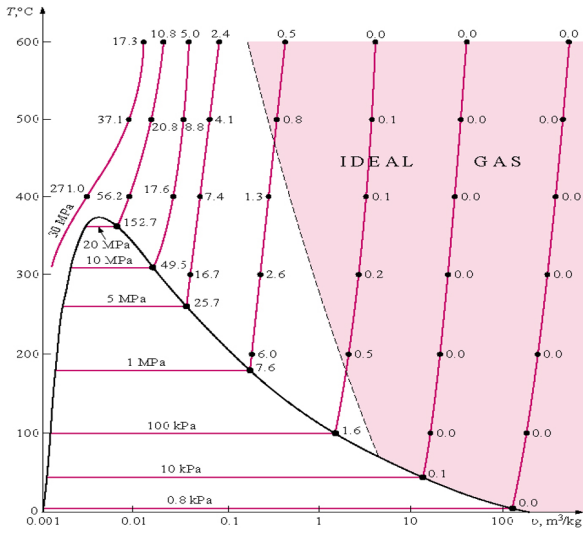

FIGURE 4.1: T-v Curve Water [6]

Fig. 4.1 is the T-v diagram of the water and it shows the percentage of error involved in assuming steam to be an ideal gas, and the region where steam can be treated as an ideal gas [6]. In general, it is possible to note in Fig. 4.1 that the ideal gas model tends to fail at

lower temperatures and/or higher pressures, when intermolecular forces and molecular size becomes important. At high pressures, the volume of a real gas is often considerably larger than the ideal gas law would predict. At low temperatures, the pressure of a real gas is often considerably less than predicted by the ideal gas law. At some point of low temperature and high pressure, gases undergo a phase transition, such as to a liquid or a solid. The model of an ideal gas, however, does not describe or allow phase transitions. It must be modelled by more complex equations of state.

The deviation from the ideal gas behaviour can be described by a dimensionless quantity, the compressibility factor, Z.

4.1.1 The Compressibility Factor

The compressibility factor (Z) is a correction factor which describes the deviation of a real gas from ideal gas behaviour. It is simply defined as the ratio of the molar volume of a gas to the molar volume of an ideal gas at the same temperature and pressure [25].

$$Z = \frac{V_{m_{gas}}}{V_{m_{IDEALgas}}} \tag{4.2}$$

The compressibility factor is defined in thermodynamics and engineering frequently as:

$$Z = \frac{p}{\rho R^* T}, \tag{4.3}$$

where p is the pressure, ρ is the density of the gas and $R^* = R/M$ is the specific gas constant, M being the molar mass, and the T is the static temperature.

For an ideal gas the compressibility factor is $Z = 1$ per definition and generally its value increases with pressure and decreases with temperature.
At high pressures molecules are colliding more often. This allows repulsive forces between molecules to have a noticeable effect, making the molar volume of the real gas (V_m) greater than the molar volume of the corresponding ideal gas ($((V_m)_{idealgas} = R^*T/p)$, which causes Z to exceed one. When temperatures are lower, the molecules are free to move. In this case attractive forces dominate, making $Z < 1$. The closer the gas is to its critical point (explained in Section 4.4) or its boiling point, more Z deviates from the ideal case [25].

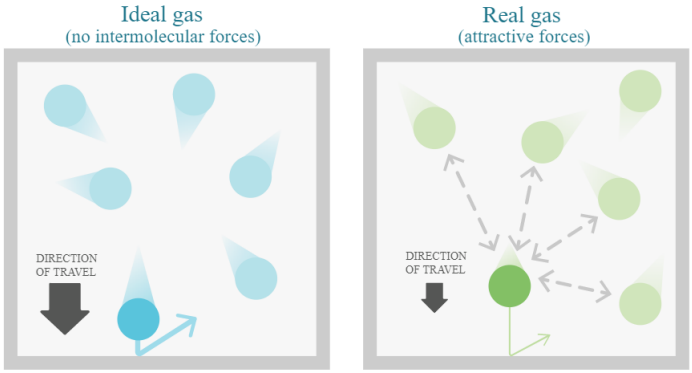

FIGURE 4.2: Compressibility Effects [25]

Compressibility factor values are usually obtained by calculation from equations of state. For a gas that is a mixture of two or more pure gases, the gas composition must be known before compressibility can be calculated.
First of all, Z is computed knowing the thermodynamic conditions of the reactants at inlet condition. In order to compute the following results, the *NIST* real gas data [9] are taken as reference for real gas thermodynamic properties and in particular the values of Z show that it is crucial to consider the real gas behaviour.

$$Z_{CH4} \approx 0.8 \qquad Z_{LOX} \approx 0.2$$

For this reason, the conclusion that the ideal gas law is unsuitable is taken. In order to continue the study it is necessary to understand which real gas *EOS* fits better with the real gas data taken from the *NIST* database [9]. The right *EOS* needs to be selected in Ansys Fluent to compute the density of the species.

4.2 Real Gas EOS

At pressures above the critical pressure and near the critical temperature, changes in temperature can correspond to extreme density gradients. Under such conditions real gas equations have to be used. The differences of thermophysical properties between ideal and real gases are also very significant. Neglecting real gas behaviour could lead to significantly erroneous thermofluidynamic fields [3]. In fact, as it will be analysed in Section 4.3, close to critical point substances exhibit large variation in thermodynamic and transport properties which in turn affects mixing and combustion results.

The cubic equations of state are very effective in predicting Pressure-Volume-Temperature behaviour of most substances, close to the critical point. Those equations of state are modifications of the simpler Van der Waals Equation (Section 4.2.1). The Van der Waals *EOS* is based on the idea that the pressure of a fluid results from the sum of repulsive and attractive forces.

There are a lot of equations of state for real gas available in literature. In the current work four different methods will be presented considering the mathematical and physical point of view:

- Van der Waals (Section 4.2.1)
- Peng-Robinson (Section 4.2.2)
- Redlich-Kwong (Section 4.2.3)
- Soave modification of Redlich-Kwong (Section 4.2.4)

After that, the most suitable will be taken and selected within Ansys Fluent to compute the density of the fluid.

4.2.1 Van der Waals EOS

The *VdW EOS* basically incorporates the effect of gas molecule volume and intermolecular forces into the Ideal Gas *EOS* (Eq. 4.1) [20]. It is expressed as follows:

$$\left(p + \frac{a}{V_m^2}\right)(V_m - b) = RT, \tag{4.4}$$

where V_m is molar volume. The substance-specific constants a and b can be calculated from the critical properties p_c,T_c and V_c (noting that V_c is the molar volume at the critical point) as:

$$a = 3p_cV_c^2 \qquad b = \frac{V_c}{3}$$

The Van der Waals equation of state was one of the first to perform markedly better than the ideal gas law. In this landmark equation, a is called the attraction parameter and b the repulsion parameter or the effective molecular volume. While the equation is definitely superior to the ideal gas law and does predict the formation of a liquid phase, the agreement with experimental data is limited for conditions where the liquid forms is not present. For this reason, since *LOX* is injected in the combustion chamber, the VdW *EOS* cannot be used to model the oxygen density correctly [20].

4.2.2 Peng-Robinson EOS

The Peng-Robinson *EOS* has the basic form [13]:

$$p = \frac{R \cdot T}{V_m - b} - \frac{a \cdot \alpha}{V_m^2 + 2 \cdot B \cdot V_m - b^2} \tag{4.5}$$

Variables a, b, and α are further described by:

$$a = \frac{0.457235 \cdot R^2 \cdot T_c^2}{p_c}, \quad b = \frac{0.077796 \cdot R \cdot T_c}{p_c}, \quad \alpha = (1 + k \cdot (1 - T_r^{\frac{1}{2}}))^2$$

where R is the universal gas constant, T_c and p_c the critic temperature and pressure and $T_r = T/T_c$.
Further k in the definition of α is defined as:

$$k = 0.37464 + 1.54226 \cdot \omega - 0.26992 \cdot \omega^2$$

where $\omega = p^{sat}/p_c$ is the acentric factor (a measure of molecules' non-sphericity) which is a function of the saturated vapour pressure and the critical pressure. It is very helpful to write Eq. 4.5 in polynomial form (Eq. 4.6) because then it can be easily solved in *Matlab*[1]

$$Z^3 - (1 - B)Z^2 + (A - 2B - 3B^2)Z - (AB - B^2 - B^3) = 0 \tag{4.6}$$

Where A, B and Z (compressibility factor) are respectively

$$A = \frac{\alpha a p}{R^2 T}, \qquad B = \frac{bp}{RT}, \qquad Z = \frac{PV}{nRT}$$

The Peng-Robinson equation of state can model some liquids as well as real gases. It is easy to see in the first term of Eq. 4.5 that this state equation had its origins in the Ideal Gas *EOS*, since V/n gives the molar volume V_m. In order to apply the ideal gas law to real gases, correction terms have been included that are composed of empirically derived offsets [13].

4.2.3 Redlich-Kwong EOS

Introduced in 1949, the Redlich-Kwong equation of state (Eq. 4.7) was a considerable improvement over other equations of the time. It is still of interest primarily due to its relatively simple form. While superior to the van der Waals equation of state, it performs poorly with respect to the liquid phase and thus cannot be used for accurately calculating vapor–liquid equilibria. However, it can be used in conjunction with separate liquid-phase correlations for this purpose [20].

$$p = \frac{RT}{V_m - b} - \frac{a}{\sqrt{T} V_m (V_m + b)} \tag{4.7}$$

where

$$a = 0.42748 \frac{R^2 T_c^{\frac{5}{2}}}{p_c} \qquad b = 0.08664 \frac{RT_c}{p_c}$$

4.2.4 Soave-Redlich-Kwong EOS

In 1972 G. Soave replaced the $1/\sqrt{T}$ term of the Redlich-Kwong equation with a function $\alpha(T, \omega)$ involving the temperature and the acentric factor (the resulting equation is also known as the Soave-Redlich-Kwong equation of state, abbreviated *SRK EOS*). The α function was devised to fit the vapor pressure data of hydrocarbons and the equation does fairly well for these materials.

$$p = \frac{RT}{V_m - b} - \frac{a\alpha}{V_m (V_m + b)} \tag{4.8}$$

[1]The Matlab scripts cannot be shown for corporate data security policies.

where

$$a = \frac{0.42747 R^2 T_c^2}{p_c}$$

$$b = \frac{0.08664 R T_c}{p_c}$$

$$\alpha = (1 + (0.48508 + 1.55171\omega - 0.15613\omega^2)(1 - T_r^{0.5}))^2$$

This formulation for α is from Graboski and Daubert. The original formulation from Soave is:

$$\alpha = (1 + (0.480 + 1.574\omega - 0.176\omega^2)(1 - T_r^{0.5}))^2$$

Note especially that this replacement changes the definition slightly, as T_c is now to the second power, instead of 2.5 before.
The *SRK EOS* is written in polynomial form as follows:

$$Z^3 - Z^2 + Z(A - B - B^2) - AB = 0, \tag{4.9}$$

where

$$A = \frac{a\alpha p}{R^2 T^2} \qquad B = \frac{bp}{RT}$$

4.2.5 Comparison of the Different Equations Of State

Eq. 4.1 of Ideal Gas, Eq. 4.6 of Peng-Robinson and Eq. 4.9 of Soave-Redlich-Kwong are implemented in *Matlab*[2] to compute the density (over the temperature) of the species involved in the reaction at constant pressure equal to the chamber pressure. The results are presented compared to *NIST* real gas values taken from *NIST* database [9]. Moreover, to estimate the most suitable equation, an error estimation of the reactants' densities at inlet condition is conducted.

In the current section only the methane and oxygen density plots are included. The plots for the other species involved in the global reaction (Eq. 2.2) can be found in Appendix A.

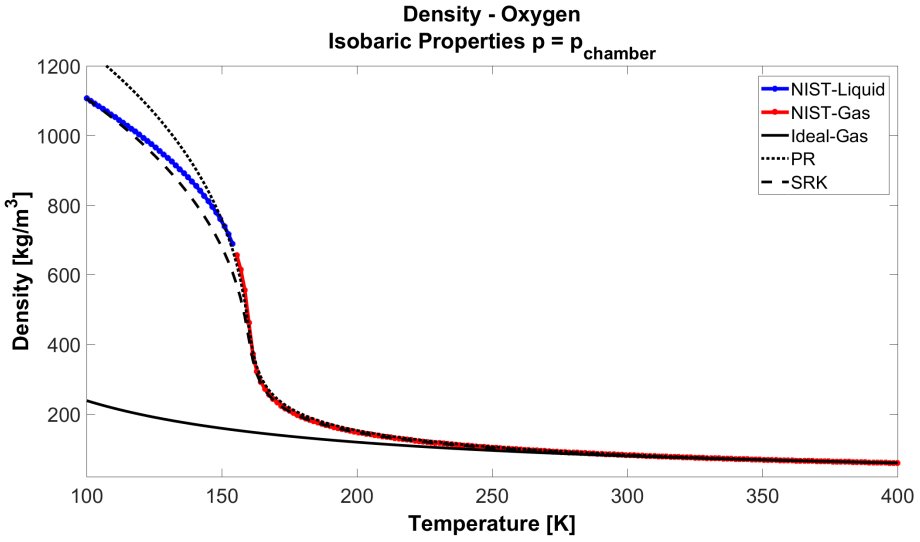

FIGURE 4.3: Oxygen Density/Temperature Plot

[2]The Matlab scripts cannot be shown for corporate data security policies.

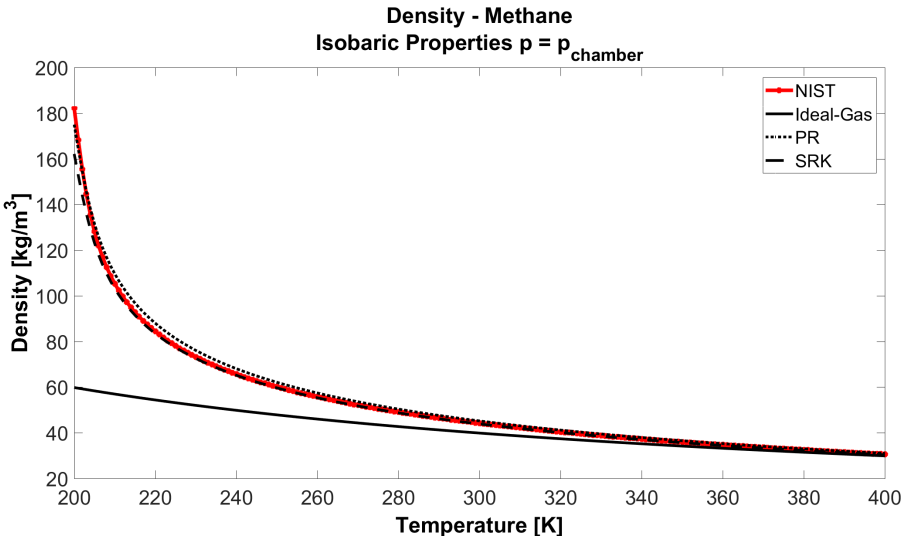

FIGURE 4.4: Methane Density/Temperature Plot

From the above plots the conclusion of using Soave-Redlich-Kwong equation of state is taken. In particular Fig. 4.3 shows that in the oxygen case the *SRK EOS* is the most suitable to replicate the real condition of the flow. Moreover, as *LOX* is injected in the chamber, in some cases also a minor amount of liquid nitrogen is dissolved into the oxygen to stabilize its liquid form [33]. Taking a look of Fig. A.3 (nitrogen density), it can be seen that the liquid form is better described by *SRK EOS* than the others methods.

In order to validate these considerations based on the density plots, the results of an error estimation at inlet condition are presented in Tab. 4.1 and 4.2.

EOS/Error type	Absolute Error $[Kg/m^3]$	Relative Error [%]
Ideal Gas	841.99	79.37
PR	127.49	12.02
SRK	**7.24**	**0.68**

TABLE 4.1: Oxygen Density Error Estimation at inlet condition

EOS/Error type	Absolute Error $[Kg/m^3]$	Relative Error [%]
Ideal Gas	12.25	20.38
PR	2.02	3.36
SRK	**0.43**	**0.72**

TABLE 4.2: Methane Density Error Estimation at inlet condition

The absolute and relative errors are calculated respectively with Eq. 4.10 and 4.11:

$$Absolute\ Error = |\phi - \phi_{real}|, \tag{4.10}$$

$$Relative\ Error = \frac{|\phi - \phi_{real}|}{\phi_{real}} \cdot 100, \tag{4.11}$$

where ϕ is the generic property (density in this case) at the inlet temperature computed with the different methods and $\phi_{NIST} = \phi_{real}$ is the proper value from *NIST* real gas database [9]. The density values of methane and oxygen at inlet condition are also compared to the simulations' results in Section 5.1

For the products of the global reaction (carbon dioxide and water-vapour), no relevant differences of using any particular methods are recognised from the plots in Appendix A.1. In fact, at high temperature when the products are created, there are no relevant differences between ideal and real gas behaviour. The best topic is to simulate the correct value of the

density at inlet condition and during the reaction process. As a result of this analysis, *SRK EOS* density method will be used in Fluent for simulation requiring real gas treatment.

4.3 Transport and Thermodynamic Properties

The model of the thermodynamic properties in a combustion chamber has a significant impact on the simulation results. Some properties of the gas mixture cannot easily be defined from the properties of its components. Fluent defines the properties of multicomponent mixture using a mass averaging, by which the contribution of the individual components to the properties of the mixture is directly proportional to the mass fraction [40].
Five species are involved in the global reaction (Eq. 2.2) and the mass averaging mixing law (Eq. 4.12) is used to compute the properties of the mixture.

$$\phi = \sum_{i=1}^{5} Y_i \phi_i, \tag{4.12}$$

ϕ is the generic thermodynamic or transport property of the mixture, Y_i and ϕ_i the species i mass fraction and its properties value. The property ϕ_i for each involved species has to be defined within Ansys Fluent.

The topic is to determine the best method to simulate the thermodynamic and transport properties of the mixture. The fundamental problem of the present case is the reactants are injected close to the critical conditions. In this region the properties do not have a regular behaviour and simulating it correctly is really difficult and challenging.

The attention is given to the definition of *heat capacity* (c_p), *thermal conductivity* (λ) and *dynamic viscosity* (μ). No special attention is put into the mass transfer, instead the standard approach of using the kinetic theory in the ideal gas simulation and a constant dilute approximation in the *SRK* simulations has been chosen. The data from *NIST* real gas WebBook [9] are taken as reference values and different methods are analysed to find the best method that fits with the *NIST* values. The data are compared graphically and the properties values of the propellants at inlet condition are described in detail.

4.3.1 Dynamic Viscosity and Thermal Conductivity

In order to analyse the transport properties the same computational methods will be taken into account. The *NIST* data are compared with the results that come from:

- Sutherland-Law;
- Power-Law;
- CEA Transport Property Coefficients;
- Own piecewise polynomials (further explained).

Sutherland-Law

Sutherland's viscosity law resulted from the kinetic theory by Sutherland (1893) using an idealized intermolecular-force potential. The formula is specified using two or three coefficients [32]. Sutherland's law with two coefficients has the form:

$$\mu = \frac{C_1 T^{3/2}}{T + C_2}, \tag{4.13}$$

where μ is the viscosity $[kg/m*s]$, T the static temperature $[K]$ and C_1, C_2 the coefficients.
Sutherland's law with three coefficients has the form:

$$\mu = \mu_0 \left(\frac{T}{T_0}\right)^{3/2} \frac{T_0 + S}{T + S} \tag{4.14}$$

where μ_0 is the reference viscosity $[kg/m*s]$, T_0 the reference temperature $[K]$ and S an effective temperature (Sutherland constant) $[K]$ [32].

Power-Law

Another common approximation for the viscosity of dilute gases is the power-law form. For dilute gases at moderate temperatures, this form is considered to be slightly less accurate than Sutherland's law [32].
The power-law with two coefficients has the form:

$$\mu = BT^n \tag{4.15}$$

where B is a dimensional coefficient and n the power coefficient.
The power-law with three coefficients has the form:

$$\mu = \mu_0 \left(\frac{T}{T_0}\right)^n \tag{4.16}$$

where μ_0 is the reference viscosity $[kg/m-s]$ and T_0 the reference temperature $[K]$ [32].

The same equations can be used to simulate the thermal conductivity. The reference and constant values need to be changed accordingly and they can be taken from the literature for oxygen, nitrogen and carbon dioxide [19]. Regarding methane and water-vapor, the Sutherland's and power laws three coefficients are not taken from any literature source. They were created "by-hand" trying to fit the *NIST* real gas data, in particular at inlet condition.

CEA Transport Property Coefficients

The values of the properties function of temperatures are taken also by the NASA Lewis Research Center's Chemical Equilibrium and Applications Program (*CEA*) in which the coefficients, that describe the values of dynamic viscosity and thermal conductivity, were generated by a least-squares fit to the following equation [37]:

$$\left.\begin{matrix} ln(\mu) \\ ln(\lambda) \end{matrix}\right\} = Aln(T) + \frac{B}{T} + \frac{C}{T^2} + D \tag{4.17}$$

In Eq. 4.17, T is the temperature, μ the viscosity and λ the thermal conductivity. A, B, C, and D are constants obtained by fitting the data. The constants were fitted to generate the viscosity in units of micropoise [3] ($\mu g/cm \cdot s$) and the conductivity in units of microwatts per centimetre kelvin ($\mu W/cm \cdot K$) [37].
Coefficients were generated for two temperature intervals, usually 300 to 1000K and 1000 to 5000K. Typically, each species has four sets of coefficients: two sets for viscosity and two sets for conductivity (low- and high- temperature intervals for each) [37].

Comparison of the Different Methods

Eq. 4.14, 4.16 and 4.17, respectively for Sutherland (3 coefficients), power-law (3 coefficients) and *CEA*, are implemented in *Matlab*. They are plotted in comparison with *NIST* real gas values and Fluent default parameters [4]. The piecewise-polynomial functions were created trying to best fit the experimental *NIST* data.

[3] 1 micropoise $[\mu P] = 10^{-7} \quad Pa \cdot s$
[4] As done in Section 4.2.5, the plots of the products can be found in A.3

Dynamic Viscosity

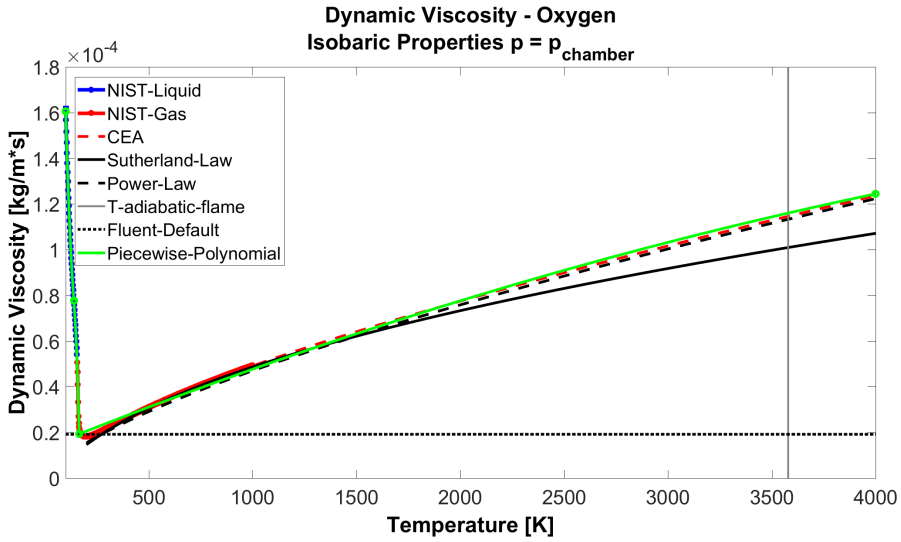

FIGURE 4.5: Oxygen Dynamic Viscosity/Temperature Plot

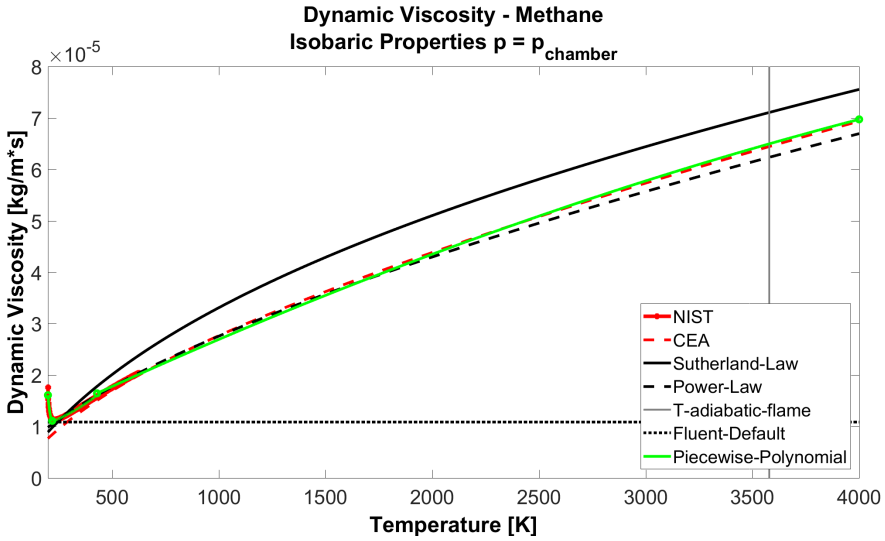

FIGURE 4.6: Methane Dynamic Viscosity/Temperature Plot

The injection condition of the reactants is taken into account and in particular an error estimation of the different methods is done. In Tab. 4.3, the dynamic viscosity at inlet condition is reported considering the different implemented methods.

Viscosity $[Kg/m*s]$	Oxygen	Methane
NIST	**1.3381e-04**	**1.1489e-05**
Sutherland	1.4624e-05	1.1065e-05
Power	1.5482e-05	1.1352e-05
CEA	1.4729e-05	9.5126e-06
Fluent-default	1.9190e-05	1.0870e-05
Polynomials	**1.3787e-04**	**1.1896e-05**

TABLE 4.3: Methane and Oxygen Dynamic Viscosity at inlet condition

An absolute and relative error of the different discussed methods are calculated using Eq. 4.10 and 4.11. The results are written in Tab. 4.4 and 4.5.

Method/Error type	Absolute Error $[Kg/m*s]$	Relative Error [%]
Sutherland	1.1919e-04	89.07
Power	1.1833e-04	88.43
CEA code	1.1908e-04	88.99
Fluent-default	1.1462e-04	85.66
Polynomials	**4.0589e-06**	**3.03**

TABLE 4.4: Oxygen Dynamic Viscosity Error Estimation at inlet condition

Method/Error type	Absolute Error $[Kg/m*s]$	Relative Error [%]
Sutherland	4.2375e-07	3.69
Power	1.3679e-07	1.19
CEA code	1.9764e-06	17.20
Fluent-default	6.1900e-07	5.39
Polynomials	**4.0733e-07**	**3.55**

TABLE 4.5: Methane Dynamic Viscosity Error Estimation at inlet condition

Tab. 4.5 shows that the Sutherland and the Power-law method predict the value of viscosity for methane better at inlet condition than the other methods. The reference parameters for the methane case are created "by hand" because no literature sources were found for this specie. This allows to have the best fit at inlet condition but an high error when the temperature changes.

Thermal Conductivity

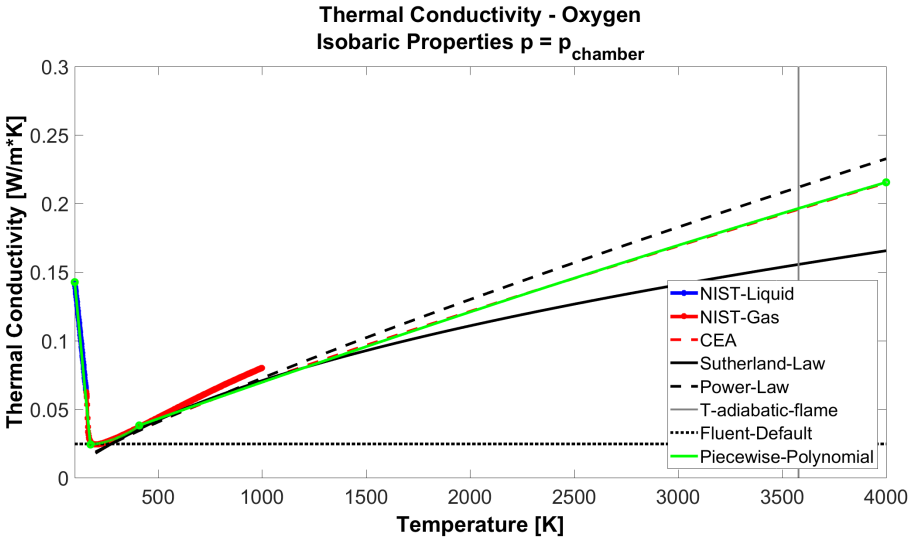

FIGURE 4.7: Oxygen Thermal Conductivity/Temperature Plot

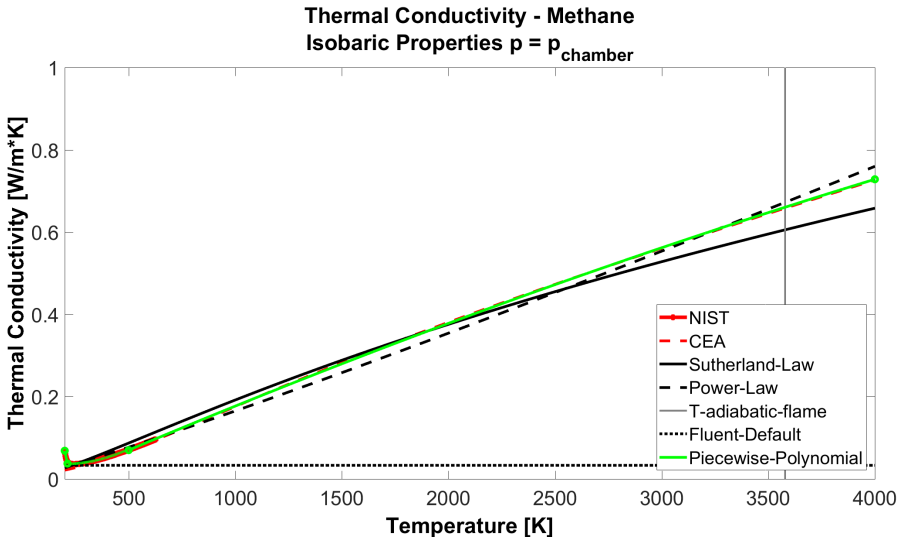

FIGURE 4.8: Methane Thermal Conductivity/Temperature Plot

As done for the dynamic viscosity analysis, first the thermal conductivity at inlet condition is reported in Tab. 4.6 and then an error estimation is conducted. Tab. 4.7 and 4.8 show the results.

Thermal Conductivity $[W/m*K]$	Oxygen	Methane
NIST	**1.3003e-01**	**3.5986e-02**
Sutherland	1.7838e-02	3.5986e-02
Power	1.8788e-02	3.5986e-02
CEA	1.8123e-02	2.7431e-02
Fluent-default	2.4600e-02	3.3200e-02
Polynomials	**1.3033e-01**	**3.8051e-02**

TABLE 4.6: Methane and Oxygen Thermal Conductivity at inlet condition

Method/Error type	Absolute Error $[W/m*K]$	Relative Error $[\%]$
Sutherland	1.1219e-01	86.28
Power	1.1124e-01	85.55
CEA code	1.1191e-01	86.06
Fluent-default	1.0543e-01	81.08
Polynomials	**3.0185e-04**	**0.23**

TABLE 4.7: Oxygen Thermal Conductivity Error Estimation at inlet condition

Method/Error type	Absolute Error $[W/m*K]$	Relative Error $[\%]$
Sutherland	0	0
Power	0	0
CEA code	8.5550e-03	23.77
Fluent-default	2.7860e-03	7.74
Polynomials	**2.0652e-03**	**5.74**

TABLE 4.8: Methane Thermal Conductivity Error Estimation at inlet condition

The errors equal to zero that are present in Tab 4.8 are a result of the fact that the reference values of temperatures and thermal conductivity for Sutherland and Power-law have been taken equal to the values of the properties at inlet condition. Therefore, using these methods, errors are not present but Fig. 4.8 shows that the results are unreliable at different temperature condition.

Why were the piecewise polynomials functions created? First, a comparison without the polynomials was done. The goal was to determine the best method. However, looking especially at Fig. 4.5 and 4.7 (dynamic viscosity and thermal conductivity of the oxygen), the decision to create a new piecewise-polynomials functions was taken. These functions are used to incorporate the strongly non-linear behaviour of the properties of species within the mixing to have a fluid behaviour closer to the reality.

The results in Section 5.1 will confirm this choice, as the values of the properties are similar to the simulations' results using the *NIST* database [9]. In particular, in order to validate the method, the analytic dynamic viscosity and thermal conductivity of the reactants at the inlet temperatures (reported in Tab. 4.3 and 4.6 for oxygen and methane respectively) will be compared in Section 5.1 to the Fluent results. Moreover, the current study is conducted especially because unfortunately the *NIST* database is no available for reacting and/or mixed flows in Ansys Fluent 19.2. In this Fluent version it is also not possible to import RefProp tables to compute the properties of the species.

4.3.2 Specific Heat Capacity

Under transcritical and supercritical conditions, thermophysical properties such as internal energy, enthalpy and constant pressure specific heat are calculated as the sums of an ideal gas reference value at the same temperature and a departure function. Departure function relates the difference between the high-pressure thermodynamic state and its value at standard atmospheric pressure. These thermodynamic quantities are state properties, so they only depend on their initial and final state, not on the path between these states. Therefore, the departure functions are exact description of the real fluid effects [3].

The specific formulations are described as,

$$e(T,P) = e_0(T) + \int_{\rho_0}^{\rho} \left[\frac{P}{\rho^2} + \frac{T}{\rho^2} \left(\frac{\partial P}{\partial T} \right)_\rho \right]_T d\rho \tag{4.18}$$

$$h(T,P) = h_0(T) + \int_{P_0}^{P} \left[\frac{1}{\rho} + \frac{T}{\rho^2} \left(\frac{\partial \rho}{\partial T} \right)_P \right]_T dP \tag{4.19}$$

$$c_p(T,\rho) = c_{P_0}(T) - \int_{\rho_0}^{\rho} \left[\frac{T}{\rho^2} \left(\frac{\partial^2 \rho}{\partial T^2} \right)_\rho \right]_T d\rho + \frac{T}{\rho^2} \frac{\left(\frac{\partial^2 \rho}{\partial T^2} \right)_\rho}{\left(\frac{\partial P}{\partial \rho} \right)_T} \tag{4.20}$$

The subscript 0 represent the ideal state and the departure functions on the right hand side are determined using a real fluid equation of state (*SRK EOS*).

If ideal gas simulations are conducted, only the ideal part of Eq. 4.18, 4.19 and 4.20 is considered. The ideal heat capacity $c_{P_0}(T)$ has to be modelled within the Fluent solver.
The Fluent-default to model the ideal heat capacity are piecewise-polynomial functions and the values of the properties obtained with these functions are compared to the *NASA* values (derived from the *NASA* polynomial functions) to understand if they are reliable or not. Moreover, other piecewise-polynomial functions, showed in the following figures, are implemented in Fluent to keep the heat capacity of the ideal gas solution close to the real gas one as much as possible. The goal is to avoid high discontinuity in the value of the heat capacity between ideal and real gas simulation, especially because the ideal gas results could be used to initialize the real gas simulation. This is a useful method, often suggested, in order to to start the real gas simulation when a reliable shape of the flame is already obtained.

NASA Polynomials

The NASA polynomials have the form:

$$Cp/R = a_1 + a_2 T + a_3 T^2 + a_4 T^3 + a_5 T^4,$$

$$H/RT = a_1 + a_2 T/2 + a_3 T^2/3 + a_4 T^3/4 + (a_5 T^4)/5 + a_6/T,$$

$$S/R = a_1 lnT + a_2 T + a_3 T^2/2 + a_4 T^3/3 + a_5 T^4/4 + a_7,$$

where a_1, a_2, a_3, a_4, a_5, a_6, and a_7 are numerical coefficients supplied in *NASA* thermodynamic files [22]. Looking into them, it is possible to note that there are two sets of coefficients, one for low temperature (below 1000K) and the other one for high temperature (above 1000 K).

In Fig. 4.9 and 4.10, the *NIST* real gas data [9] are plotted to understand the difference between the ideal and real behaviour of the gas[5]. The *NIST* data will be compared to the simulation results of the injectors in Section 5.1 to verify how the departure functions work and in order to establish if the results are reliable enough or not.

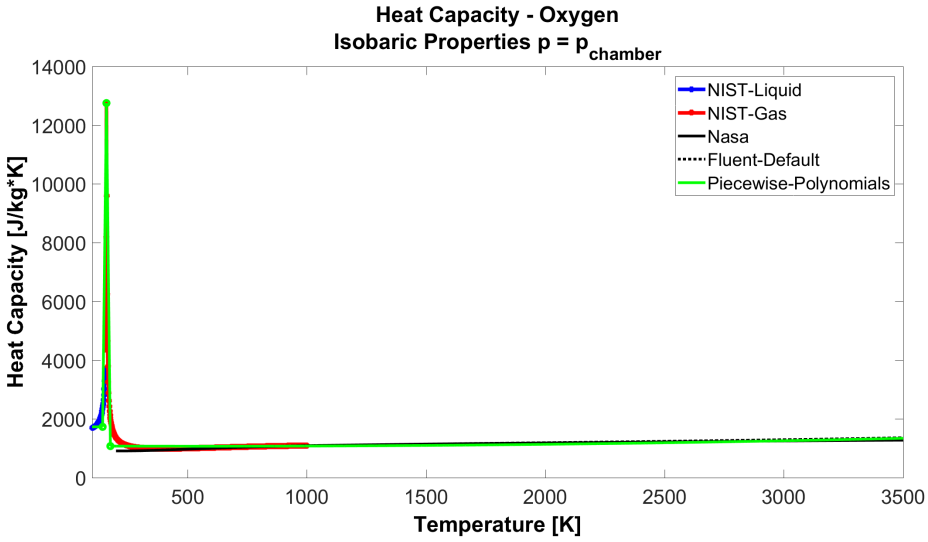

FIGURE 4.9: Oxygen Heat Capacity/Temperature Plot

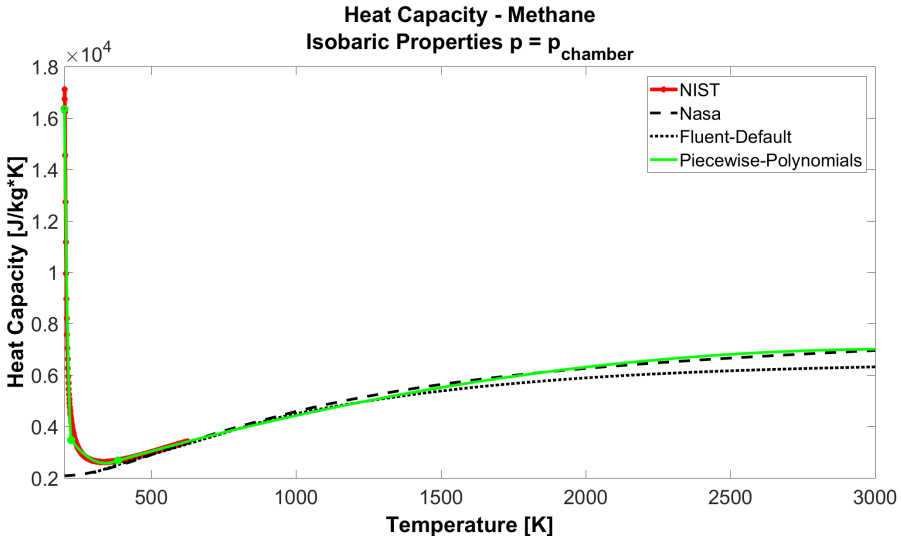

FIGURE 4.10: Methane Heat Capacity/Temperature Plot

The previous figures show that the Fluent-default piecewise-polynomials are substantially the NASA piecewise-polynomials and the choice to utilize them to simulate the ideal heat capacity of the species is taken.

The values of heat capacity at inlet condition are computed and an error estimation is conducted. Tab. 4.9, 4.10 and 4.11 show the calculated values.

[5]Further plots for other species involved in the reaction can be found in A.4.

Heat Capacity $[J/Kg*K]$	Oxygen	Methane
NIST	**1732.10**	**3110.10**
NASA	910.66	2131.98
Fluent-default	916.63	2197.89
Polynomials	**1731.10**	**2886.3**

TABLE 4.9: Methane and Oxygen Heat Capacity at inlet condition

Method/Error type	Absolute Error $[J/Kg*K]$	Relative Error [%]
NASA polynomials	8.2144e+02	47.42
Fluent-default	8.1547e+02	47.08
Polynomials	**0.9667**	**0.06**

TABLE 4.10: Oxygen Heat Capacity Error Estimation at inlet condition

Method/Error type	Absolute Error $[J/Kg*K]$	Relative Error [%]
NASA polynomials	9.7812e+02	31.45
Fluent-default	9.1221e+02	29.33
Polynomials	**2.2382e+02**	**7.19**

TABLE 4.11: Methane Heat Capacity Error Estimation at inlet condition

4.4 Mixture Density Computation

It is important to think about the state of all the species in the mixture in particular thermodynamic conditions in order to understand what is happening in the combustor during the simulations. The states at which a pure material can exist can be graphically represented in diagrams of pressure vs. temperature (PT diagrams in Fig. 4.11) and pressure vs. molecular or specific volume (PV diagrams in Fig. 4.12). Homogeneous fluids are normally divided in two classes, liquids and gases. However the distinction cannot always be sharply drawn, because the two phases become indistinguishable at what is called the critical point.

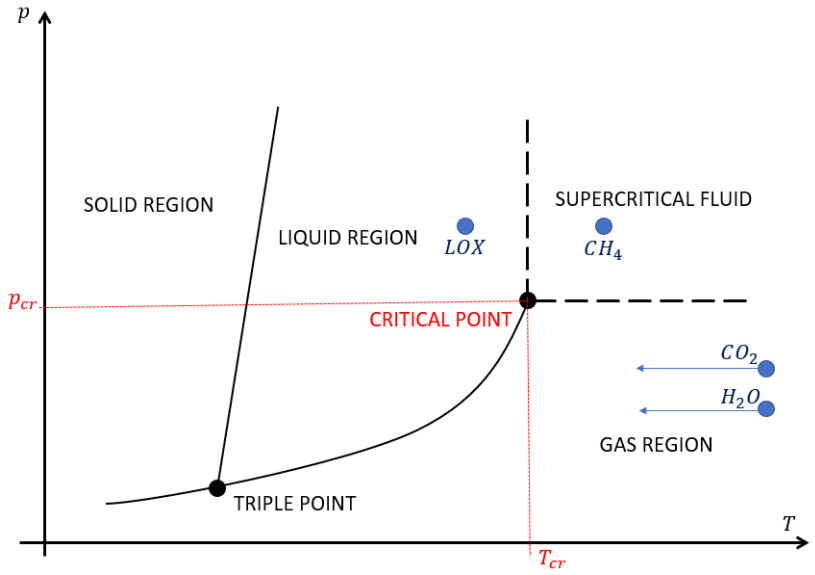

FIGURE 4.11: Typical PT Diagram of a Pure Specie

The diagram in Fig. 4.11 shows the single phase regions, as well as the conditions of P and T where two phases coexist. The solid and the gas region are divided by the sublimation curve, the liquid and gas regions by the vaporization curve, and the solid and liquid regions by the fusion curve. The three curves meet at the triple point, where all three phases can coexist in equilibrium [27]. Although the fusion curve continues upward indefinitely, the vaporization curve terminates at the critical point. The coordinates of this point are called

critical pressure p_c and critical temperature T_c. These represent the highest temperature and pressure at which a pure material can exist in vapour-liquid equilibrium. At temperatures and pressures above the critical point, the physical property differences that differentiate the liquid phase from the gas phase become less defined. This reflects the fact that, at extremely high temperatures and pressures, the liquid and gaseous phases become indistinguishable. This new phase, which has some properties that are similar to a liquid and some properties that are similar to a gas, is called a supercritical fluid [27].

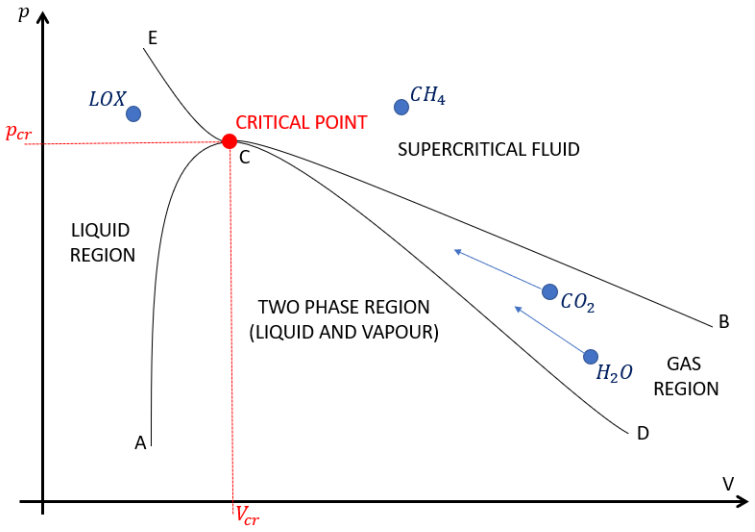

FIGURE 4.12: Typical PV Diagram of a Pure Specie

Fig. 4.12 presents a typical diagram of pressure versus molar or specific volume (PV diagram) of a pure material. The dome shaped curve ACD is called the saturation dome and separates the single phase regions in the diagram; curve AC represents the saturated liquid and curve CD the saturated vapour. The area under the saturation dome ACD is the two-phase region and represents all possible mixtures of vapour and liquid in equilibrium. Curve ECB is the critical isotherm and exhibits a horizontal inflection at point C at the top of the dome. This is the critical point. The specific volume corresponding to the critical point, is called the critical specific volume V_c. The conditions to the right of the critical isotherm ECB correspond to supercritical fluid [27].

In Fig. 4.11 and 4.12 it is important to note where the species involved in the global reaction (Eq. 2.2) are located to understand why some problems appear in the simulation. Oxygen is injected at transcritical condition (above the critical pressure but below the critical temperature) while methane is injected at supercritical condition. In both case, Fluent is able to predict the fluid's behaviour because the most important thing is that the pressure is above the critical one to avoid the possibility of having phase change.
The Fluent solver gets unsuitable results if the fluid is located inside the two phase region, which can happen only if the pressure is below the critical one [38].
Tab. 4.12 shows the critical properties (temperatures and pressures) of the species involved in the global reaction (Eq. 2.2) and an important consideration has to be done.

Species	T_c $[K]$	p_c $[bar]$
Oxygen	154.58	50.43
Methane	190.56	45.99
Nitrogen	126.2	34
Carbon Dioxide	304.21	73.83
Water-Vapour	647.1	220.64

TABLE 4.12: Critical Point Coordinates

When the combustion is simulated, all the five species are contemporary in the chamber. The chamber pressure is fixed equal to the chamber experimental pressure by the pressure

outlet, whereas the temperature field is in evolution during the simulation. A final state will be reached but also the intermediate state are important for the consistency of the solver. As Fig. 4.11 and 4.12 show, the products (water-vapour and carbon dioxide) are unfortunately in subcritical condition: the chamber pressure is lower than the critical one of each of the two species. For this reason, an high temperature is needed to not enter into the saturation domain.
Where and When does the problem of two phase flow appear? A single step reaction is considered, so carbon dioxide and water-vapour are directly created when the propellants react. In the flame front, as explained in Chapter 2, intermediate species are not considered and the final products are present. In this way, the water comes in direct contact with the liquid oxygen that cools down the temperature of the mixture. Moreover, the products increase the critical pressure of the mixture and the mixture can fall into the subcritical condition. Therefore, in the flame front, the risk of having a two phase flow takes form and it creates a big issue in the simulation.

The density computation of a real gas mixture will be done using SRK EOS as for a pure component, to which appropriate critical constants are assigned. These mixture critical constants are functions of the mixture composition and pure component critical properties, and are sometimes called pseudocritical constants, because their values are generally expected to be different from the true mixture critical constants that may be determined experimentally [3].
The critical coordinates of the mixture were calculated using the pseudocritical method based on the one fluid Van der Waals mixing rule, which treats the properties of a mixture as that of a pure component. In this method the coefficients a and b in Section 4.2.4 are replaced by composition dependent expressions as follows [38]:

$$\sqrt{a_m} = \sum_{i=1}^{5} X_i \sqrt{a_i},$$

$$b_m = \sum_{i=1}^{5} X_i b_i,$$

where X_i is the mole fraction of component i, a_i and b_i are coefficients of component i; a_m and b_m are mixture coefficients.
The critical temperature T_c, critical pressure P_c, critical specific volume V_c, and acentric factor ω, are replaced by the corresponding mixture critical constants (T_{cm}, P_{cm}, V_{cm} and ω_m). The mixture acentric factor is computed in particular with a mole average mixing law (Eq. 4.21)

$$\omega_m = \sum_{i=1}^{5} X_i \omega_i, \tag{4.21}$$

where X_i is the mole fraction of the species i.
The values for the mixture's critical point are calculated instead with the one fluid Van Der Waals mixing rules as follows [38]

$$T_{cm} = \frac{\left[\sum_{i=1}^{5} \left(x_i \frac{T_{ci}}{p_{ci}^{0.5}} \right)\right]^2}{\sum_{i=1}^{5} \left(\frac{x_i T_{ci}}{p_{ci}} \right)} \tag{4.22}$$

$$p_{cm} = \frac{T_{cm}}{\sum_{i=1}^{5} \left(\frac{x_i T_{ci}}{p_{ci}} \right)} \tag{4.23}$$

$$V_{cm} = \sum_{i=1}^{5} \frac{x_i p_{ci} V_{ci}}{T_{ci}} \left(\frac{T_{cm}}{p_{cm}} \right) \tag{4.24}$$

The critical constants of the mixture are a function of the mixture composition and the critical constants of each species (Tab. 4.12). The mixture close to the flame front can enter the two phase region because the critical pressure of the mixture p_{cm} shifts above the chamber

pressure and the temperature in that specific region is below the critical temperature of the mixture T_{cm}. To circumvent the problem to temporarily drop below the critical point into the two phase regime, there are two simple solutions. Temporarily decrease T_{cm} or p_{cm}. The temperature in the chamber depends on the energy equation and production term, so the choice to not modify T_{cm} is taken. On the contrary, the pressure is fairly stable in the combustor (deflagration mode) and p_{cm} can be modified manually within Fluent, simply by adopting the critical pressure of the single species (Tab. 4.12). This means that by decreasing the critical pressure of water, the mixture could be kept in supercritical condition artificially.

Fig. 4.13 shows how the critical temperature and pressure of the mixing change as function of the critical temperature of water. Note that the composition of the mixture has a major role in the current work since the critical values depend on it. As reference the composition at the chamber exit is chosen as here the most water exists. It is taken from the Ideal Gas Combustion results in Section 5.2.2, doing an average on the outlet surface.

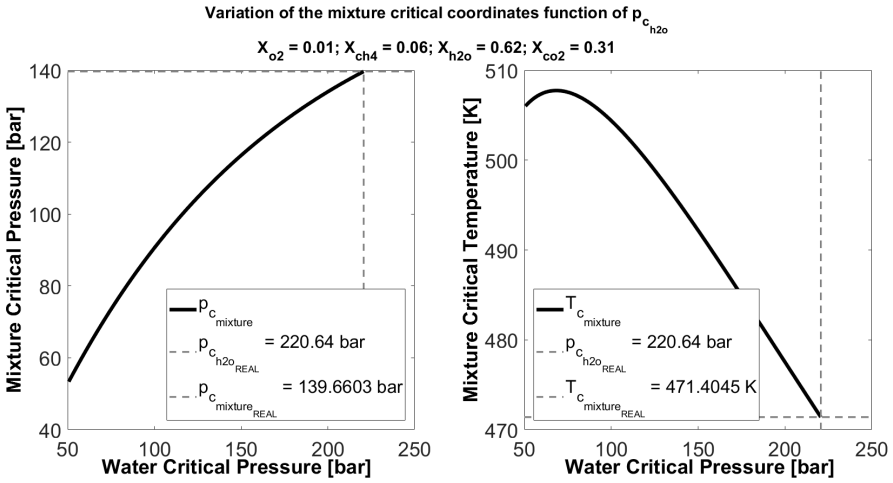

FIGURE 4.13: Variation Mixture Critical Properties

The goal is to decrease the mixture critical pressure below the chamber pressure. For this reason, the water critical pressure has to be reduced even if the mixture critical temperature increases. A parametric study is conducted to determine the mixture density behaviour in regards to $p_{c_{H_2O}}$ and $T_{mixture}$.

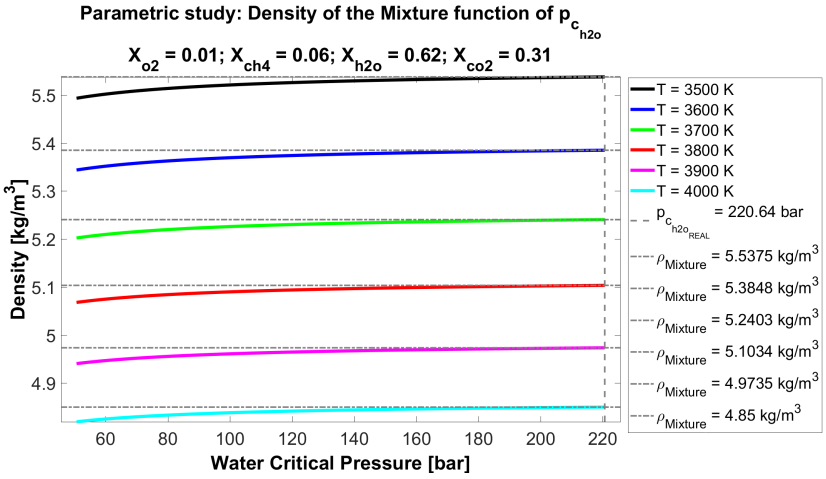

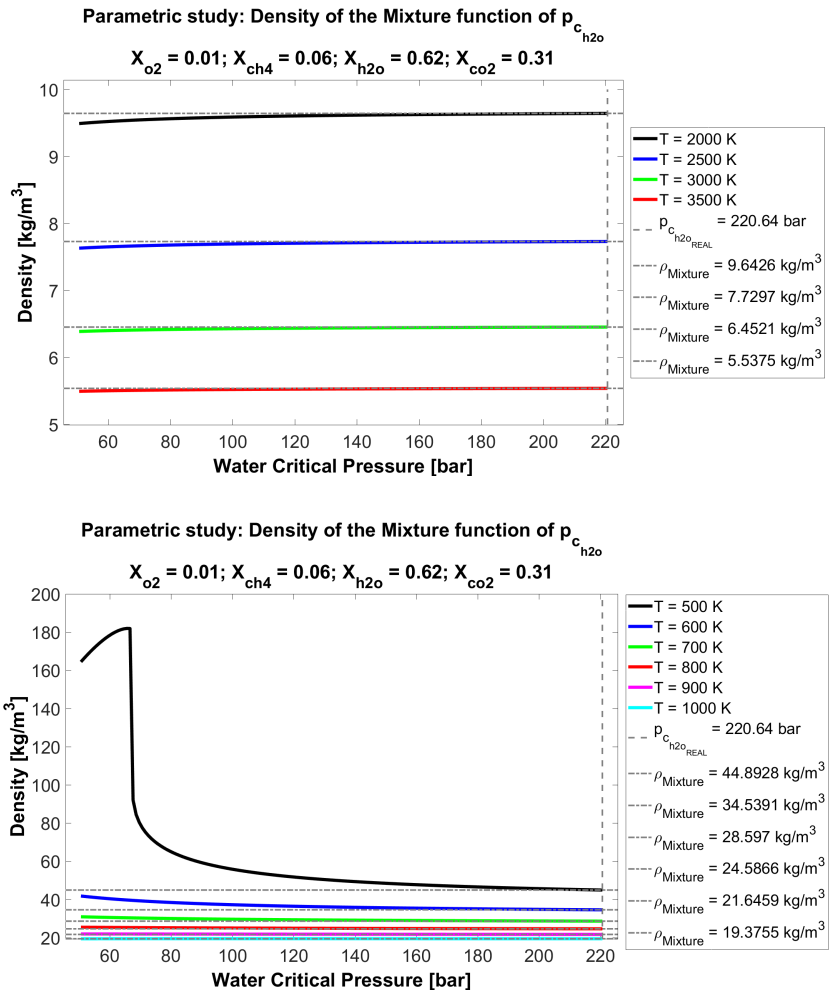

FIGURE 4.14: Mixture Density function of Water Critical Pressure

Fig. 4.14 show the mixture density versus the critical pressure of water at different temperatures. In particular two zoom in of specific temperature ranges (high and low mixture temperature) are illustrated. From Fig. 4.14 it could be noted that at low temperatures the mixture density starts to be overestimated when the water critical pressure decrease.

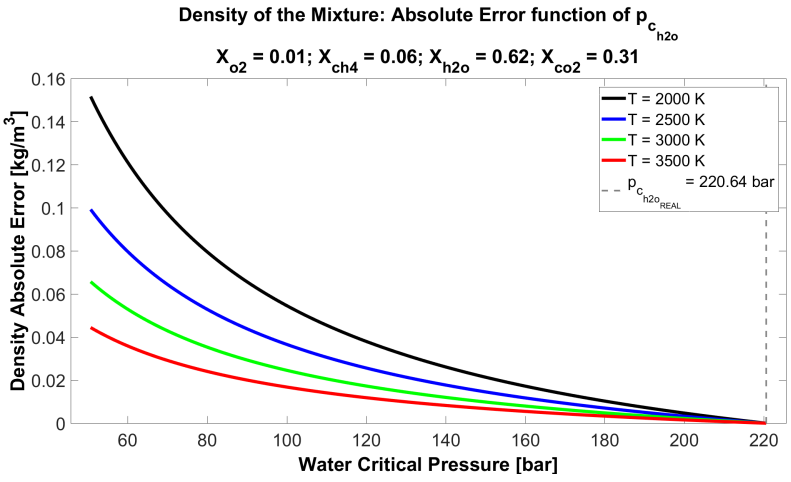

FIGURE 4.15: Mixture Density Absolute Error function of Water Critical Pressure

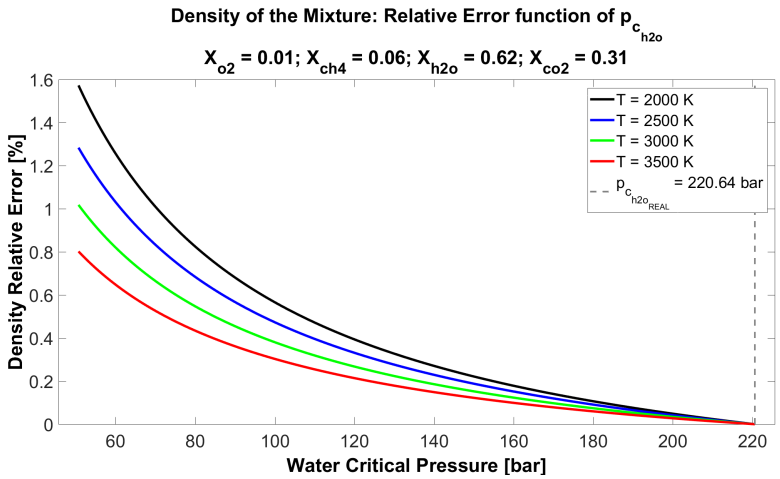

FIGURE 4.16: Mixture Density Relative Error function of Water Critical Pressure

Fig. 4.15 and 4.16 show the absolute and the relative error calculated using Eq. 4.10 and 4.11. As expected, more the critical pressure of water is decreased, more the error increases, in particular at low mixture temperature. At high temperature behaviour of the gas follows the ideal gas law and this effect is less relevant in the real gas computation.

Finally, the density of the mixture is plotted versus the mixture temperature where each line corresponds to a different critical pressure of water.

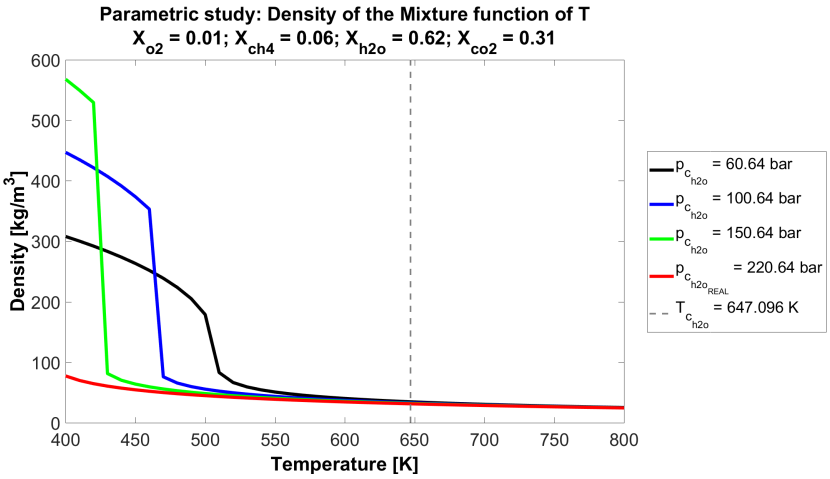

FIGURE 4.17: Mixture Density function of Temperature

Fig. 4.17 shows how a decrease of the critical pressure of water becomes more and more significant when the temperature decrease, as it was explained previously. This is confirmed also by the following Fig. 4.18 and 4.19 that represent the errors on the density computation in function of the temperature.

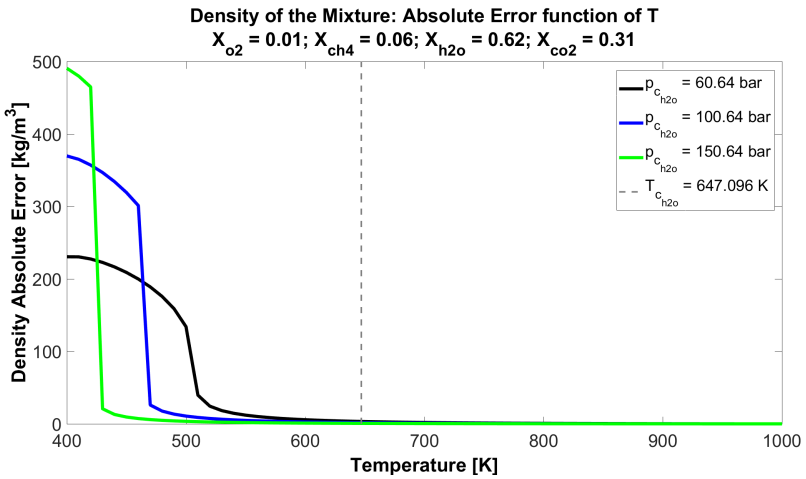

FIGURE 4.18: Mixture Density Absolute Error function of Temperature

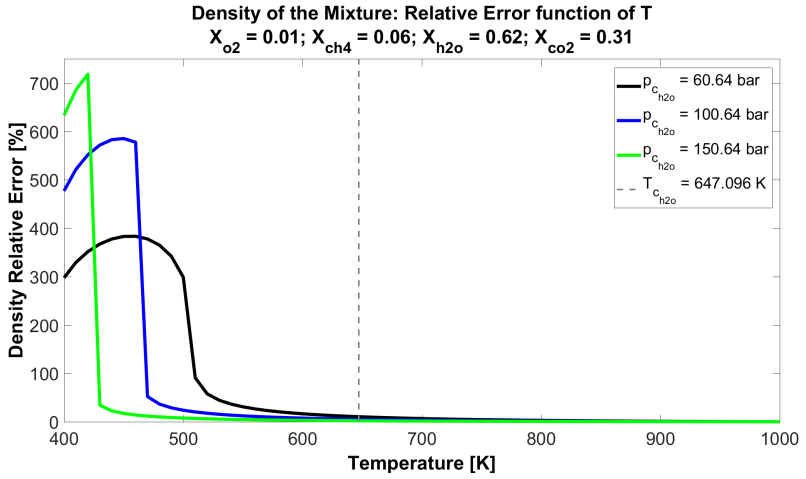

FIGURE 4.19: Mixture Density Relative Error function of Temperature

In order to complete the study, Fig. 4.20 shows a 2D plot that tries to include all the informations previously exposed.

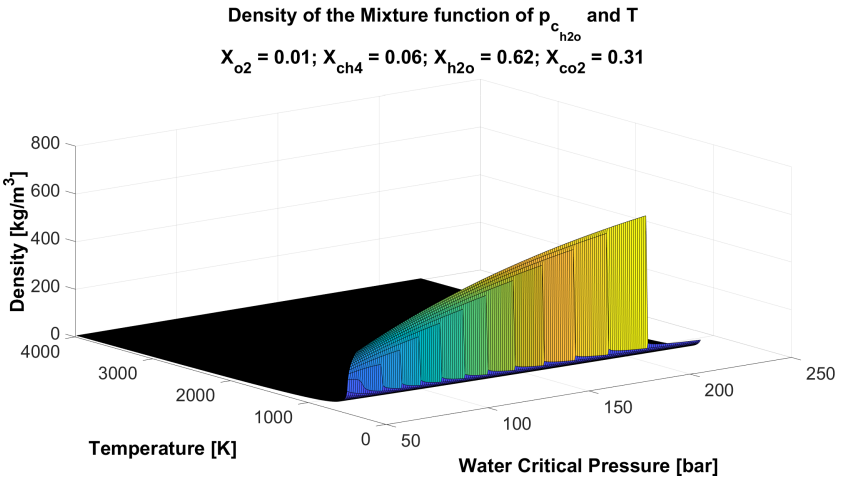

FIGURE 4.20: Mixture Density 2D Plot

Chapter 5

Results

The current Chapter is divided in two main Sections:

- Injectors (Section 5.1) in which the results of the methane (Section 5.1.1) and oxygen (Section 5.1.2) injectors are exposed;
- Combustion chamber (Section 5.2) in which the Mixing (Section 5.2.1) and the Combustion results (Section 5.2.2) are presented.

The results of the simulations will be compared to the results obtained in Chapter 2 and 4 where the combustion theory and the properties of the species were discussed in detail.

Before presenting any kind of results, the reference values are chosen for security data reason. The variables are so referred to the correspondent reference value chosen. Taking into account the Ideal Gas Combustion simulation with the inlet profiles as boundary conditions (Section 5.2.2), the reference variable are taken in correspondence of the outlet chamber surface doing an average of the exit values. Most part of the results will be presented graphically dividing the variables by its reference value.

5.1 Injectors

The simulations of the injectors are very important because they will be used as inlet condition in the combustion chamber. As showed in Section 3.2, the simulation of the combustion chamber is conducted considering only a sector of 45 degrees for symmetry reasons. In this domain, two coaxial injectors are included: one sector of 180 degrees and the other one of 45 degrees in the middle of the chamber. In order to simplify the coupling of the simulations in Ansys Fluent (between injectors and combustion chamber), the two coaxial injectors are simulated in the correct position. It means that the coordinates of the outlet surfaces of the injectors must coincide to the coordinates of the inlet surfaces of the chamber. In this way, the outlet profiles can be extrapolated by the simulations of injectors, and then they can be imported as inlet condition in the combustion chamber.

In order to be sure that the simulations of 180 and 45 degrees injectors sectors lead to the same results, a simple comparison study is done graphically and the resulting pictures can be found in Appendix B.1.1. In particular, no relevant differences are found in the outlet profiles. It means that equal inlet conditions are present in the combustion chamber and this is really important for the simulation's convergence.
Moreover, as it can be seen in the plots of the inlet and outlet surface contained in Appendix B.1.1, there are fundamental differences between inlet and outlet profiles. It is possible to note how the thermodynamic and turbulent variables vary along the injectors. The properties' variation across the pipes will be analysed in Section 5.1 and it will be possible to visualize how the turbulent flow develops. This is essential to understand why the simulations of the injectors are crucial; how they affect the combustion results and in particular the mixing process in the combustor. This will be shown in Section 5.2.2, considering the simple Ideal Gas Combustion with different inlet boundary conditions.

Then, two different simulations of the 180 degrees injectors sectors will be compared to understand how the density methods, the piecewise-polynomials functions and the departure functions work in Ansys Fluent. For this study, just the sectors of 180 degrees are taken into

account because previously it was demonstrated graphically how there are no relevant differences between the simulation results of the 180 and 45 degrees injector sectors.
The reference simulation is conducted using the *NIST* real gas database included in Ansys Fluent. The real gas simulations are instead conducted using *SRK EOS*. Piecewise-polynomial functions are implemented to compute the transport properties (dynamic viscosity and thermal conductivity), as explained in Section 4.3.1, and the heat capacity is computed with the departure functions, as exposed in Section 4.3.2. Therefore, in the injectors solutions, the density, the heat capacity and the transport properties are compared to the *NIST* real gas database computation. Reminding Chapter 4, Ansys Fluent results are compared with the *Matlab* ones.

5.1.1 Methane

First, the methane injector is analysed. As shown in Section 3.2, the injector of methane is a simple pipe. The plots included in the current Section are used in order to make a qualitative comparison between the two different simulations:

- *SRK EOS*, in which real gas law, piecewise-polynomials and departure functions are used;
- *NIST* database, in which *NIST* real gas data [9], included in Ansys Fluent, are used.

In order to plot the longitudinal and outlet profiles, the data are extrapolated in correspondence of the detection lines[1] showed in Fig. 5.1. The faceplate or injection plane is located in correspondence to x equal to 0.

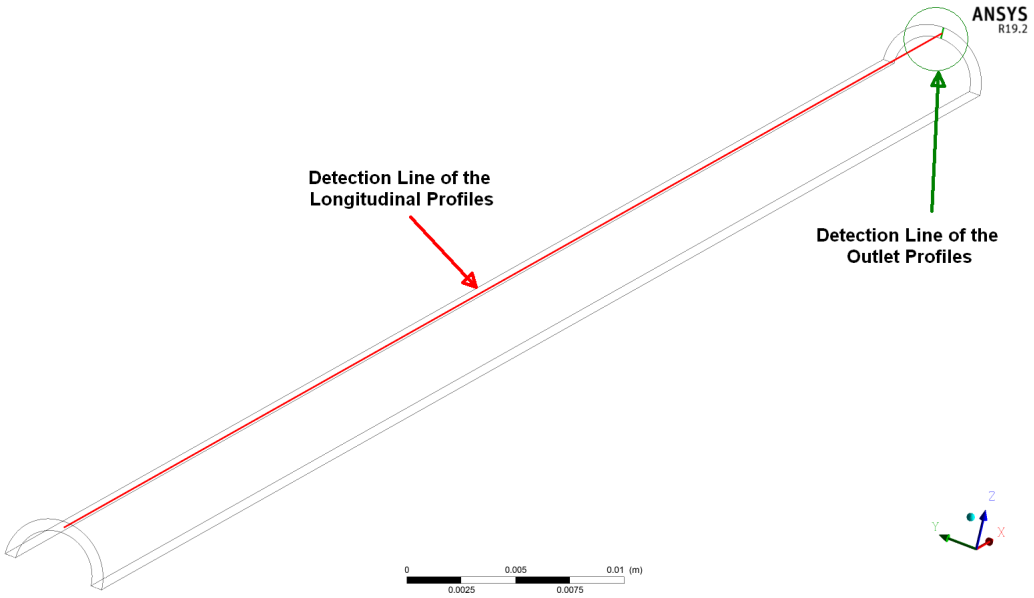

[1]Note that the longitudinal detection line (x-axis direction) is in the middle of the methane jet

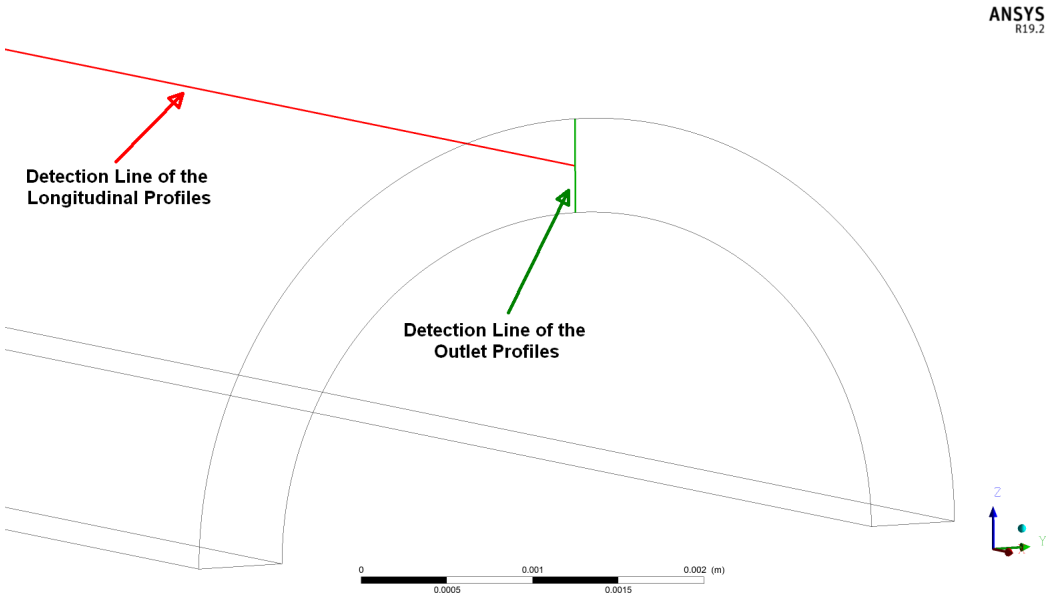

FIGURE 5.1: Detection Lines in the Methane Injector

Longitudinal Profiles

The properties behaviour along the injectors is discussed. Mass flow rate is imposed as inlet condition, so a velocity block is present on the inlet surface as it can be seen in Appendix B.1.1. The flow evolves during the path and the thermodynamic, transport and turbulent properties change along the longitudinal axis (x-axis in Fig. 5.1).

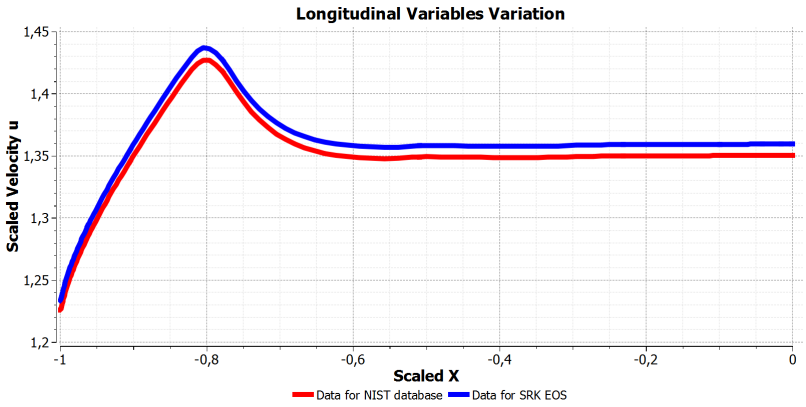

FIGURE 5.2: Methane Longitudinal Profile Velocity u

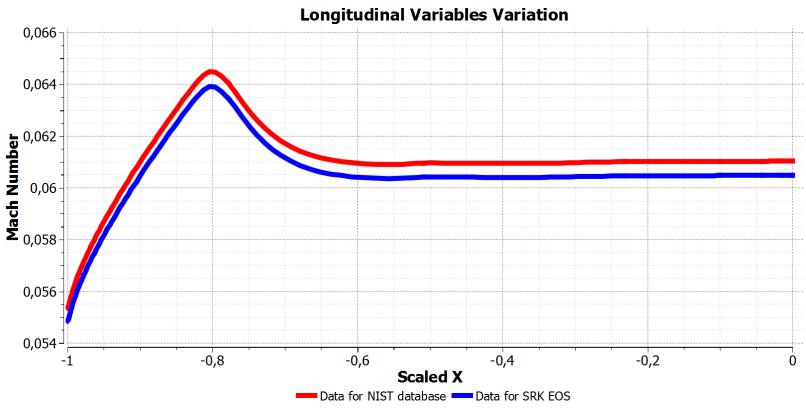

FIGURE 5.3: Methane Longitudinal Profile Mach Number

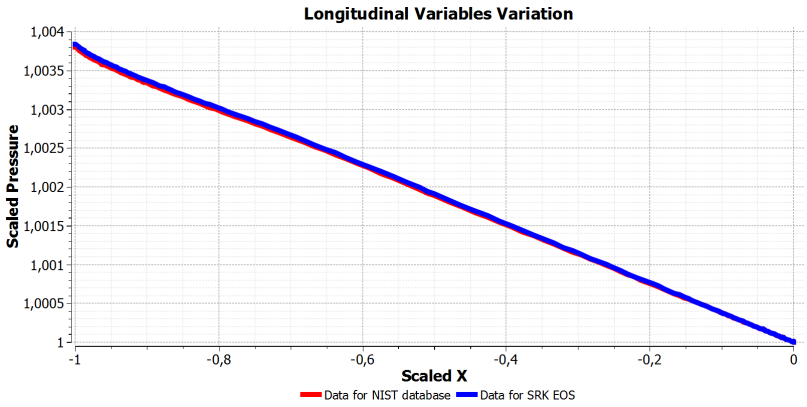

FIGURE 5.4: Methane Longitudinal Profile Pressure

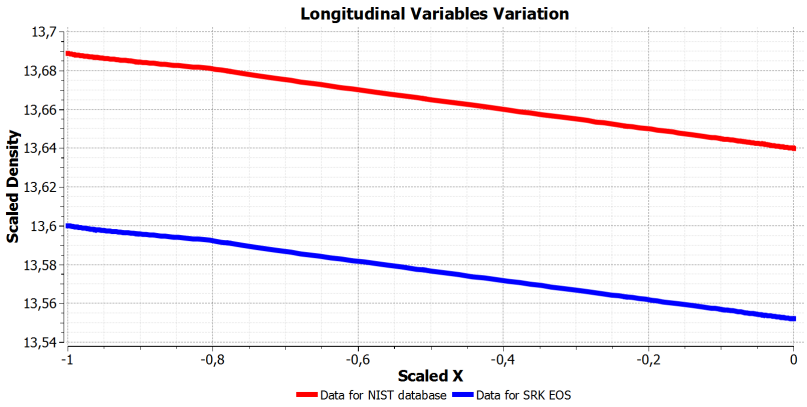

FIGURE 5.5: Methane Longitudinal Profile Density

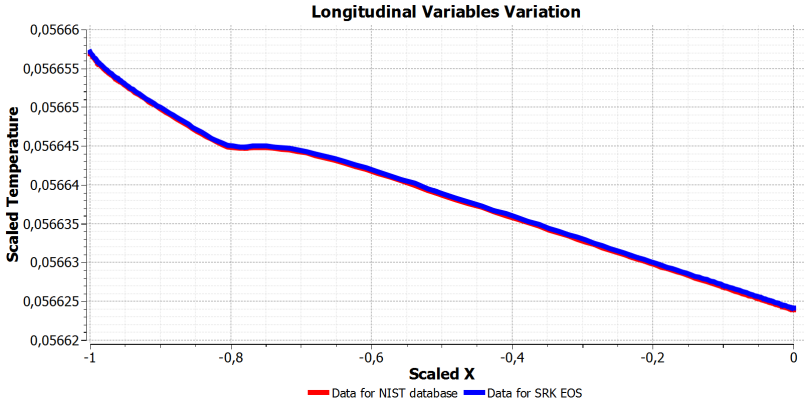

FIGURE 5.6: Methane Longitudinal Profile Temperature

Fig. 5.5 shows the density in the methane injector. Reminding the study done in Section 4.2.5, the predicted density in *Matlab* and the computed one in *Fluent* are compared. The comparison is done computing the relative error of the computed density respect to the predicted one. The results are shown in Tab. 5.1.

Method / Value	Relative Error %
NIST	0.0102
SRK	0.0108

TABLE 5.1: Methane Simulated Density Error Estimation at inlet condition

In both case the density is overestimated because the inlet temperature in the simulation is a little bit lower then the inlet temperature used in the computations done in Section 4.2.5. In

any case, the relative errors are very low and the results of simulation can be accepted. For this reason, the SRK EOS is acceptable to compute the density of the methane.

As expected considering a Fanno Flow, the density, temperature and pressure decrease across the injectors caused by the viscous force present especially near the wall. The viscous stress is the responsible for the behaviour of the velocity after inlet surface. The block velocity present in the inlet surface has to evolve across the injector. Therefore, in the middle core, the flow must accelerate to keep the mass flow rate constant considering that it must decelerate towards the wall until it reaches zero velocity magnitude at the wall. This is confirmed by the velocity profile shown in Fig. 5.15.

Fanno Flow: one-dimensional adiabatic flow with friction The Fanno flow is not the topic of the current work. However, it could be interesting analyse qualitatively the previous figures following the physical consideration behind the theory. It is just introduced and a little bit commented, only to understand the behaviour of the flow.

The Fanno Flow is a flow that develops inside a tube along L in an adiabatic way ($q = 0$) and in the presence of viscous effects ($\tau_\omega \neq 0$). The effects of viscosity translate into a distribution of frictional stress on the wall along the entire duct to be considered in the balance of the momentum. For an assigned input flow (subsonic in the current case) the conditions of the outflow depend on the length L of the duct that determines the entity of the resulting friction force acting on the walls of the duct. For a subsonic inlet flow, i.e., $M_{inlet} < 1$, the effect of friction on the downstream flow is such that [17]:

1. Mach number increases, $M_2 > M_1$ (Fig. 5.3);
2. Pressure decreases, $p_2 < p_l$ (Fig. 5.4);
3. Temperature decreases, $T_2 < T_1$ (Fig. 5.6);
4. Total pressure decreases, $p_{t2} < p_{t1}$;
5. Velocity increases, $u_2 > u_l$ (Fig. 5.2).

A subsonic flow in a duct in the presence of viscous effects accelerates: it may seem strange. The case of a supersonic flow that decelerates in the presence of friction in the duct may seem more plausible. This behaviour resides in the fact that a viscous flow near to the wall manifests all its effects through the presence of a viscous layer. It is precisely the viscous layer (boundary layer for a semi-guided flow) that grows as a thickness from the beginning to the end of the duct that brings the flow in the duct "to see" a decreasing cross-Section in the direction of its advancement. Fig. 5.7 shows the concept graphically: a subsonic inflow evolves into an "convergent" duct and accelerates as it happens into a classical nozzle.

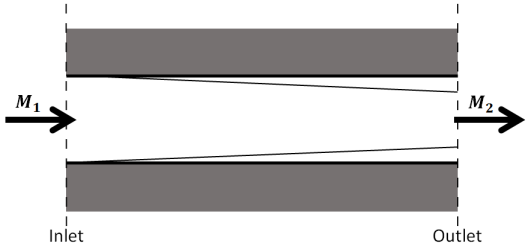

FIGURE 5.7: Fanno Flow: decreasing cross-section

Fig. 5.8 shows the velocity u (x-axis velocity) in the methane injector close to the inlet surface. In particular, it is possible to note how the behaviour predicted by the Fanno Flow (Fig. 5.7) is verified from the simulations (Fig. 5.8).

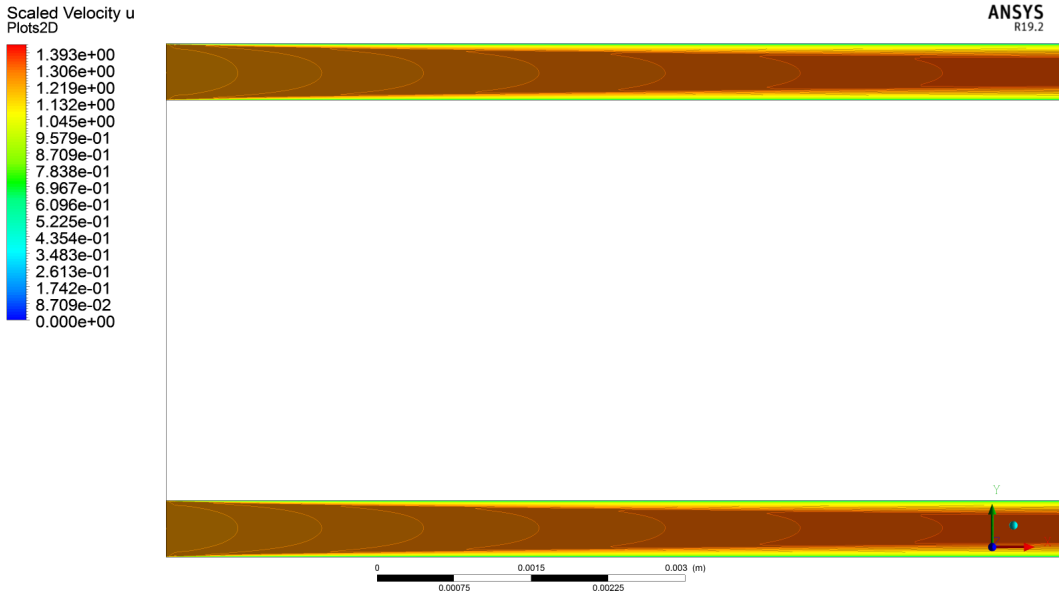

FIGURE 5.8: Methane Injector Velocity u

Due to their importance regarding the mixing process within the combustion chamber and the major influence the turbulent parameters have on the *EDM* combustion model, a brief overview on their behaviour inside the injector is presented here.

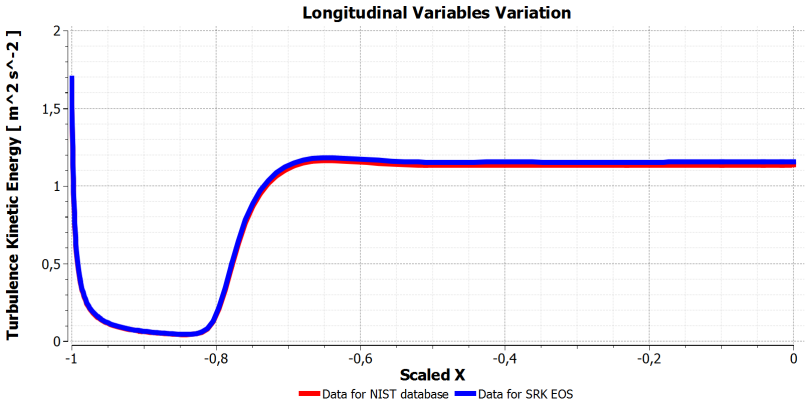

FIGURE 5.9: Methane Longitudinal Profile Turbulent Kinetic Energy

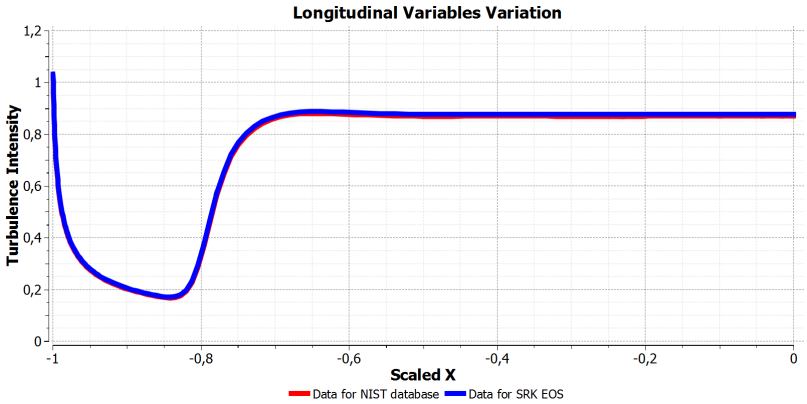

FIGURE 5.10: Methane Longitudinal Profile Turbulent Intensity

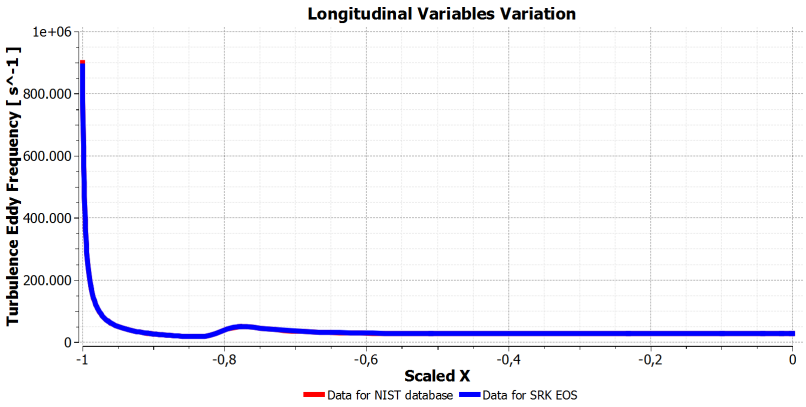

FIGURE 5.11: Methane Longitudinal Profile Turbulent Dissipation Rate

Fig. 5.9 shows the behaviour of turbulent intensity (k) in the injector pipe. Reminding Eq. 2.49 in which $k \propto I^2$, it is possible to understand why the picture of the turbulent kinetic energy is similar to Fig. 5.10 of the turbulent intensity (I). Eq. 2.53 of the turbulent intensity demonstrates that it decreases if the axial velocity u increases (Reynolds number's effect). In the region immediately after the inlet surface, as it can be seen in Fig. 5.2, the velocity increases and it generates the variation of turbulent parameters. The same link between speed and turbulent kinetic energy is evident also taking a look of the outlet profiles (Section 5.1.1). In fact, the turbulent kinetic energy (Fig. 5.18) increases close to the wall where on the contrary the velocity u (Fig. 5.15) decreases. It is important therefore to consider that the turbulent intensity I is an input parameter at the inlet boundary conditions in Ansys Fluent solver. It means that the choice of its value influences the behaviour of the turbulence in the combustor and consequently the flame length, as exposed in Section 5.2.2.

As done before for the density values, the dynamic viscosity and the thermal conductivity of the simulations results are compared to the transport properties computed in *Matlab* using the piecewise-polynomials functions in Section 4.3.1.

The specific heat capacity at constant pressure is computed using the definition of departure function contained in Section 4.3.2. So, the aim of this comparison is to understand how Eq. 4.20 implemented in Ansys Fluent is able to predict the value of thermodynamic property. For this reason, the relative errors are calculated with the results of *NIST* database simulation taken as reference solution.

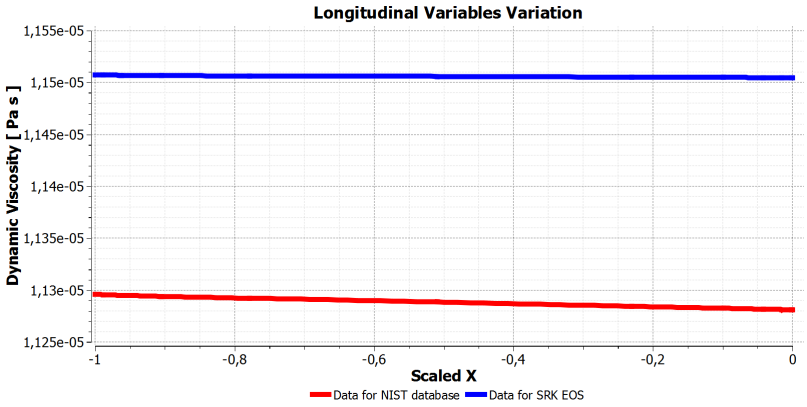

FIGURE 5.12: Methane Longitudinal Profile Dynamic Viscosity

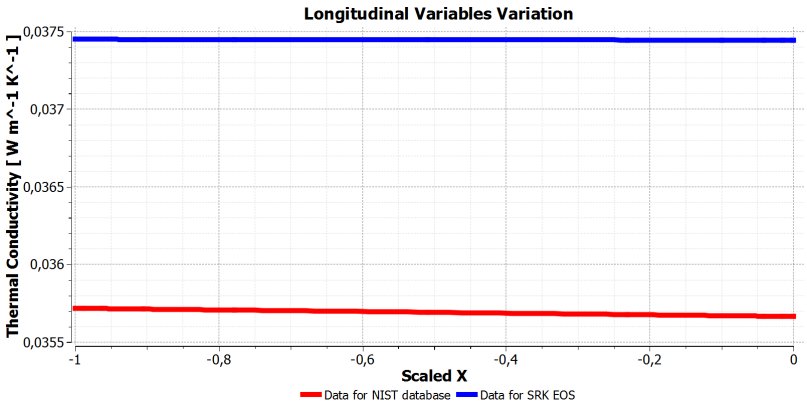

FIGURE 5.13: Methane Longitudinal Profile Thermal Conductivity

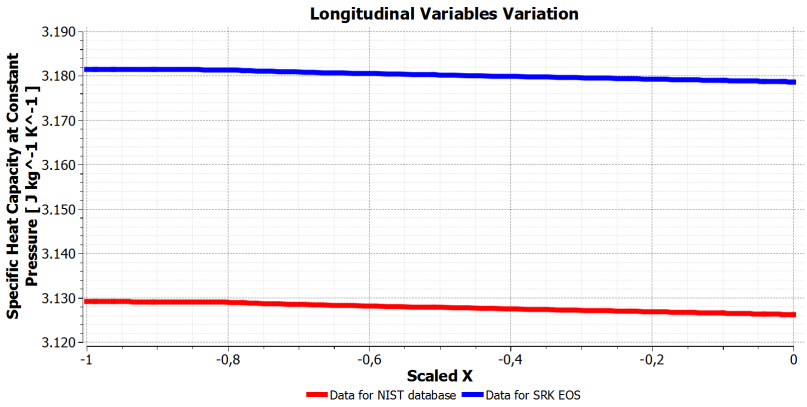

FIGURE 5.14: Methane Longitudinal Profile Specific Heat Capacity

Fig. 5.12, 5.13 and 5.14 show the evolution of the properties along the injector. Tab. 5.2, 5.3 and 5.4 show the computed values in the simulations at inlet condition as an average over the inlet surface. Moreover, relative errors are computed and the results demonstrate that the applied polynomials and departure function (already implemented in Fluent default) are reliable at inlet condition. Therefore, the same functions will be tested for the mixing and combustion simulations.

Method / Value	Viscosity $[Kg/m*s]$	Relative Error %
NIST	1.1296e-05	0.0168
Piecewise-Polynomial	1.1507e-05	0.0327

TABLE 5.2: Methane Simulated Dynamic Viscosity at inlet condition

Method / Value	Thermal Conductivity $[W/m*K]$	Relative Error %
NIST	0.0357204	0.0074
Piecewise-Polynomial	0.0374512	0.0158

TABLE 5.3: Methane Simulated Thermal Conductivity at inlet condition

Method / Value	Heat Capacity $[J/Kg*K]$	Relative Error %
NIST	3129.12	0.0061
Departure Functions	3181.48	0.0229

TABLE 5.4: Methane Simulated Heat Capacity at inlet condition

Outlet Profiles

The outlet profiles of the injectors, which are also applied as inlet boundary conditions in the combustion chamber, are the following ones:

- velocity u (x-axis) (Fig. 5.15);
- velocity v and w close to 0 everywhere in the methane injectors simulations;
- turbulent kinetic energy k (Fig. 5.18);
- turbulent dissipation rate ω (Fig. 5.19);
- static temperature T (Fig. 5.17);

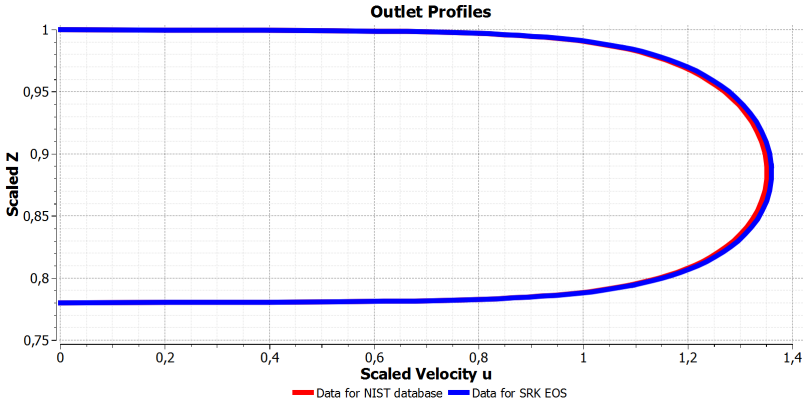

FIGURE 5.15: Methane Outlet Profile Velocity u

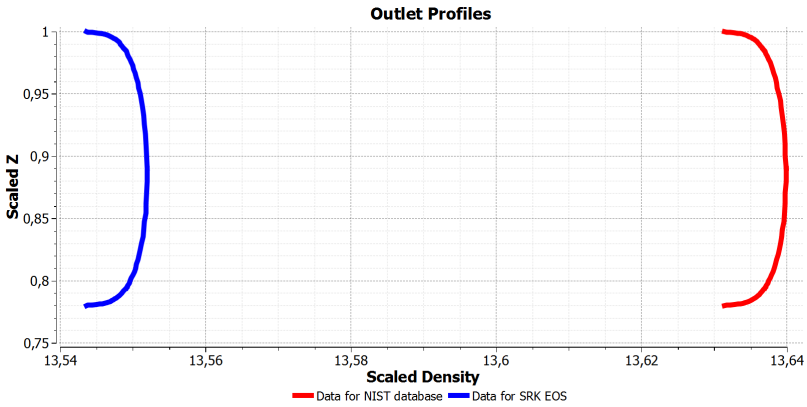

FIGURE 5.16: Methane Outlet Profile Density

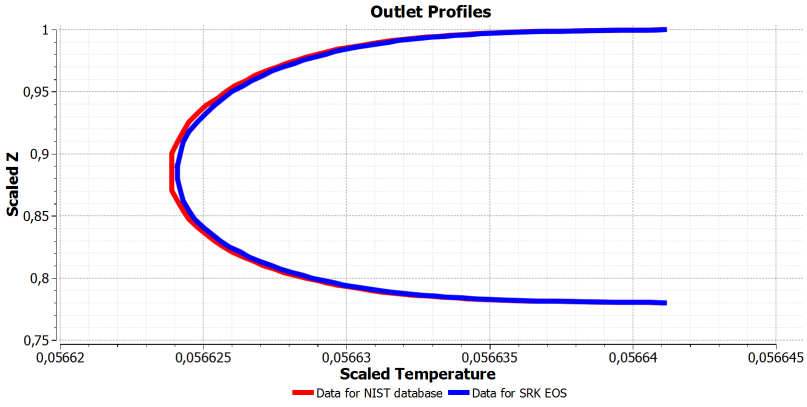

FIGURE 5.17: Methane Outlet Profile Temperature

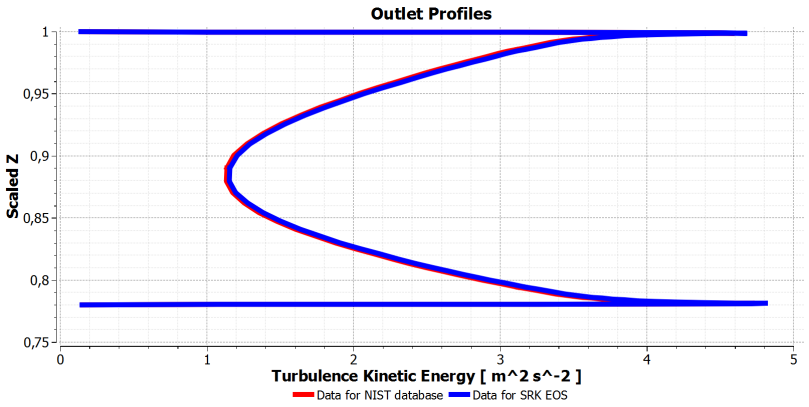

FIGURE 5.18: Methane Outlet Profile Turbulent Kinetic Energy

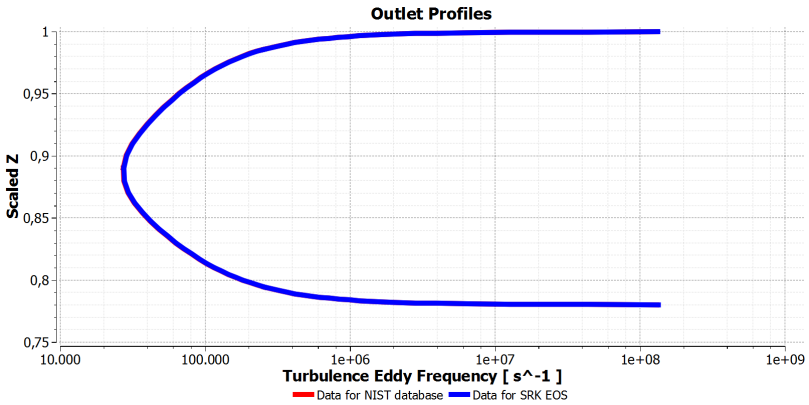

FIGURE 5.19: Methane Outlet Profile Turbulent Dissipation Rate

In particular, the velocity and the temperature outlet profiles[2], respectively in Fig. 5.15 and 5.17, are typical profiles of a flow that evolves along a pipe. The velocity profile is typical of a turbulent flow and the temperature increase close to the wall due to stress force and friction losses.

Considering the outlet profiles, the Reynolds number is computed in the middle of the methane core and the value confirms that the methane's flow in the injector is fully turbulent.

$$Re_{d_h} \approx 130000$$

In fact, for a flow in a pipe with a diameter d_{d_h}, experimental observations show that a laminar flow occurs when $Re_{d_h} < 2300$ and turbulent flow occurs when $Re_{d_h} > 2900$.

The methane injector simulations reach the convergence condition and the final residuals are shown in Tab. 5.5. At the end of each solver iteration, the residual for each of the conserved variables is computed and stored, thereby recording the convergence history, that can be seen in Fig. 5.20. The absolute convergence criterion in Ansys Fluent is applied. It requires that the globally scaled residuals, decrease to 10^{-5} for all equations except the energy equation, for which the criterion is 10^{-6} [21].

iter	continuity	u	v	w	energy	k	omega
212	9.96e-06	2.05e-10	5.66e-10	5.22e-10	1.08e-13	6.78e-10	2.48e-09

TABLE 5.5: Residuals of the Methane Injector SRK EOS 180 degrees sector simulation

[2]2D plots over the outlet surface can be found in B.1.1

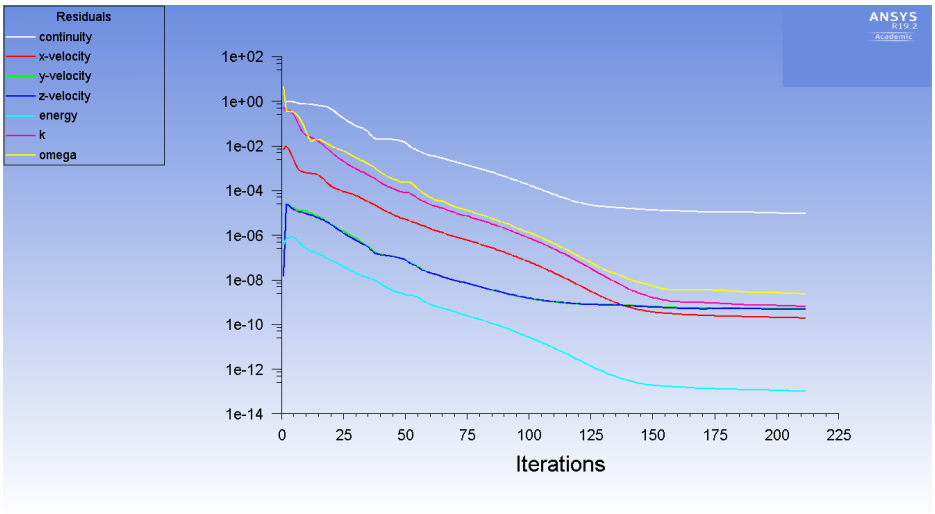

FIGURE 5.20: Convergence History of the Methane Injector SRK EOS 180 degrees sector simulation

5.1.2 Oxygen

The simulations of the oxygen injectors are presented. In particular, as done for the methane injectors, the comparison between *SRK EOS* and *NIST* database results is discussed simulating the 180 degrees sector of the oxygen injector. Fig. 5.21 shows the detection lines in the oxygen injector domain.

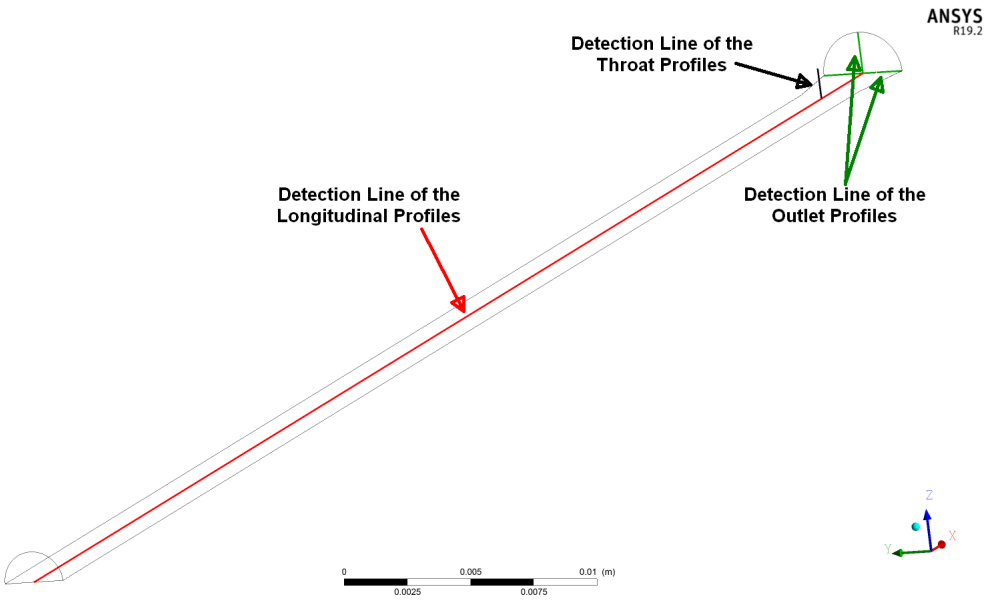

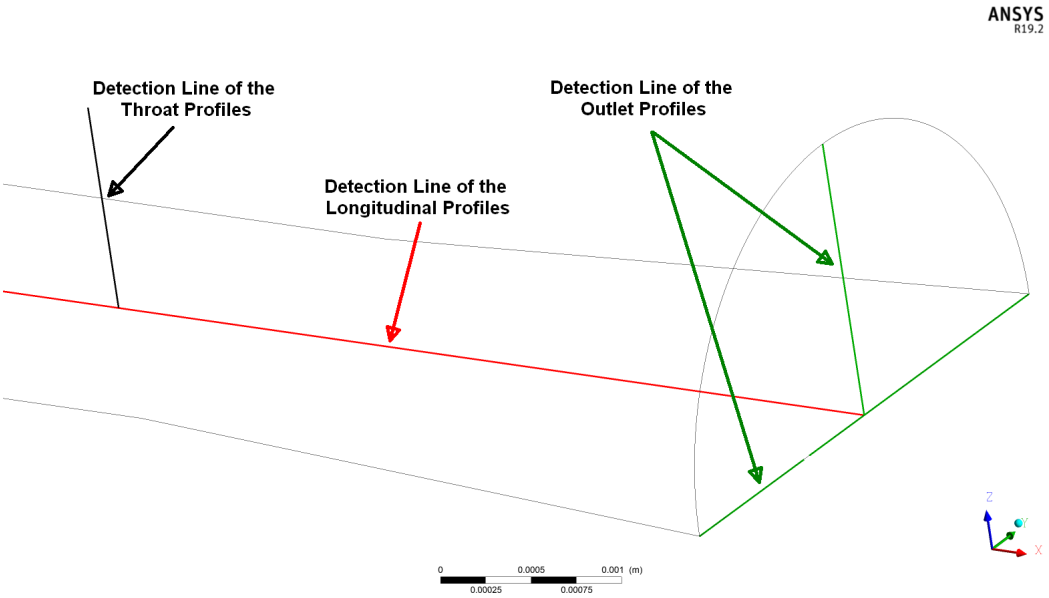

FIGURE 5.21: Detection Lines in the Oxygen Injector

As exposed in Section 3.2, the duct of oxygen is not a pipe with constant area everywhere. The most interesting part of the injector is the tapering part in which the fluid should expand and decelerate since the duct area increases.

Regarding the first part of the injector with constant area, the behaviour of fluid is explained in Section 5.1.1 with the explanation of the Fanno Flow.

Longitudinal Profiles

The behaviour of a fluid within a divergent pipe is regulated by the gas dynamic laws. For a subsonic flow ($M < 1$), a decreases in velocity in Fig. 5.22 is associated with an increases in area [18]. If the velocity decreases, the fluid tends to be more compact, to reduce its specific volume and the pressure in Fig. 5.23 consequently has to increase.

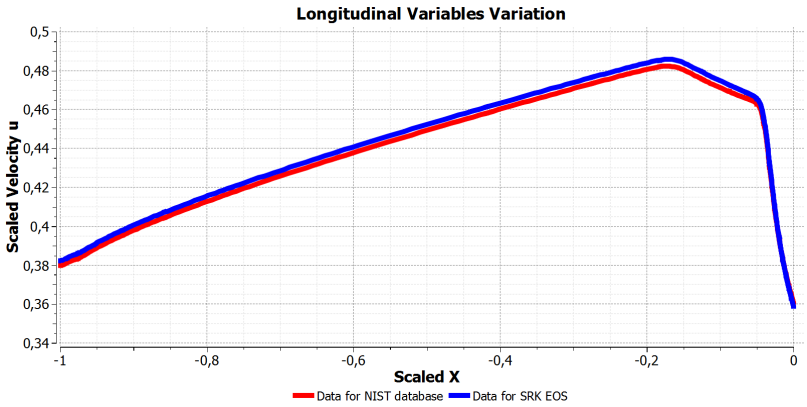

FIGURE 5.22: Oxygen Longitudinal Profile Velocity u

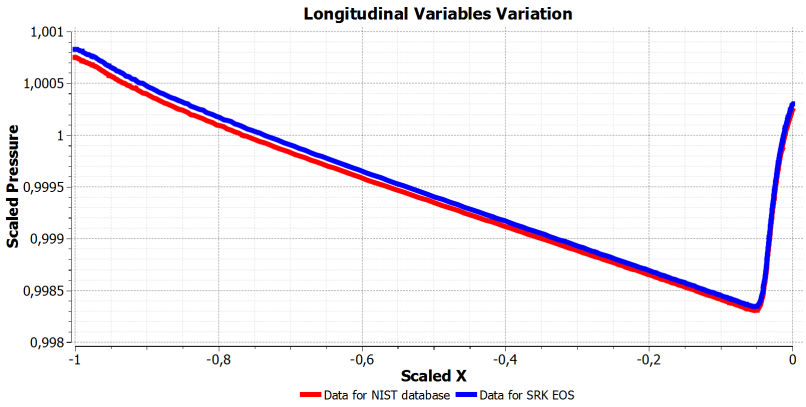

FIGURE 5.23: Oxygen Longitudinal Profile Pressure

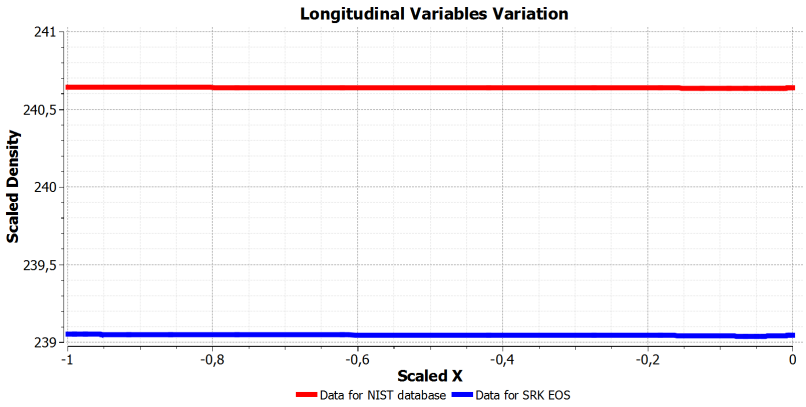

FIGURE 5.24: Oxygen Longitudinal Profile Density

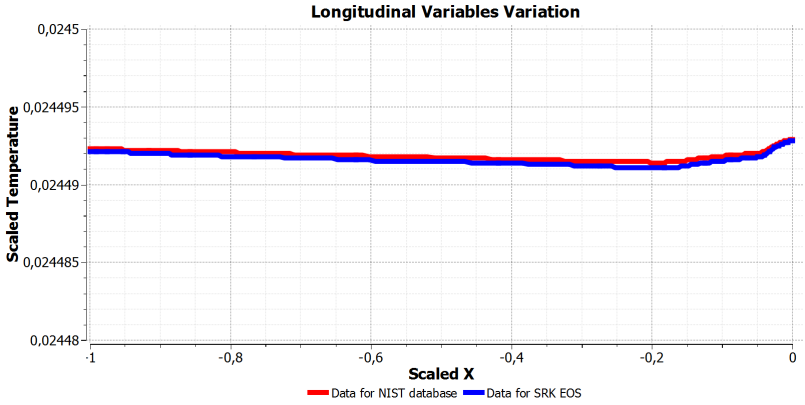

FIGURE 5.25: Oxygen Longitudinal Profile Temperature

Fig. 5.24 shows the density in the oxygen injector. If the velocity decreases, the divergence of velocity in Eq. 2.27 is negative and the density should increases. In reality, the oxygen is injected in liquid form and this phenomenon is not very noticeable for the fluid's high density. In fact, the density remains almost constant along the pipe.

Method / Value	Relative Error %
NIST	0.0062
SRK	0.0059

TABLE 5.6: Oxygen Simulated Density Error Estimation at inlet condition

As done in Section 5.1.1 for the methane injector, Tab. 5.1 shows the relative error between predicted and computed density for the oxygen injector. The relative errors are very low and

the results of simulation can be accepted. This means that *SRK EOS* is valid also to compute the oxygen density.

Moreover, as said in Section 5.1.1, the velocity change also affects the turbulent parameters. In fact, if the velocity decreases, the Reynolds number decreases too and the turbulent intensity has to increase following the Eq. 2.53. So, reminding Eq. 2.49, the turbulent kinetic energy is forced to rise in the divergent part and a high turbulent flow enters into the combustion chamber.

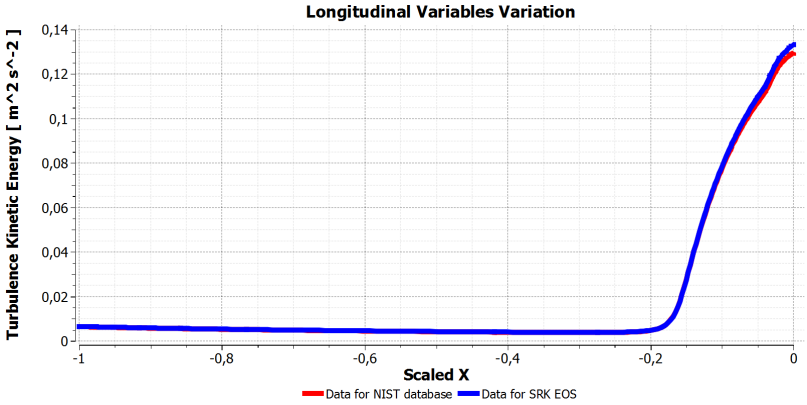

FIGURE 5.26: Oxygen Longitudinal Profile Turbulent Kinetic Energy

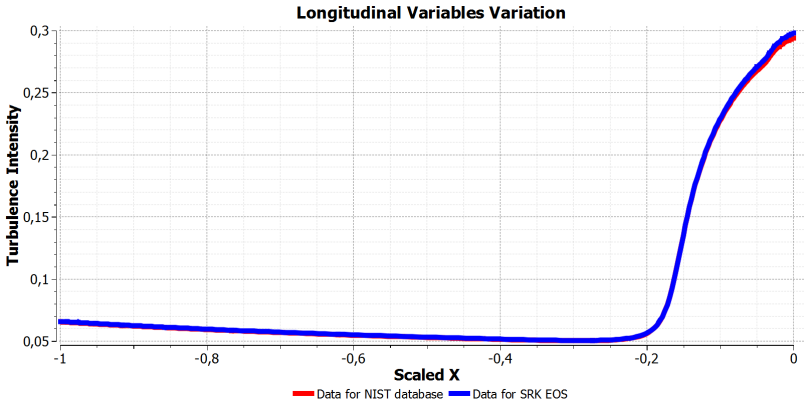

FIGURE 5.27: Oxygen Axis Turbulent Intensity

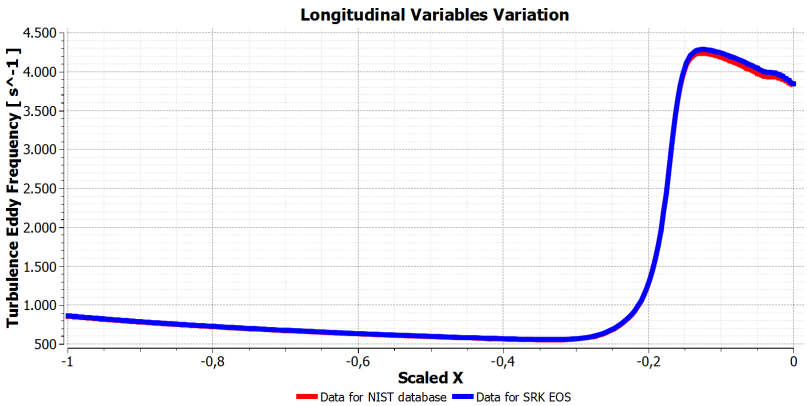

FIGURE 5.28: Oxygen Longitudinal Profile Turbulent Dissipation Rate

In Fig. 5.29 the turbulent kinetic energy is shown in the symmetry plane. It is evident how the turbulent kinetic energy starts to increase when the area starts to increase. It is interesting the behaviour that it takes in proximity of the corner. In particular, k is created by the presence of the corner and it is no longer contained within the viscous layer close to the wall in the divergent part .

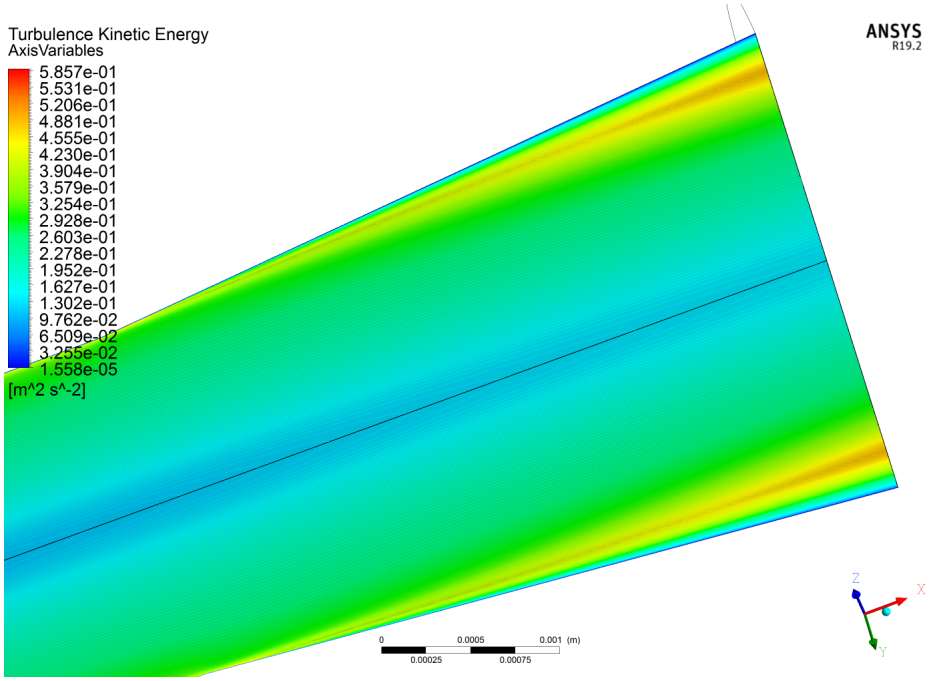

FIGURE 5.29: Oxygen Symmetry Turbulent Kinetic Energy

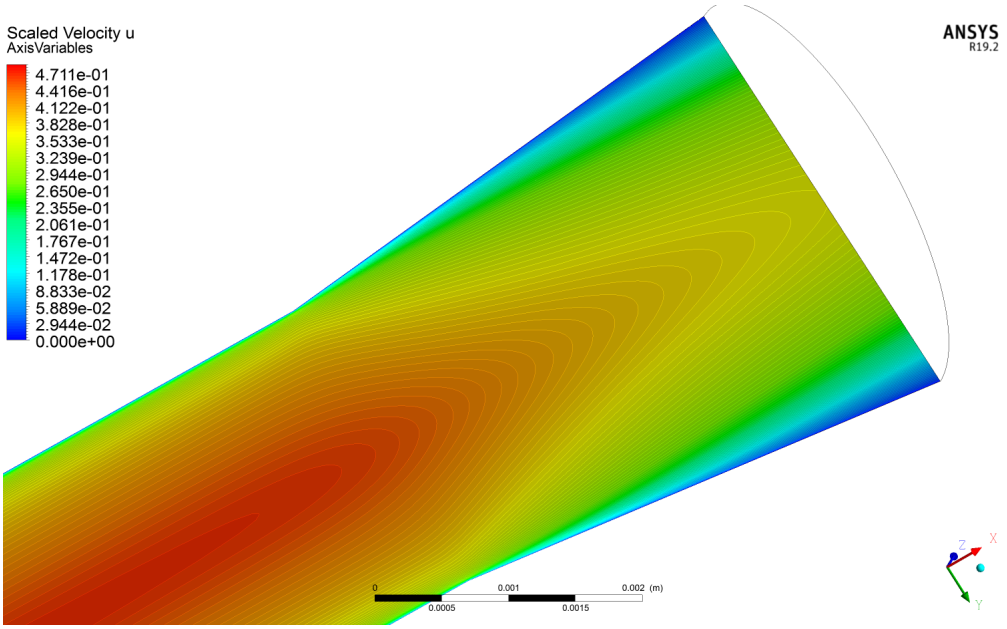

FIGURE 5.30: Oxygen Symmetry Velocity u

As it can be seen in Fig. 5.30, the thickness of the viscous layer increases in the divergent part and the maximum value of kinetic energy is located further away from the wall. In particular, the turbulent kinetic energy is maximal where the velocity w (z-axis) is also maximal, as it can be seen in Fig. 5.36 and 5.39.

Fig. 5.31, 5.32 and 5.33 show the evolution of transport and thermodynamic properties across the injector. Tab. 5.7, 5.8 and 5.9 show the computed values in the simulations at inlet condition doing an average over the inlet surface. Moreover, relative errors are computed and the results demonstrate that the applied polynomials and departure function (already implemented in Fluent default) are reliable for the specific test conditions. The same functions will be used for the mixing and combustion simulations.

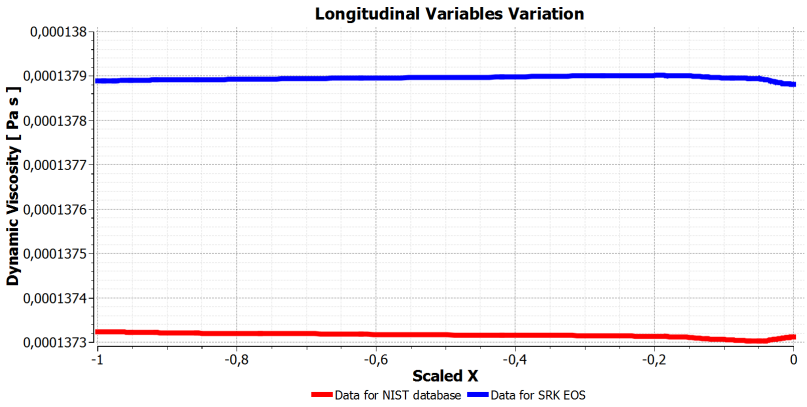

FIGURE 5.31: Oxygen Longitudinal Profile Dynamic Viscosity

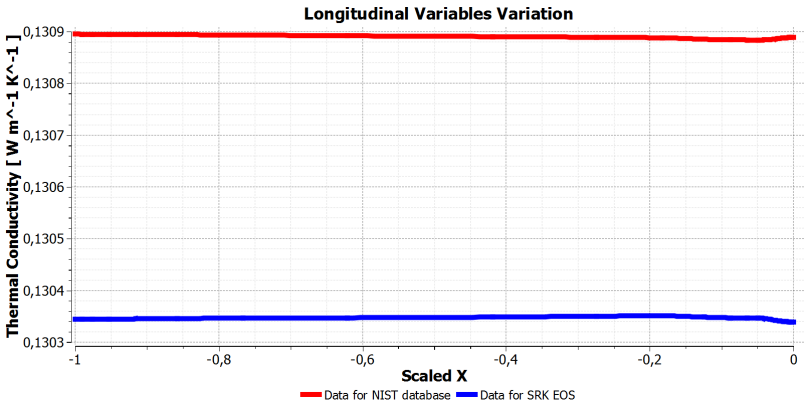

FIGURE 5.32: Oxygen Longitudinal Profile Thermal Conductivity

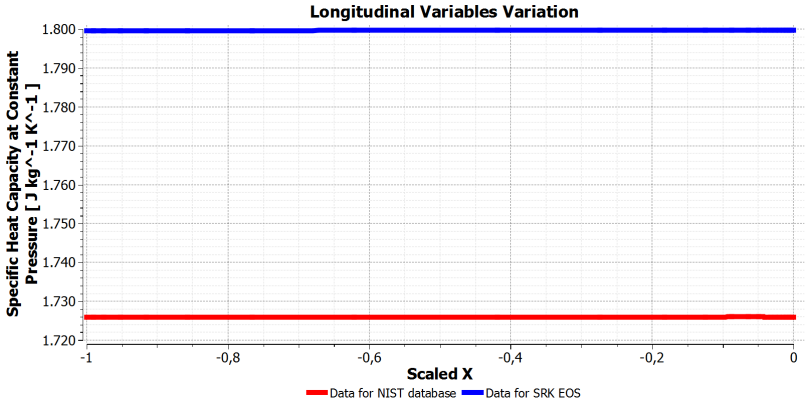

FIGURE 5.33: Oxygen Longitudinal Profile Specific Heat Capacity

Method / Value	Viscosity $[Kg/m*s]$	Relative Error %
NIST	1.3729e-04	0.026
Piecewise-Polynomial	1.3786e-04	0.0036

TABLE 5.7: Oxygen Simulated Dynamic Viscosity at inlet condition

Method / Value	Thermal Conductivity $[W/m*K]$	Relative Error %
NIST	1.3088e-01	0.0065
Piecewise-Polynomial	1.3033e-01	0.0001

TABLE 5.8: Oxygen Simulated Thermal Conductivity at inlet condition

Method / Value	Heat Capacity $[J/Kg*K]$	Relative Error %
NIST	1725.91	0.0036
Departure Functions	1799.69	0.0390

TABLE 5.9: Oxygen Simulated Heat Capacity at inlet condition

Outlet Profiles

The following outlet profiles[3] are extracted from the results of the injector simulation and then they are imported and interpolated as inlet boundary conditions for the combustion chamber simulations.

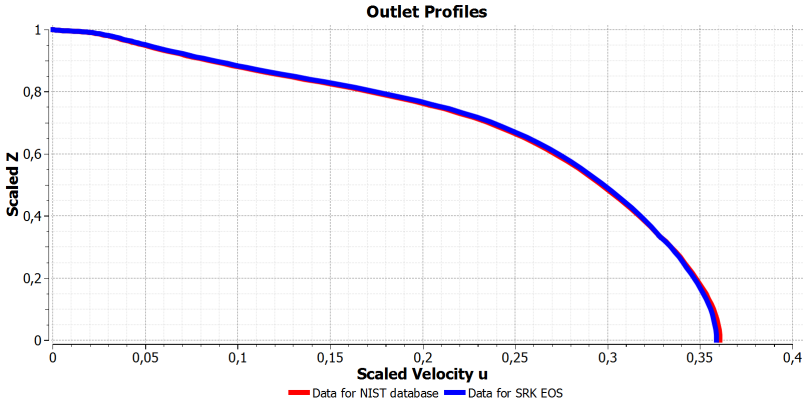

FIGURE 5.34: Oxygen Outlet Profile Velocity u

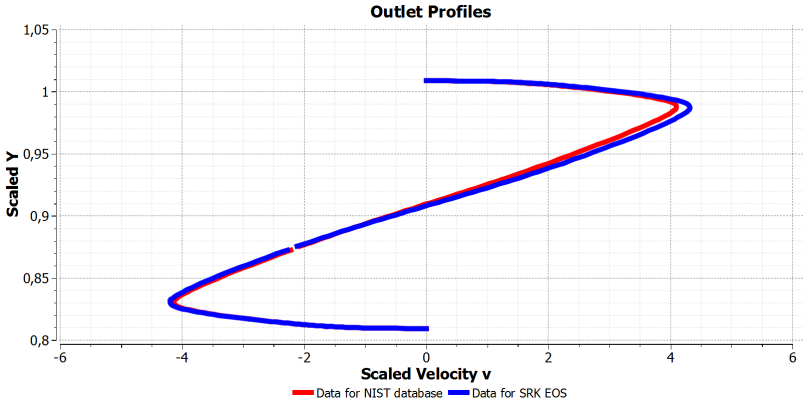

FIGURE 5.35: Oxygen Outlet Profile Velocity v

[3] 2D plots of the outlet surface can be found in B.1.1

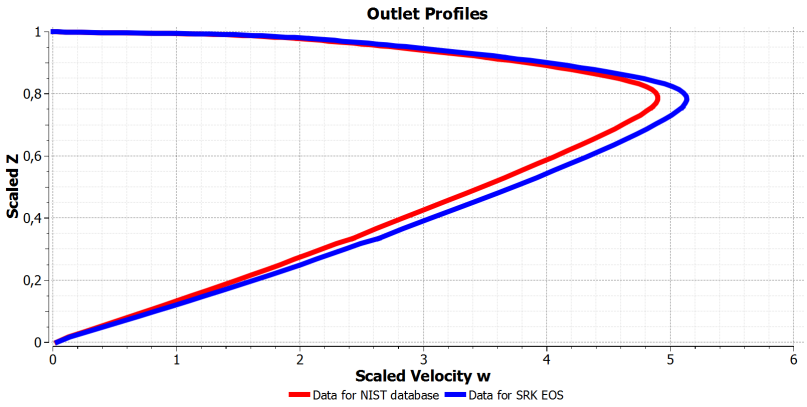

FIGURE 5.36: Oxygen Outlet Profile Velocity w

Fig. 5.34, 5.35 and 5.36 show the three components of the velocity profile on the outlet surface. The flow expands in the tapering part being attached to the upper wall. This is confirmed taking a look of the direction velocity vector plot (Fig. 5.37).

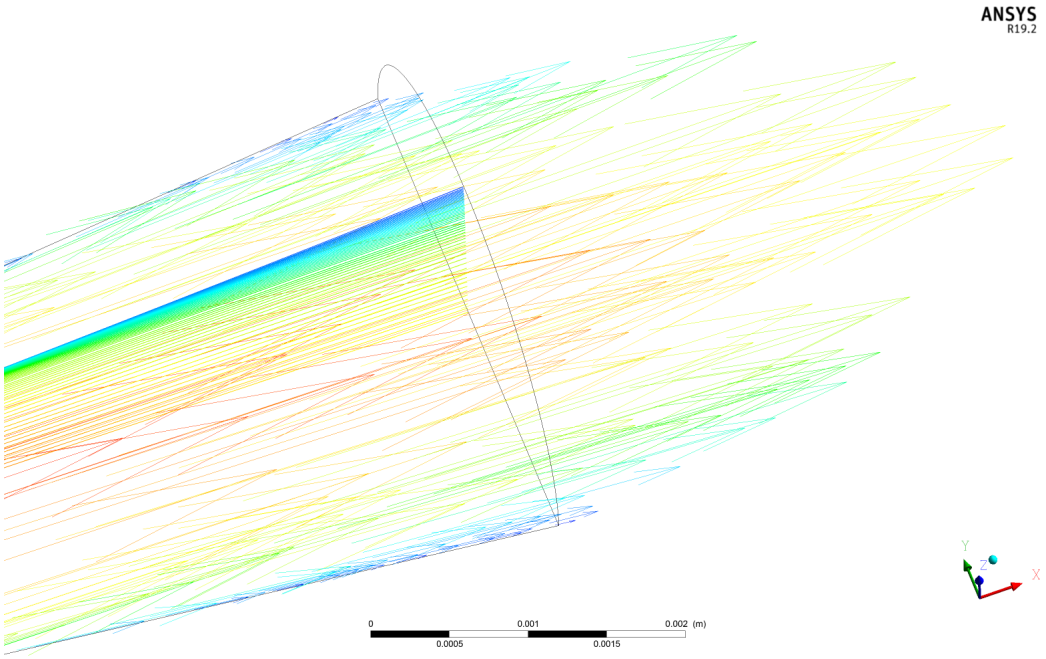

FIGURE 5.37: Oxygen Injector Vector Velocity

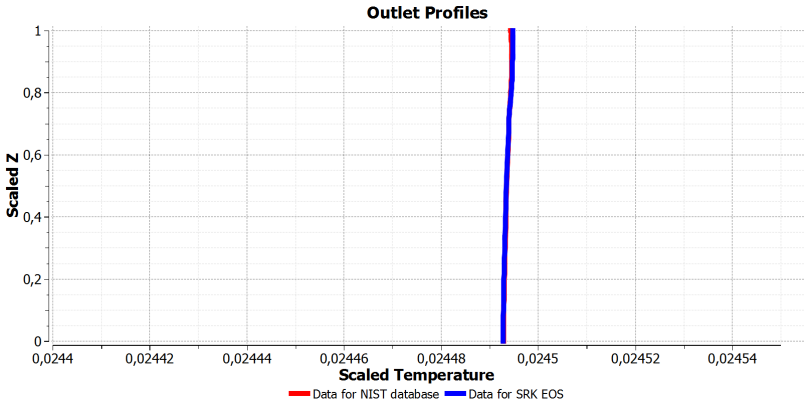

FIGURE 5.38: Oxygen Outlet Profile Temperature

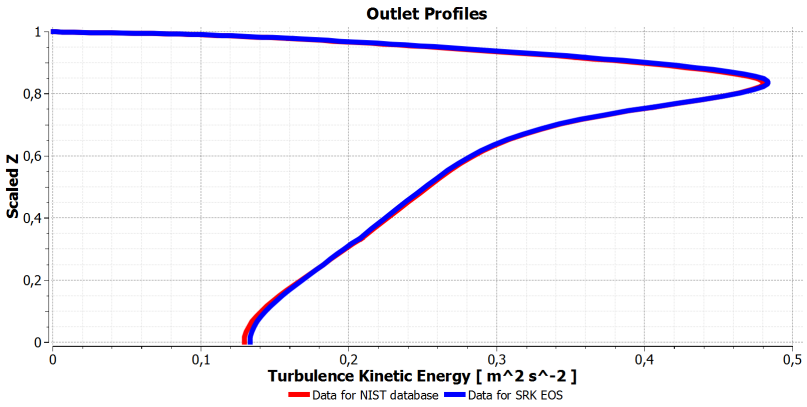

FIGURE 5.39: Oxygen Outlet Profile Turbulent Kinetic Energy

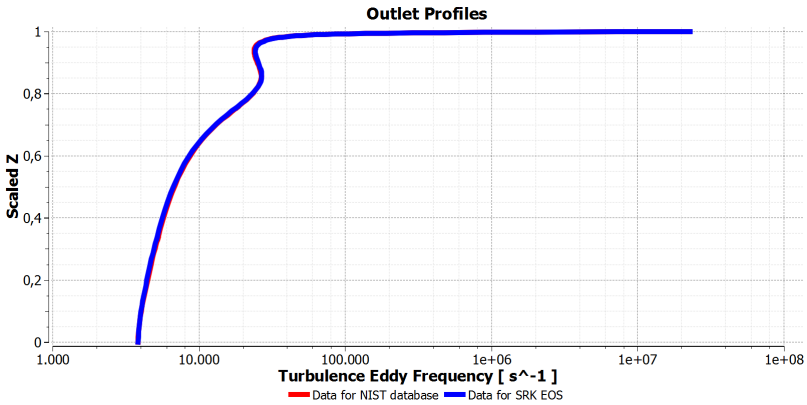

FIGURE 5.40: Oxygen Outlet Profile Turbulent Dissipation Rate

Considering the outlet profiles, the Reynolds number is computed in the middle of the oxygen core and the value confirms that the oxygen's flow in the injector is fully turbulent.

$$Re_{d_h} \approx 152000$$

The velocity profile in Fig. 5.34 is determined by the tapering part. The area increases, the velocity u decreases and the viscous layer close to the wall raises its thickness (Fig. 5.30). As it can be seen in Fig. 5.41, the profile of the velocity u in correspondence to the "throat" (where the area starts to increase) looks more like a typical turbulent velocity profile.

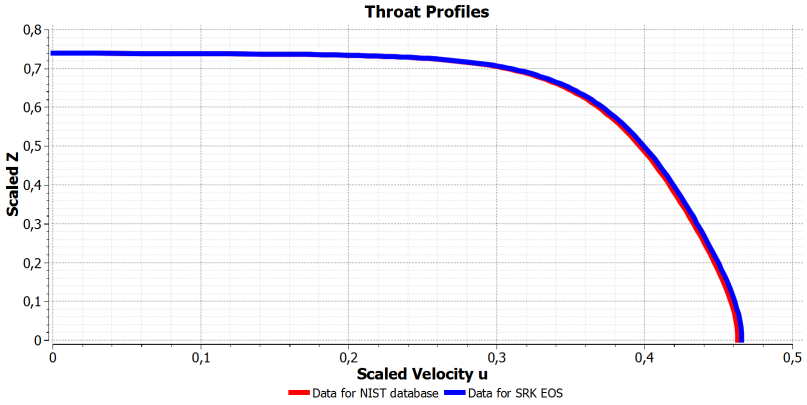

FIGURE 5.41: Oxygen Throat Profile Velocity u

The oxygen injector simulations reach the convergence condition and the final residuals are shown in Tab. 5.10. The convergence history is shown in Fig. 5.42.

iter	continuity	u	v	w	energy	k	omega
336	8.29e-06	3.54e-06	3.35e-08	1.65e-08	1.74e-09	1.69e-06	4.72e-06

TABLE 5.10: Residuals of the Oxygen Injector SRK EOS 180 degrees sector simulation

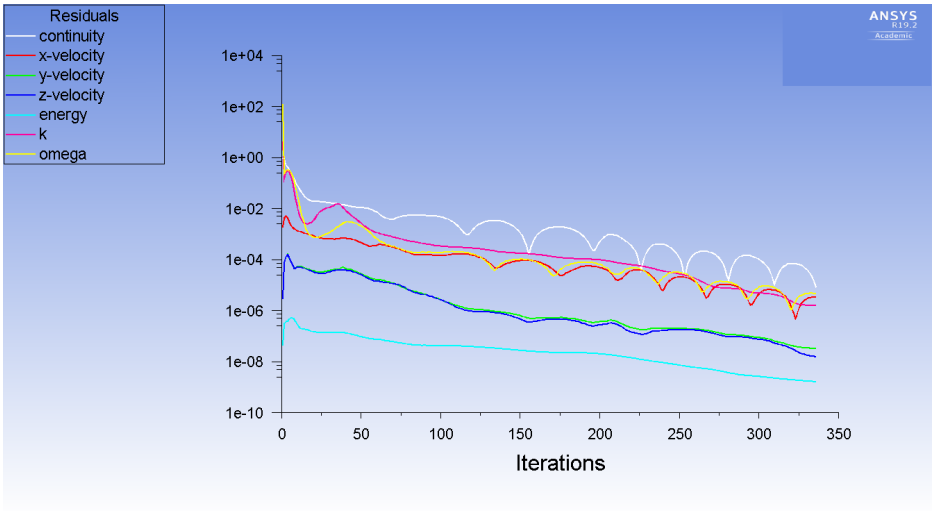

FIGURE 5.42: Convergence History of the Oxygen Injector SRK EOS 180 degrees sector simulation

5.2 Combustion Chamber

The results detailed in Section 5.1 are used as inlet condition for the combustion simulations. Many simulations of the combustion chamber have been conducted and many studies are presented in the current section.

Firstly, the simulation of the mixing case are used to conduct a mesh "validation". The mesh has to fulfil some requirements to get reliable results. In particular, the residuals of the simulations are affected by the characteristics of mesh. In this phase, a "sort of" mesh convergence study was conducted, just to analyse the main issues of the mesh and trying solving them.

In a second step, the combustion was activated. The first studies on combustion were performed using Ideal Gas EOS to compute the density of the mixture. Ideal Gas EOS is the simplest one and it simplifies the numerical convergence of the used method. It is fully validated in Asys Fluent and the results will confirm that this method works very well. This phase is used to understand how the *EDM* combustion model works in Ansys Fluent and how some parameters of the method could influence the solution.

Finally, the real gas computation with *SRK EOS* and piecewise-polynomials functions was tested. Many issues occurred during the simulation, as for example the mistake in the mixture density computation explained in Section 4.4. Due to big difficulties to get a stable flame, a 2D test case was build in order to reduce the computational cost and time. It was possible to make many tests and something interesting has come out.

Fig. 5.43 shows the detection lines in the combustion chamber. The data of the illustrated profiles are extrapolated from these lines.

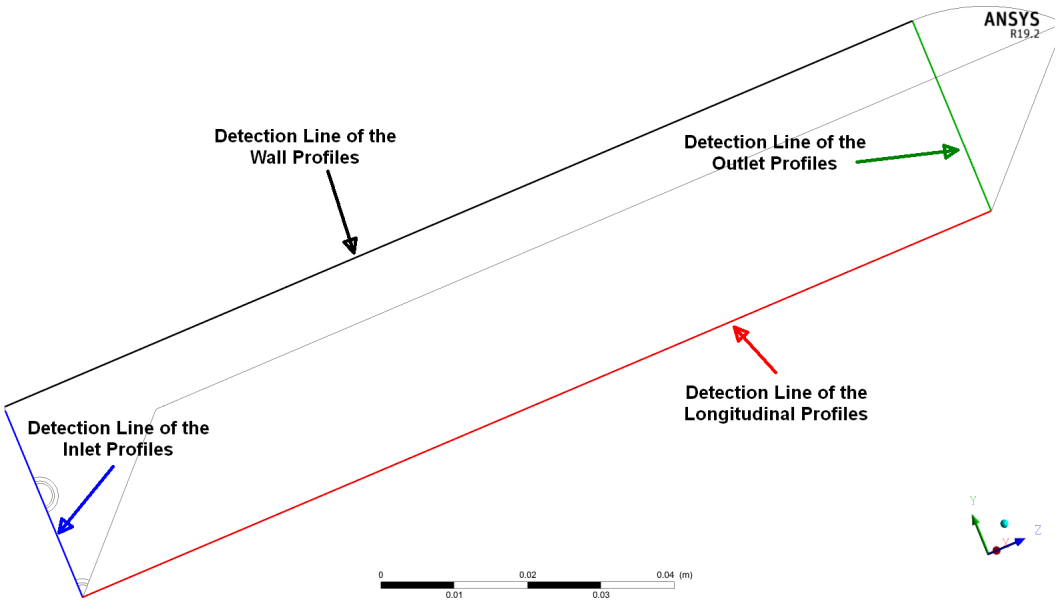

FIGURE 5.43: Detection Lines in the Combustion Chamber

5.2.1 Mixing

The first study conducted in the combustor is the simulation of the mixing case. In particular, the results of the Mixing simulations are compared as well as possible to the results obtained following the theory of the diffusion flame explained in Section 2.4.

The analysis of the mesh was conducted until the simulations reached the convergence criteria. The final residuals are shown in Tab. 5.11. At the end of each solver iteration, the residual for each of the conserved variables is computed and stored, thereby recording the convergence history, as can be seen in Fig. 5.44. The absolute convergence criterion in Ansys Fluent is applied. It requires that the globally scaled residuals, decrease to 10^{-3} for all equations except the energy and species equations, for which the criterion is 10^{-6} [21]. It is important to highlighted that to obtain a good convergence, pseudo-transient method with very large time-step (10^{-2}) has been utilized for all the equations. In fact, if the time-step increases the oxygen core's length in the combustor decreases and everything mix very fast. With small time-step, it is possible to obtain a full homogenous mixture very close to the injector post tip.

iter	404
continuity	9.57e-04
u	2.06e-06
v	3.32e-07
w	2.86e-07
energy	2.49e-07
k	5.68e-06
omega	5.66e-04
ch4	2.12e-07
o2	6.46e-08

TABLE 5.11: Residuals of the Mixing simulation

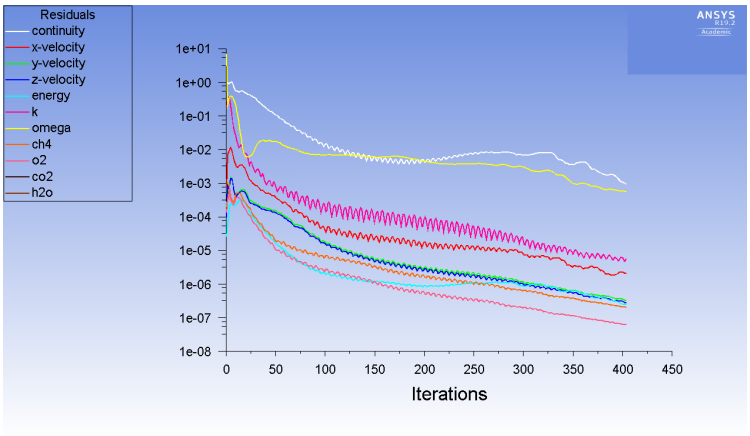

FIGURE 5.44: Convergence History of the Mixing simulation

Inlet Profiles

The following plots are taken in correspondence of the detection line in the inlet surface. It is possible to see the matching between the inlet profile in the chamber and the outlet profile of the methane and oxygen injectors, described in Section 5.1.1 and 5.1.2. This demonstrates that the coupling of the simulations is well-done and the work can proceed correctly studying the combustor.

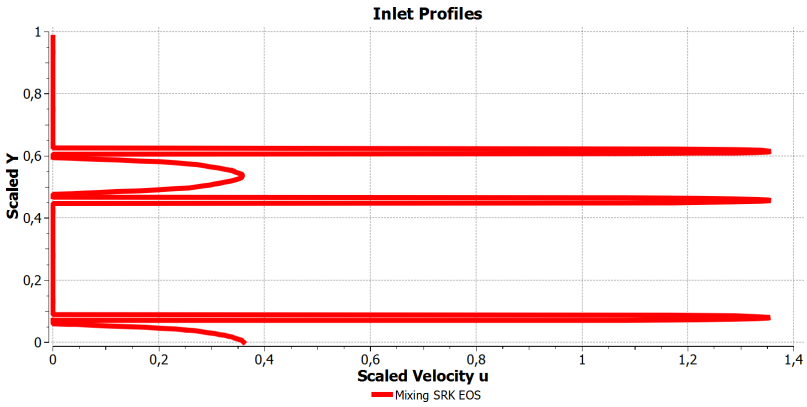

FIGURE 5.45: Mixing Inlet Profile Velocity u

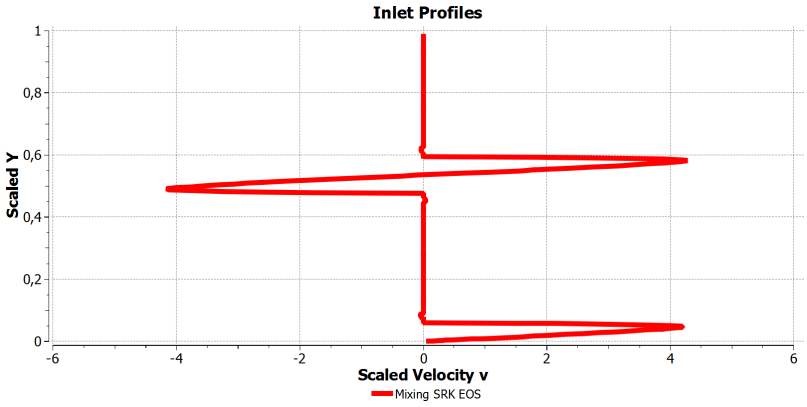

FIGURE 5.46: Mixing Inlet Profile Velocity v

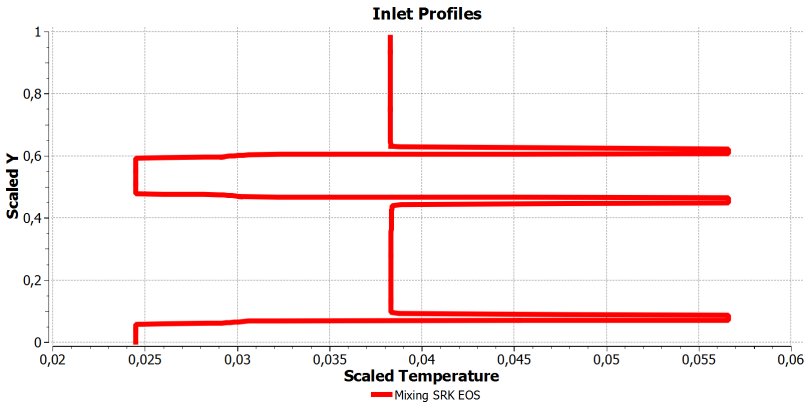

FIGURE 5.47: Mixing Inlet Profile Temperature

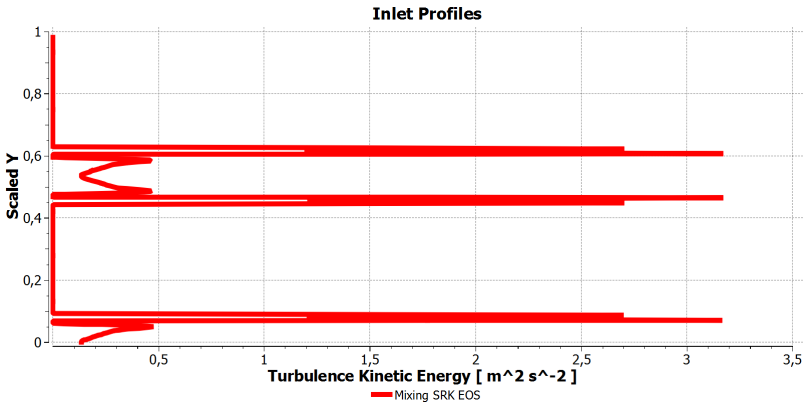

FIGURE 5.48: Mixing Inlet Profile Turbulent Kinetic Energy

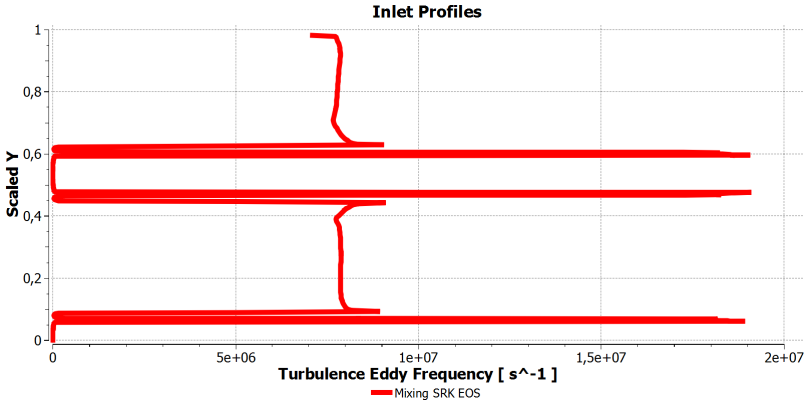

FIGURE 5.49: Mixing Inlet Profile Turbulent Dissipation Rate

Symmetry Surfaces Plots

In order to visualize the behaviour of the fluids within the combustion chamber, 3D plots are presented.

Fig. 5.50 and 5.51 show the mass fraction of the reactants, the only two species involved in the simulation of the mixing case.

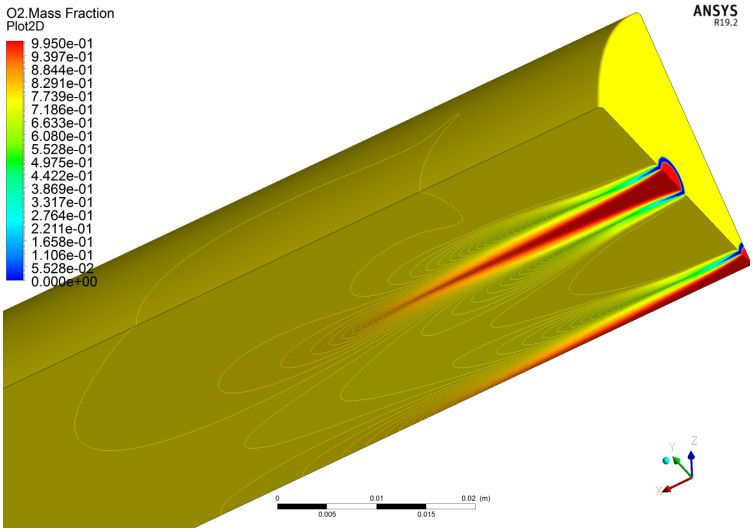

FIGURE 5.50: Mixing 3D Oxygen Mass Fraction

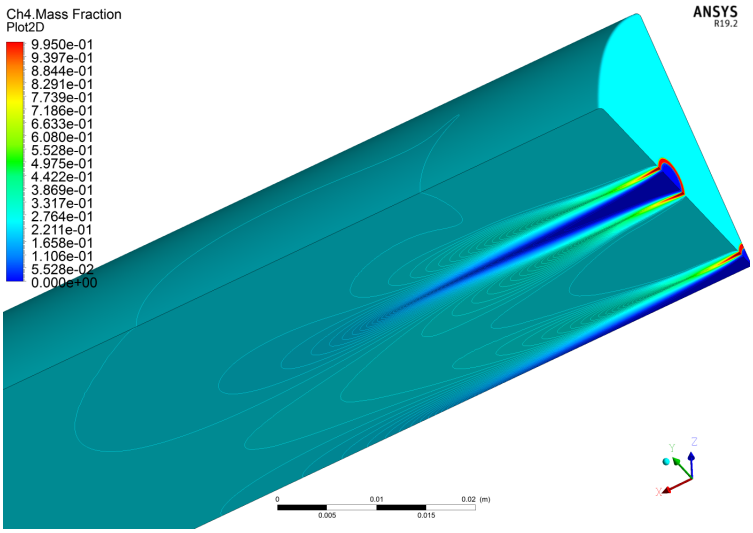

FIGURE 5.51: Mixing 3D Methane Mass Fraction

As it can be seen graphically form the previous figures, the total mixture fraction z_{TOT} is everywhere equal to unity within the chamber and this is confirmed by theory in Section 2.4.2. As it is illustrated in the previous figures, it can be computed that the fully mixture is obtained after about 20% of the combustion chamber.

The velocity field is shown in the following figures and some considerations will be done.

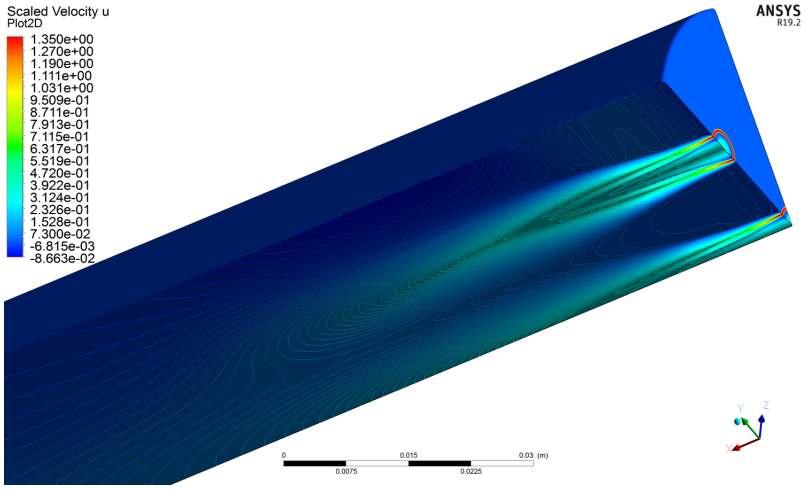

FIGURE 5.52: Mixing 3D Velocity u

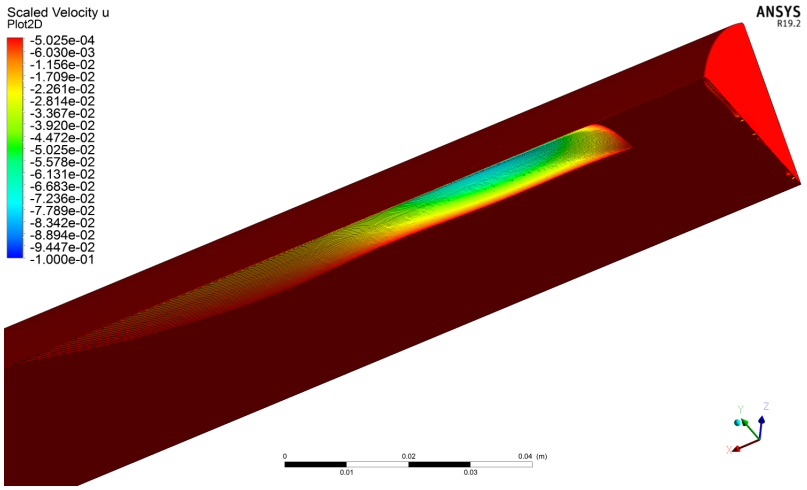

FIGURE 5.53: Mixing 3D Negative Velocity u

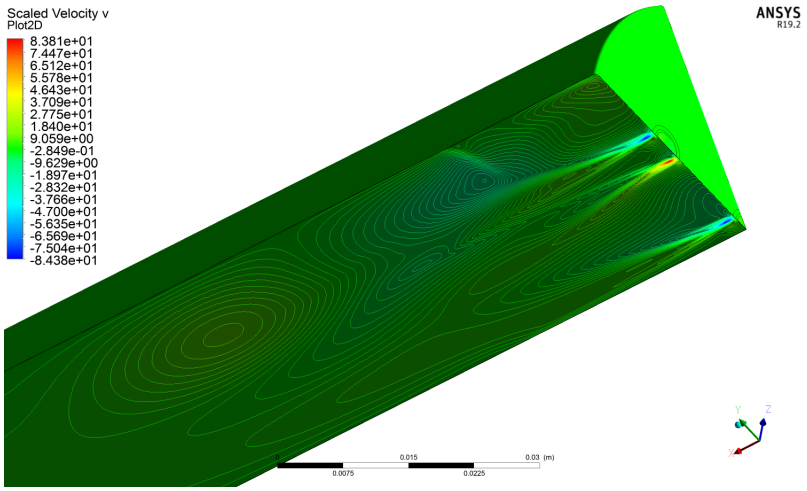

FIGURE 5.54: Mixing 3D Velocity v

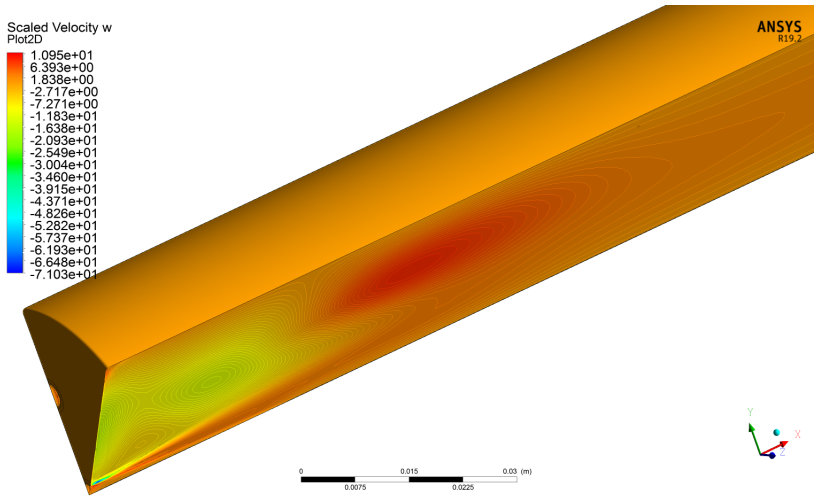

FIGURE 5.55: Mixing 3D Velocity w

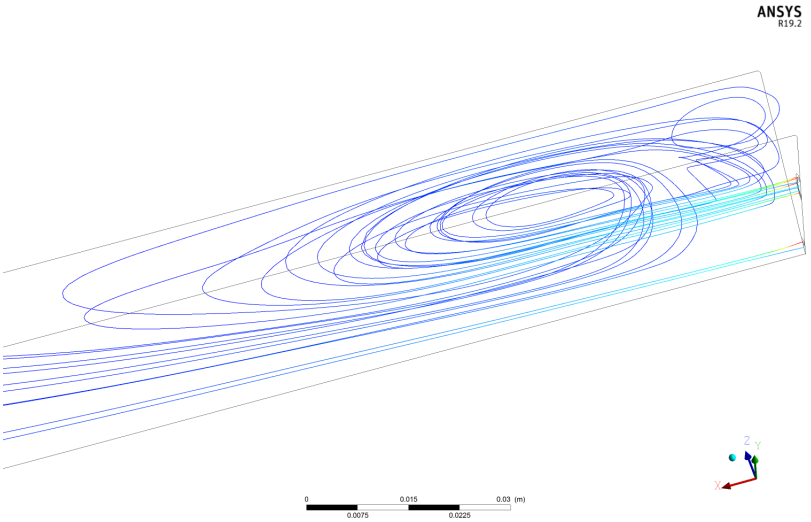

FIGURE 5.56: Mixing 3D Streamline

Fig. 5.56 shows the stream lines of the velocity that start from the inlet surfaces. The recirculation zone between the wall and the injector is very evident. In particular, as it can be seen in Fig. 5.53, the u-velocity (x-axis) is negative in a circumscribed region near the upper wall. Moreover, the change of flow direction in the same region is visible in the plots regarding the others components of velocity.

Fig. 5.54 shows the v-velocity (y-axis). Reminding the v-velocity profile in correspondence to the oxygen injector outlet surface (Fig. 5.35, B.11 and 5.46) one can note that the direction of the v-velocity immediately after the injector post is opposite. The methane diffuses very fast into the oxygen core due to high stress force between the two inlet streams. The inlet streams (oxygen and methane) have a big gap in density and speed and this fact helps the viscous stress between them and generate a really fast mixing.

Moreover, the condition of a non-slip wall is applied at the injector post tip (wall between oxygen and methane inlet). This forces the fluid to follow the wall (parallel to the wall). It creates the conditions to have a very fast mixing in this specific region between the two jets.

As it can be seen in Fig 5.57, the Mach Number inside the chamber is very low and this allows to neglect the compressibility effect within the simulations.

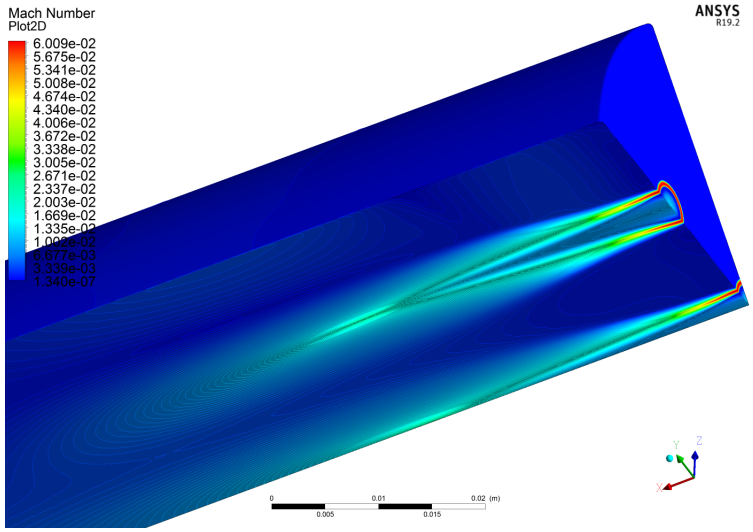

FIGURE 5.57: Mixing 3D Mach Number

Fig. 5.58 and 5.59 show the density and the temperature field in the combustion chamber.

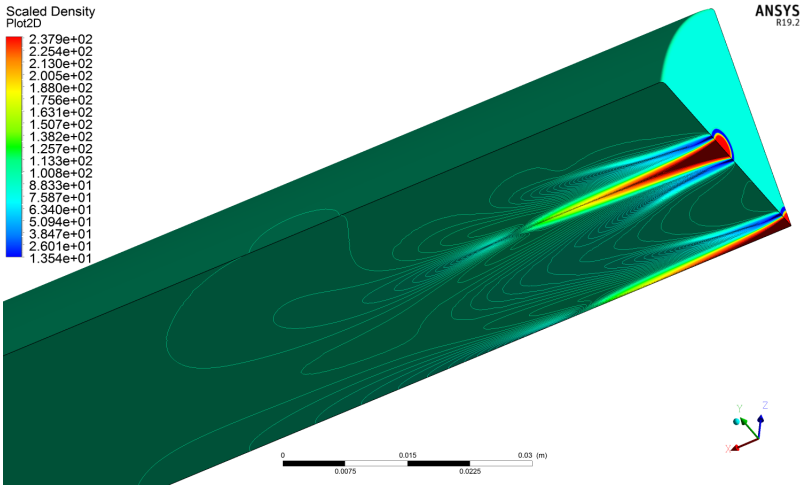

FIGURE 5.58: Mixing 3D Density

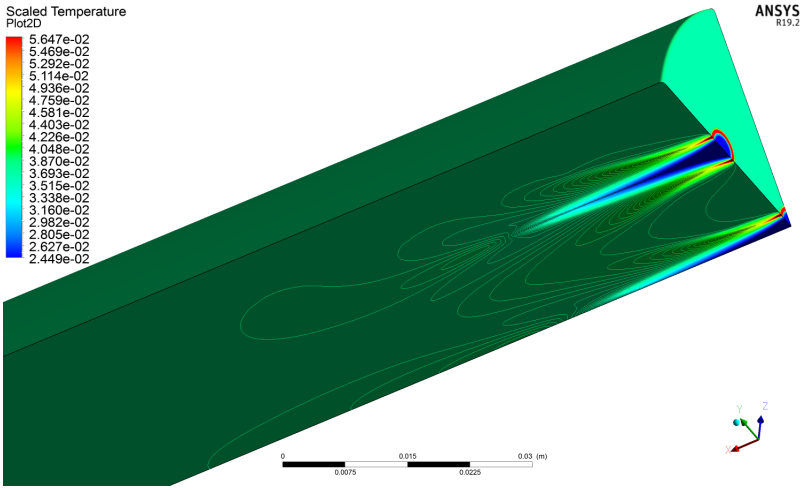

FIGURE 5.59: Mixing 3D Temperature

The results confirm the conclusion done in the injectors sections: *SRK EOS* work well for the current case if a non-reacting flow is under analysis. Unfortunately, as it will be discussed in Section 5.2.2, this conclusion is not valid if the *EDM* combustion model is activated.

The turbulent parameters are plotted in the following figures: turbulent kinetic energy in Fig. 5.60 and turbulent intensity in 5.61. As expected, huge turbulence is present immediately after the injector post where the streams start to mix and there are the peaks, negative and positive, of the v-velocity. The turbulent dissipation rate is bigger instead close to the wall, where the turbulence is dissipated how is predicted by the theory of the viscous laminar sublayer (Section 3.2.1).

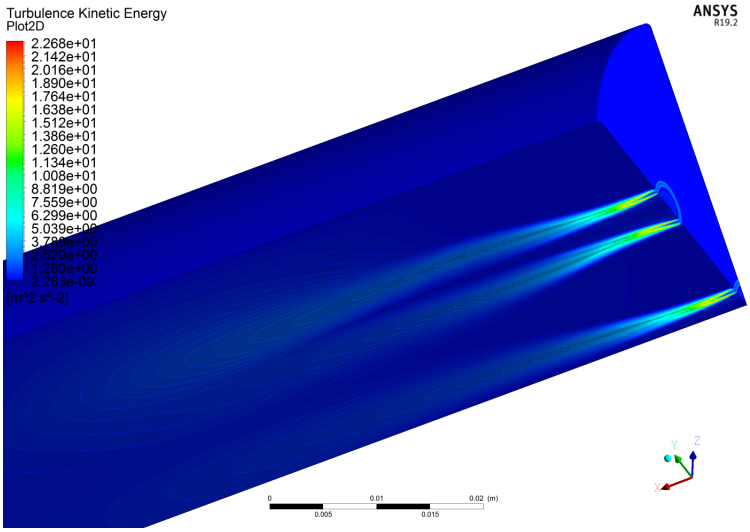

FIGURE 5.60: Mixing 3D Turbulent Kinetic Energy

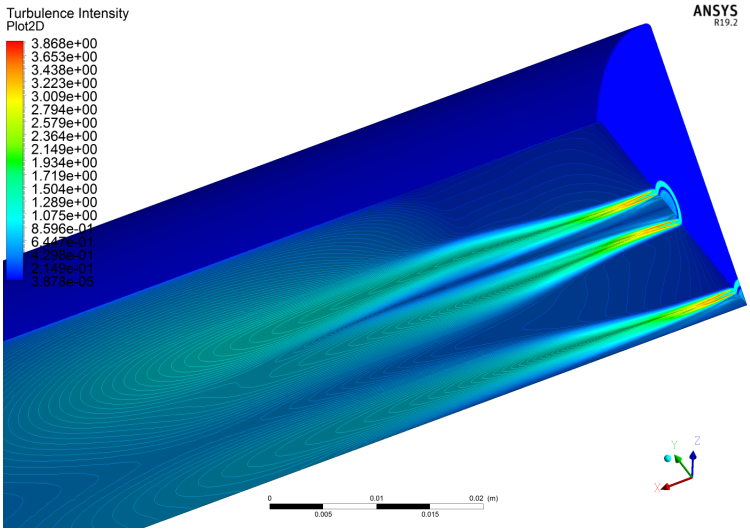

FIGURE 5.61: Mixing 3D Turbulent Intensity

The following figures show the values of the transport and thermodynamic properties in the combustor.

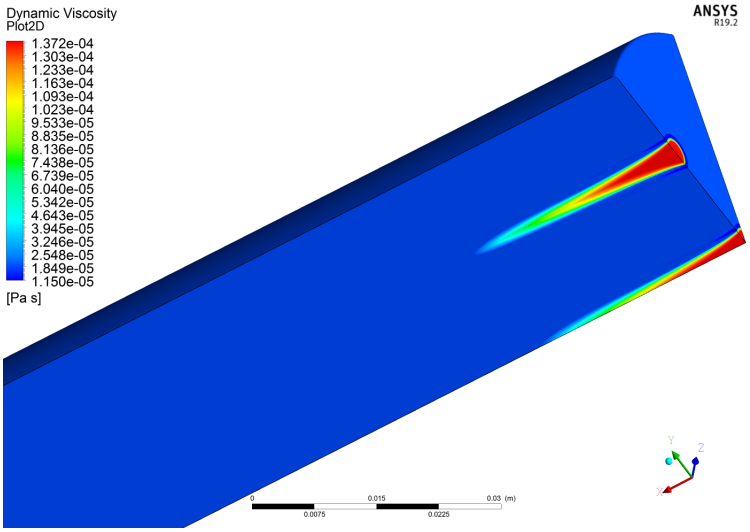

FIGURE 5.62: Mixing 3D Dynamic Viscosity

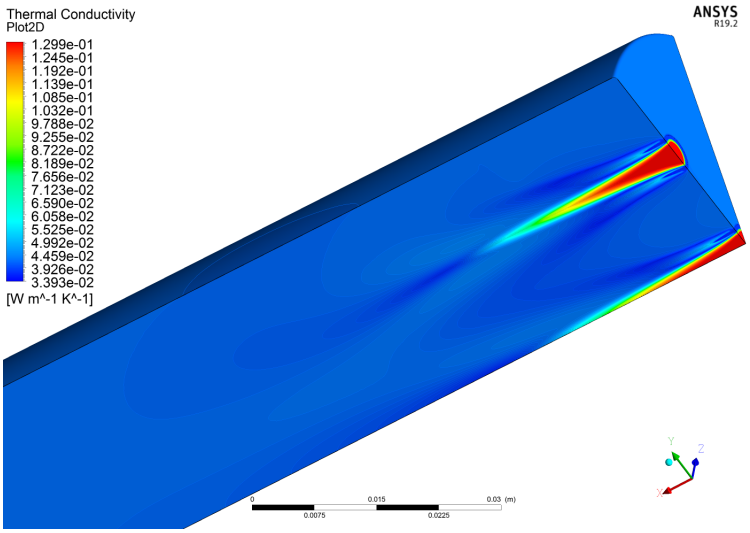

FIGURE 5.63: Mixing 3D Thermal Conductivity

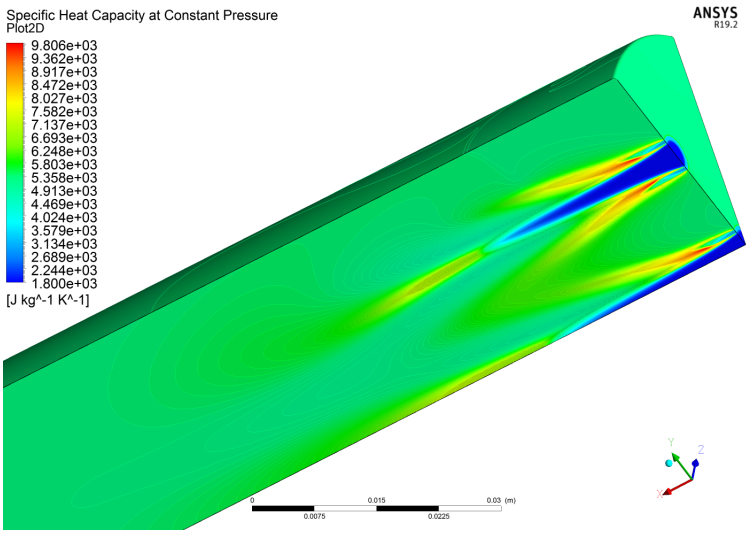

FIGURE 5.64: Mixing 3D Specific Heat Capacity

Reminding the plots in Section 4.3 regarding the analysis of these variables at constant chamber pressure, it is possible an evident comparison. This means that the piecewise-polynomials and the departure functions work well not only at inlet condition (as demonstrated in Section 5.1), but also in the mixing case. Therefore, the implemented piecewise-polynomials functions will be employed in the combustion simulations.

Outlet Profiles

The attention is given to the values of the exit variables. From the previous 3D plots is not immediate to understand what kind of flow in going out from the combustor. For this reason, the outlet profiles of some variables are presented in the current Section.

A fully mixture go out from the combustion chamber and a direct *ROF* comparison is done with the inlet *ROF* (computed knowing the inlet mass flow). The relative error is lower than 1% and it is acceptable taking into account that RANS method (Section 3.1.1) is employed to solve the governing equations.

The outlet profile of the velocity u (x-axis) is illustrated in Fig. 5.65. The velocity profile confirms that the flow in the combustor is full turbulent (high value of the Reynold number).

$$Re_{d_h} \approx 30000$$

The mesh in particular is able to evaluate the value of the velocity close to the wall. This means that the cited refinement of the hexahedral mesh close to the wall is well-done, as it will be confirmed looking into the y^+ values (Fig. 5.69).

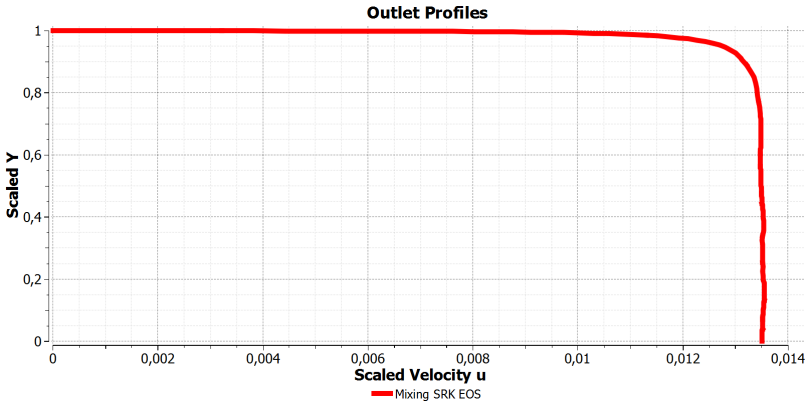

FIGURE 5.65: Mixing Outlet Profile Velocity u

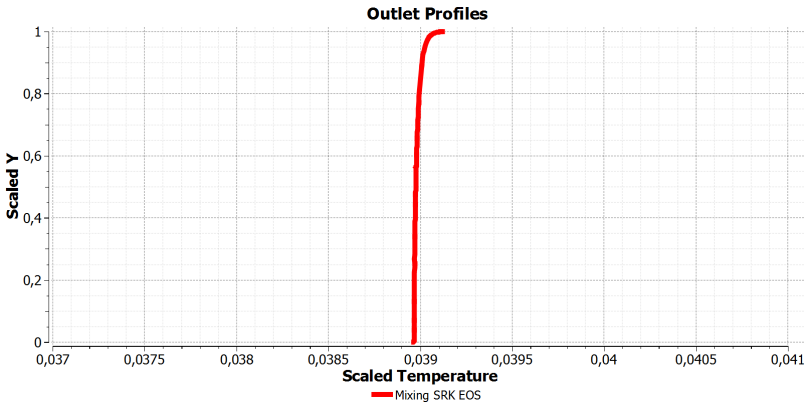

FIGURE 5.66: Mixing Outlet Profile Temperature

Fig. 5.66 shows the temperature at outlet condition. The temperature of the mixing case was predicted in Eq. 2.63 when the diffusion flame theory was explained. The simulation of the mixing is successfully verified also because this equation is fulfilled in the results. Moreover,

the temperature correctly increases close the wall due to the presence of viscous stress and friction losses.

Wall Profiles

In order to validate the mesh refinement near the upper wall of the combustor, the y^+ is illustrated in Fig.5.69. y^+ was defined in Eq. 3.13 and for the purpose of the current work was suggested to get $y^+ < 5$ *to* 5 at the wall. This requirement is fulfilled and the Shear Force (Fig. 5.67) is computed correctly.

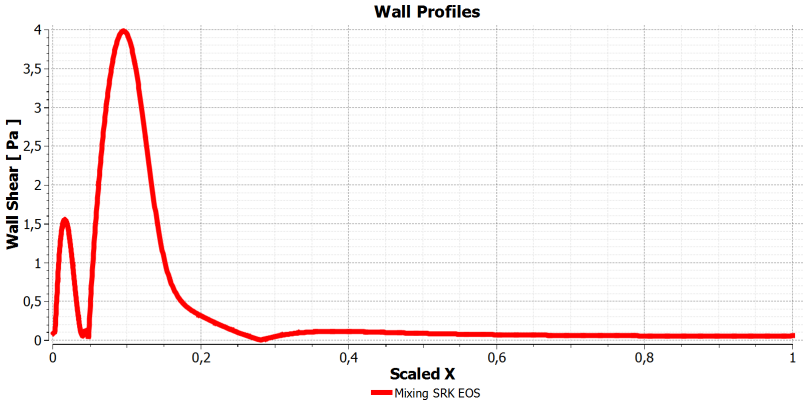

FIGURE 5.67: Mixing Wall Profile Shear

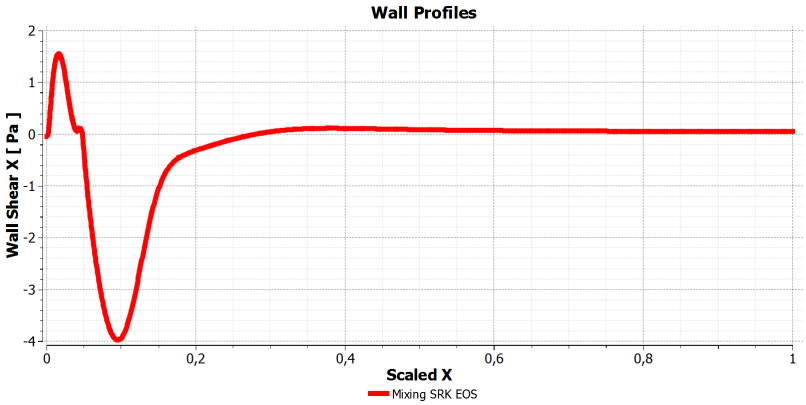

FIGURE 5.68: Mixing Wall Profile Shear X

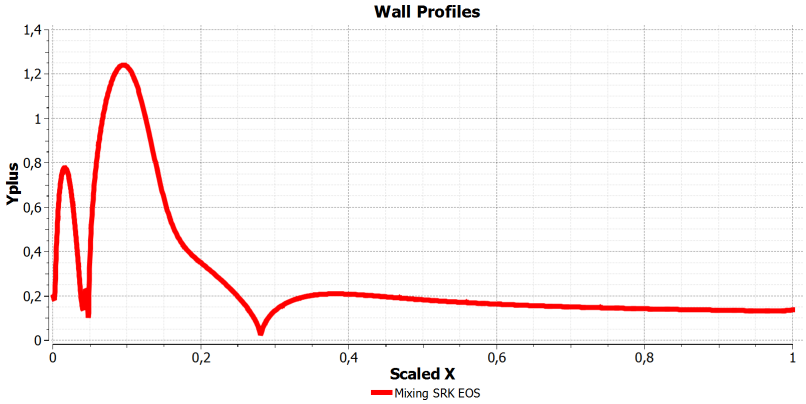

FIGURE 5.69: Mixing Wall Profile Y Plus

Looking especially in Fig. 5.68, one can note how the maximum shear stress (negative) is located in correspondence to the location of the reversed flow (Fig. 5.53). The recirculation

zone present above the injector inlet is the region in which is very important to refine the mesh in order to capture correctly this phenomena.

5.2.2 Combustion

Two main different combustion cases are analysed:

1. Ideal Combustion;
2. *SRK* Combustion;

Reminding the explanation on how the pressure-based solver works, the main difference between the two case is the employed *EOS* in order to compute the density of the mixture. Ideal Combustion means in the present study that the Ideal *EOS* (Eq. 2.15) has been used to compute the density of the species. On the contrary, *SRK* Combustion means that *SRK EOS* (Eq. 4.8) has been employed.

Ideal Combustion

Inlet Profiles Boundary Conditions First, the Ideal Combustion is conducted using profiles that came out from the injectors simulations [4] as inlet boundary conditions in the combustor.

The simulation of the Ideal Gas Combustion is performed until the simulations reach the convergence criteria. The final residuals are shown in Tab. 5.12. At the end of each solver iteration, the residual for each of the conserved variables is computed and stored, thereby recording the convergence history, that can be seen in Fig. 5.70. The absolute convergence criterion in Ansys Fluent is applied. It requires that the globally scaled residuals, decrease to 10^{-3} for all equations except the energy and species equations, for which the criterion is 10^{-6} [21].

iter	221
continuity	9.83e-04
u	1.28e-06
v	7.32e-07
w	7.17e-07
energy	4.69e-07
k	2.50e-06
omega	2.47e-04
ch4	6.81e-07
o2	5.89e-07
co2	2.78e-07
h2o	2.75e-07

TABLE 5.12: Residuals of the Ideal Combustion simulation

[4] Note that these profiles are different from the profiles presented in the previous Sections. In this case, Ideal Gas EOS is employed to compute the density of the species. The simulations of the injectors with Ideal Gas EOS are not included in the current paper.

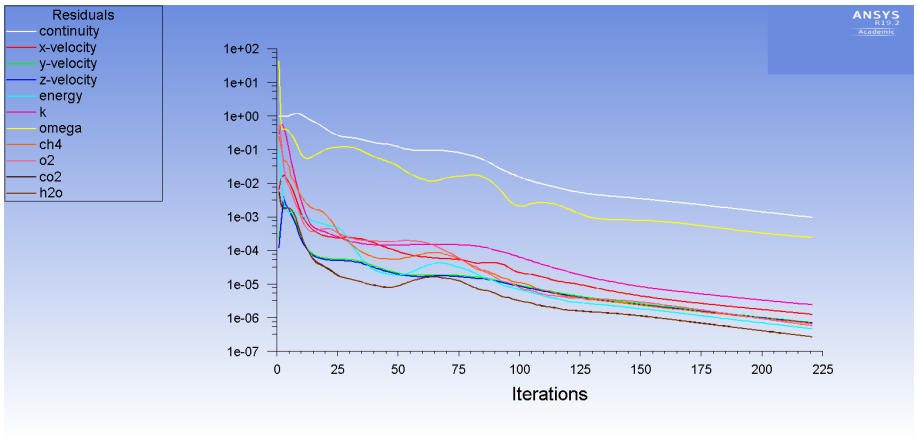

FIGURE 5.70: Convergence History of the Ideal Combustion simulation

The high convergence rate shown in Fig. 5.70 is obtained with a very large time step: the pseudo time-step is set equal to 10^{-3} for all equations except the energy and species equations, for which the value is 10^{-2}.

Fig. 5.71 shows the temperature field in the combustor and in particular it is important to take the flame length into account.

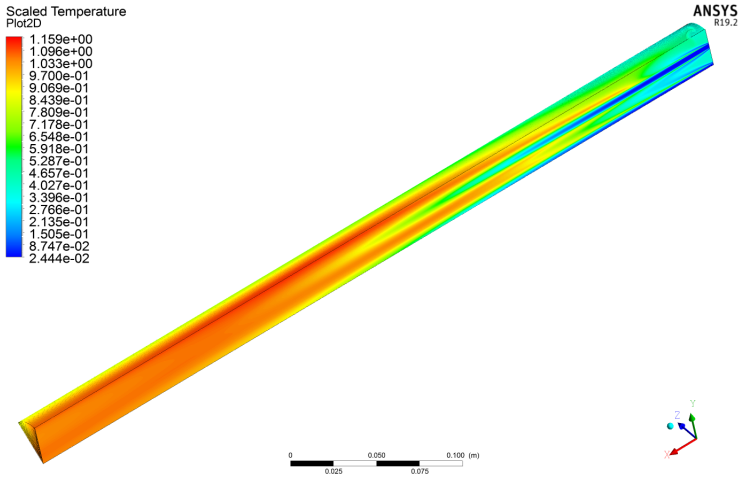

FIGURE 5.71: Ideal Combustion Temperature (Inlet Profiles)

Mass Flow Rate Inlet Boundary Conditions The simulation is conducted with the same Ansys Fluent setup. Only the inlet boundary conditions have been changed to inlet mass flow, prescribing the mass flow with a velocity block. The convergence rate is slower in this case and the simulations take longer to reach the convergence criteria. Taking a look of the following Fig. 5.72, 5.73 and 5.74, it is interesting to note how the flame length decreases.
The turbulence is determined by the turbulent intensity and the hydraulic diameter at inlet condition. Between each different simulations, the only parameter changed is the turbulent intensity at inlet condition[5].

[5]The employed turbulent intensity at inlet condition is written within the different captions of the figures

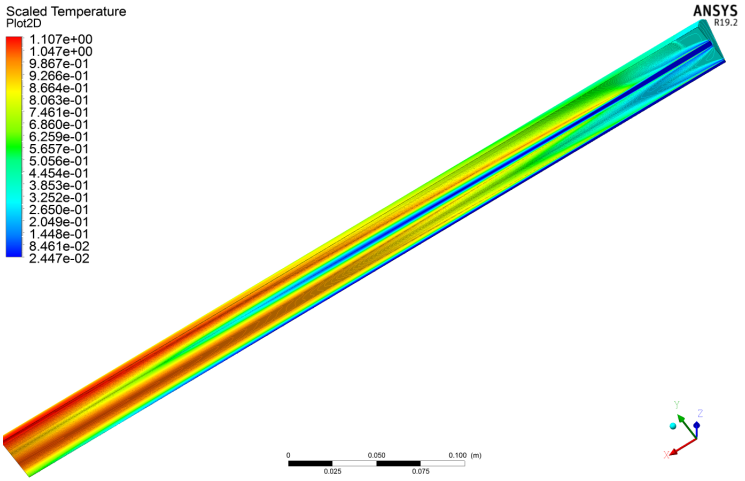

FIGURE 5.72: Ideal Combustion Temperature ($I = 1\%$)

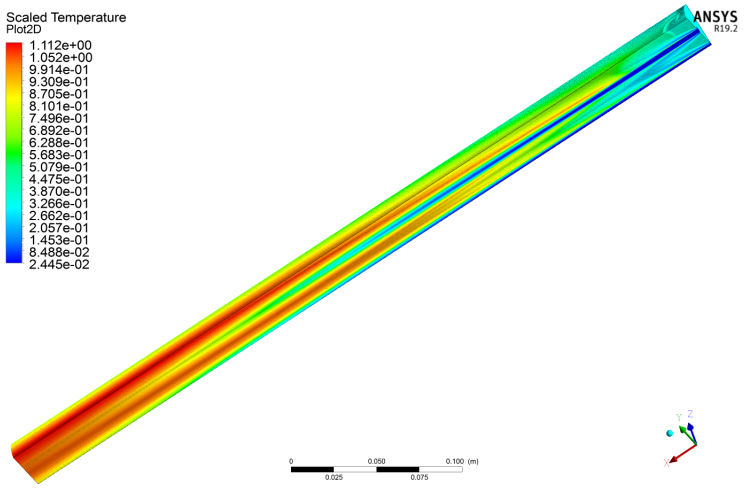

FIGURE 5.73: Ideal Combustion Temperature ($I = 5\%$)

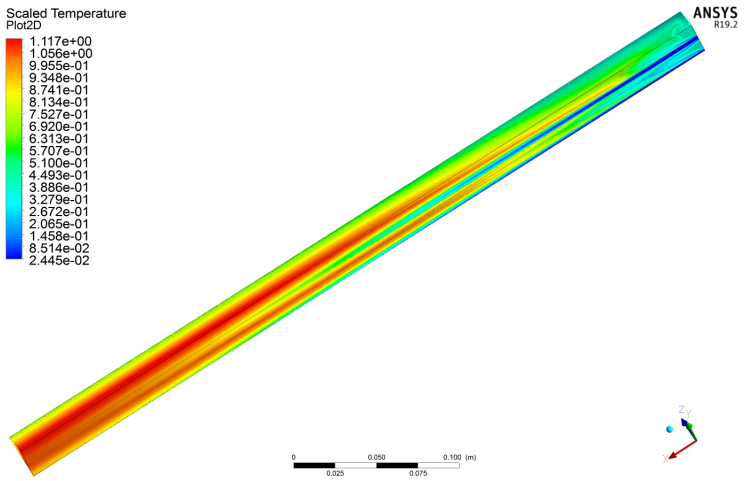

FIGURE 5.74: Ideal Combustion Temperature ($I = 10\%$)

Increasing the turbulent intensity, automatically also the turbulent kinetic energy [6] rises and the mixing after the injector post tip is faster. This effect creates a shorter flame length and a

[6]The plots of the turbulent kinetic energy in the combustor are included in Appendix B.2.1

higher maximum temperature in the combustor. The shortest flame length is the one in Fig. 5.71, where the correct profiles are used as inlet boundary conditions. This explains briefly how important the simulations of the injectors are and how the turbulence influences the flame length.

SRK Combustion

The issues with obtaining a stationary flow fields starts to appear in combustion with *EDM* combustion model when *SRK EOS* has been activated to compute the density of the species. Instabilities appear in the combustion process. The simulations do not reach the convergence criteria and it seems that the *EDM* with a single-step reaction is not reliable if the real gas law is switched on. It works very well for Ideal Combustion, but unfortunately it requires optimization to solve correctly the real behaviour of the cryogenic propellants.
Different trials have been made for the *SRK* Combustion. In particular, three different initialization of the numerical domain were tested. The simulation of the real gas has been started from:

- a fully mixed solution;
- an Ideal Gas Combustion solution;
- scratch (initial pressure, temperature, velocity, mass fractions and turbulent parameters set for the whole domain by user).

Different initializations give different behaviours in the first iterations and different convergence rate of the simulations. In any case, the *EDM* model in combination with the real gas *SRK EOS* is very unstable for this test case (maybe due to the properties of the injected reactants) and it is very difficult stabilizing the simulations to obtain good results in terms of flame shape and temperature in the combustion chamber.

2D Simulations After many 3D simulation tests, the choice to switch from 3D simulations to 2D simulations was taken. In particular, since the *SRK* combustion does not work properly, a 2D study has been conducted in order to understand the reasons of the combustion instabilities. 2D geometry and meshes were created without taking the injectors into account and many tests on *SRK* Combustion have been performed. The most suitable results were found initializing the flow with a "modified" Ideal Combustion. First, an Ideal Combustion with high inlet temperatures of the reactants has been conducted. Fig. 5.75 shows the temperature field in the combustor.

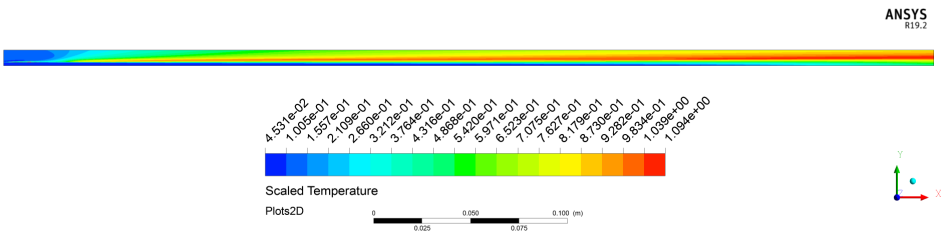

FIGURE 5.75: Ideal Combustion Temperature 2D

Then the *SRK* Combustion has been initialized form the results of this simulation. Subsequently, the injection temperature has been decreased step by step (few degrees each simulation). More the inlet temperatures decreases, more the behaviour of the species is far away from the ideal behaviour (the real gas effects becomes more important) and more instabilities appear in the simulations. The following figures show the temperature field in the combustor at each steps [7].

[7] In Appendix B.2.2, the density plots are included and it is possible to note directly the effects of the *SRK EOS* density computation

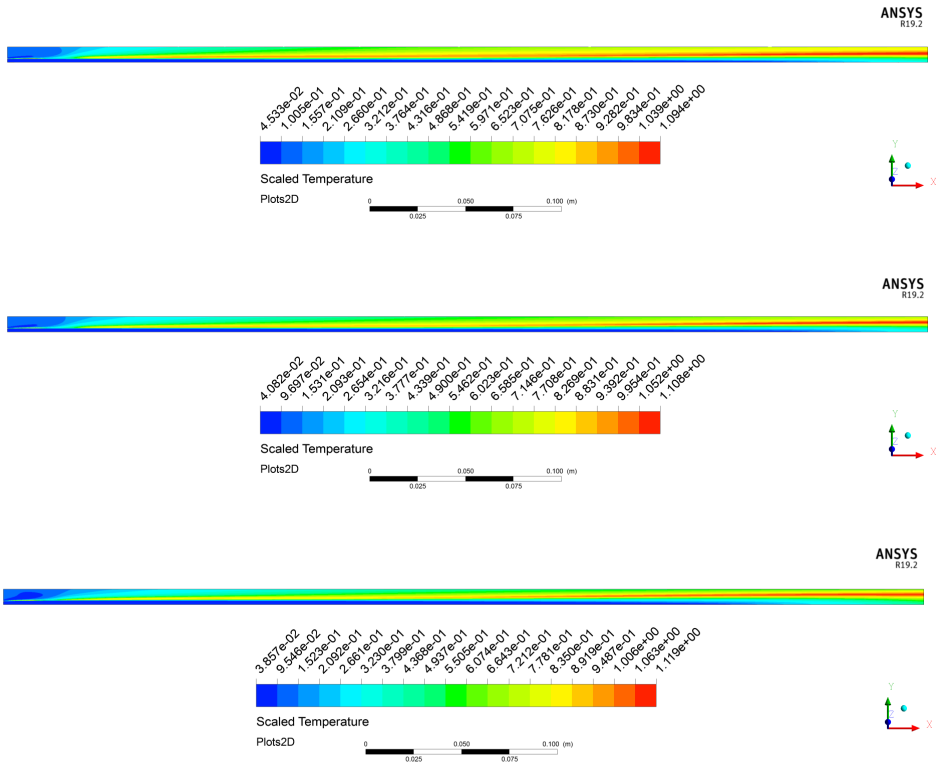

FIGURE 5.76: SRK Combustion Temperature 2D ("high" inlet temperatures)

It is possible to reach an inlet temperature of the oxygen approximately equal to 170K. Above this value, the simulations reach the absolute default convergence criteria. Fig. 5.77 shows the convergence history of the simulations. The high convergence rate is obtained with a very large time step: the pseudo time-step is set equal to 10^{-3} for all equations except the energy and species equations, for which the value is 10^{-2}.

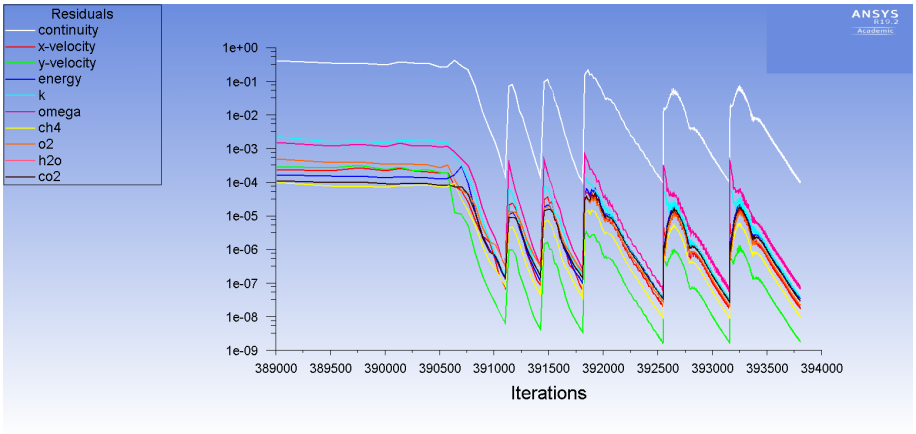

FIGURE 5.77: Convergence History of the SRK Combustion simulation

If the oxygen is injected with an inlet temperature below 170K, as the following figures show, the flame's shape deteriorates and the simulations do not reach the convergence criteria.

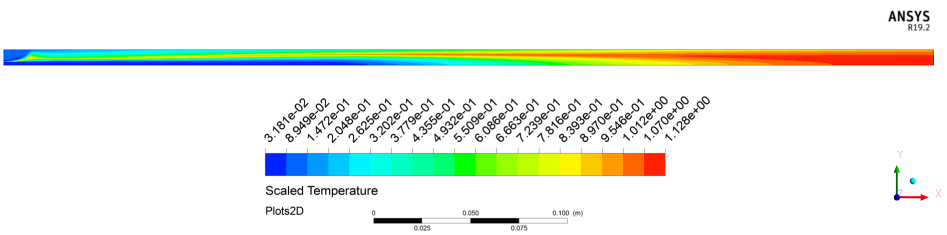

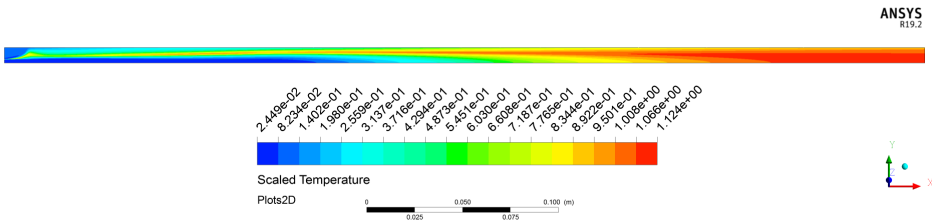

FIGURE 5.78: SRK Combustion Temperature 2D ("low" inlet temperatures)

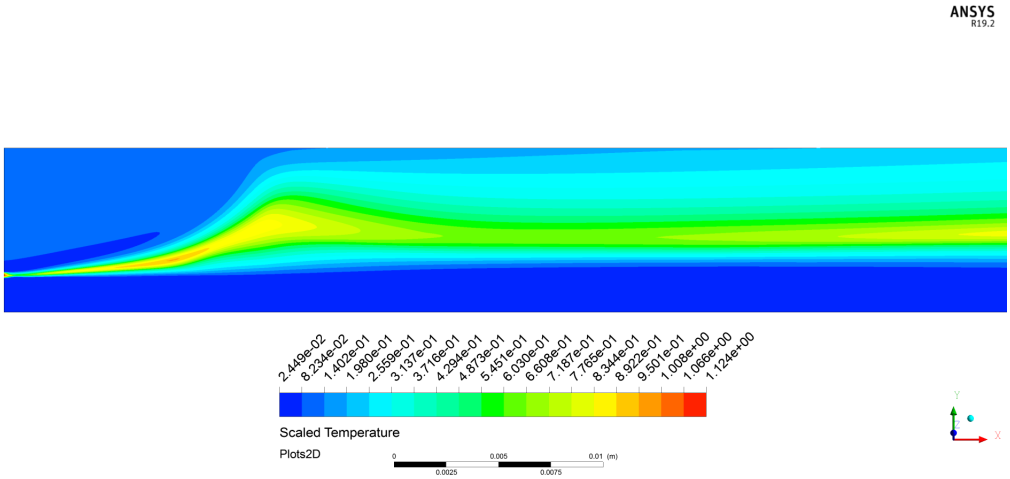

FIGURE 5.79: Deteriorated Flame

The conclusion that the *EDM* combustion model in conjunction with *SRK EOS* without any kind of chemical mechanisms is not reliable at the moment in order to simulate properly the combustion with cryogenic propellants is taken. Thanks to this work a talk with Ansys on the subject has begun and maybe in the future this method will be stabilized.

Chapter 6

Conclusions and Outlooks

The present work has been focused on the numerical simulations of combustion phenomenon in a typical liquid-gaseous propellant rocket engine using Ansys Fluent 19.2. Transcritical combustion of liquid oxygen and gaseous methane has been modelled numerically using a *RANS* approach and the *EDM* combustion model with a single-step reaction for a sub-scale combustor with 5 shear coaxial elements. The *SST* k-ω model is used for the turbulence closure .

By stepping back, first, a thermodynamic study is conducted to analyse the properties of the reactants at inlet condition. The real gas data at constant chamber pressure are taken from the *NIST* real gas database [9]. In order to compute the correct value of the species' density, a study is conducted in Section 4.2 taking into account the different real gas *EOS* present in literature. Analysing the results of the comparison between the different equations of state, *SRK EOS* is chosen to taken into account the real gas effects. *SRK EOS* has been successfully validated in the injectors and mixing simulations, but unfortunately, not in the combustion simulations.
In order to model the transport properties (dynamic viscosity and thermal conductivity) of the species involved in the global reaction properly, a comparative study is conducted in Section 4.3 between *NIST* real gas data and classical employed methods from literature. It was shown that that for the current work, these methods (as for example Sutherland and Power Law) are not reliable. In fact, methane and oxygen are injected close to the critical conditions and the behaviour of the properties is really unstable and unpredictable with the classical validated methods. Unfortunately, Ansys Fluent 19.2 contains the RefProp Tables of the *NIST* database, but they can be used only for a single species and without considering any kind of reaction. For this reason, piecewise-polynomials functions are created to fit the transport properties of the *NIST* real gas data. These polynomials are able to predict correctly the values of the properties at constant chamber pressure (important assumption) and they are successfully verified with the injectors and mixing simulations.

The injectors and the combustion chamber simulations are conducted separately. The first step is the validation of the injectors simulations results (Section 5.1). The *NIST* data are used to compute the reference results of the injectors. Then, the simulations using *SRK EOS* and piecewise-polynomials functions are conducted. In both cases, the simulations reach the default-convergence criteria in Ansys Fluent. The results of the two simulations are compared and in this way the *SRK EOS* and piecewise-polynomials functions are verified and validated for the injectors simulations at the specific test case conditions.

Successively the outlet profiles coming out from the injectors simulations are extrapolated and interpolated in the combustion chamber setup as inlet boundary conditions. The coupling between injectors and combustor simulations is successfully verified in Section 5.2.1 where the inlet profiles in the combustor are shown.

Three main different kinds of simulations in the combustion chamber are conducted:

- Mixing (Section 5.2.1);
- Ideal Combustion (Section 5.2.2);
- *SRK* Combustion (Section 5.2.2).

The Mixing simulation reach the convergence criteria and it is successfully validated also considering the theory of the diffusion flame exposed in Section 2.4. A refinement of the mesh is conducted to assure the convergence of the method with an acceptable convergence rate. Moreover, it was necessary to compute the behaviour of the flow close to the wall properly following the requirement discussed in Section 3.2.1.

Ideal Combustion means in the present study that the Ideal *EOS* (Eq. 2.15) has been used to compute the density of the species. The same mesh validated with the Mixing simulation has been used. The simulation reaches converges criteria at a very good convergence rate. This part has also been used to understand briefly how the turbulence parameters influence the mixing rate and consequently the flame length.

The issues with getting a stationary flow field start to appear in combustion with *EDM* combustion model when *SRK EOS* has been activated to compute the density of the species (*SRK* Combustion). Instabilities appear in the combustion process. The simulations do not reach the convergence criteria and it seems that *EDM* with a single-step reaction is not reliable if the real gas law is switched on. It works very well for Ideal Combustion, but unfortunately it requires optimization to solve correctly the real behaviour of the cryogenic propellants.
Different trials have been made for the *SRK* Combustion. In particular, three different initialization of the numerical domain have been tried, the simulation of the real gas has been started from:

- Mixing solution;
- Ideal Gas Combustion solution;
- Scratch (initial pressure, temperature, velocity, mass fractions and turbulent parameters set for the whole domain by user).

Moreover, different methods (coupled and not, pseudo-transient and steady) to solve the governing equations have been tried. However, in each case there are unreliable results that came out from the simulations.

After these considerations, the choice to switch from 3D simulations to 2D simulations was taken. In particular, since the *SRK* combustion does not work properly, a 2D study has been conducted in order to understand the reasons of the combustion instabilities (Section 5.2.2). 2D geometry and meshes were created without taking the injectors into account and many trials on *SRK* Combustion have been performed. The most suitable results were found initializing the flow with a "modified" Ideal Combustion. First, an Ideal Combustion with high inlet temperatures of the reactants has been conducted. Then the *SRK* Combustion has been started form the results of this simulation. Subsequently, the injection temperatures have been decreased step by step (few degrees each simulation). The more the inlet temperatures decreases, the more the behaviour of the species is shifts away from the ideal behaviour (the real gas effects becomes more important) and more instabilities appear in the simulations. It is possible to reach an inlet temperature of the oxygen approximately equal to $170K$. Below this value, the simulations do not convergence and the flame's shape deteriorates. The conclusion that the *EDM* combustion model in conjunction with *SRK EOS* without any kind of chemical mechanisms is not reliable at the moment in order to simulate properly the combustion with cryogenic propellants is taken. Thanks to this work a talk with Ansys on the subject has begun and maybe in the future this method will be stabilized.

Future Developments As said before, one possible development could be trying to stabilize the simulated flame with the method employed in the current work. In literature no works have been found using all the characteristics employed in the current researching project and it could be interesting to use *EDM* also in these conditions and seeing what is coming out from the simulations.
Kozubkovaá et al. [4] focused on the creation of the mathematical model of methane turbulent combustion usign Ansys Fluent 13.0 software. *EDM* with a single-step reaction has been the employed combustion model but the Ideal *EOS* has been used to compute the density of the species. On the contrary, *Sharma et al.* [3] chose to employ the *SRK* real gas equation

of state to account for real gas effects. However, the combustion is analysed with a non-premixed non-adiabatic steady flamelet model. Finally, at DLR Institute of Space Propulsion *Dr. Zhukov* [40] focused on a *GO2/GH2* combustion chamber with a single shear coaxial injector. The turbulent flow in the combustion chamber is modelled using *FANS* equations and the *SST* model for turbulence closure. The turbulent non-premixed flame is modelled using an extended eddy dissipation model.

Moreover, a method to extend the eddy-dissipation model in Ansys Fluent searching to limit the flame's temperature is under-development. The aim is to adapt the eddy-dissipation model to be used in computational fluid dynamics simulations of methane combustion in rocket engine combustion chambers within Ansys Fluent, which is the de-facto industrial standard for *CFD*. The model shall accurately predict the temperature of combustion products after the adaptation. The adaptation will be achieved through the accurate evaluation of the coefficients of the eddy-dissipation model and properties of burnt gases. The results of the adapted model will be evaluated through the use of NASA Chemical Equilibrium with Applications (*CEA*) code. The thermodynamic and transport properties of the burnt gases produced by the adapted model will be compared against those produced by the NASA CEA code

Finally, the present project is part of a collaboration between *DLR* and *CNES*. *CNES* provides experimental data on the wall heat flux which have to be compared with the results that come out of the numerical simulations. A comparison between the simulation done at *DLR* and the simulations done at *CNES* has to be conducted in detail. It could be interesting to examine the differences between the two results due to different numerical software and methods employed to solve the *CH4/LOX* trans-critical combustion problem.

Appendix A

Real Gas Effects Plots

A.1 Density

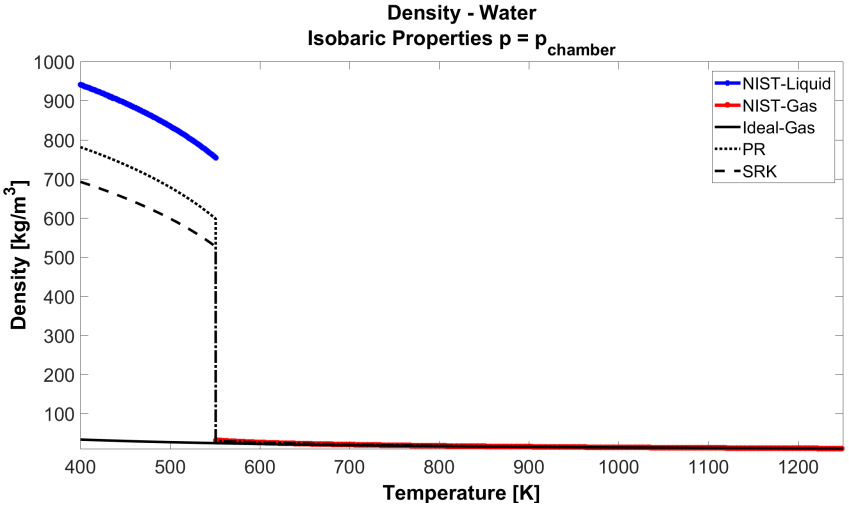

FIGURE A.1: Water Density/Temperature Plot

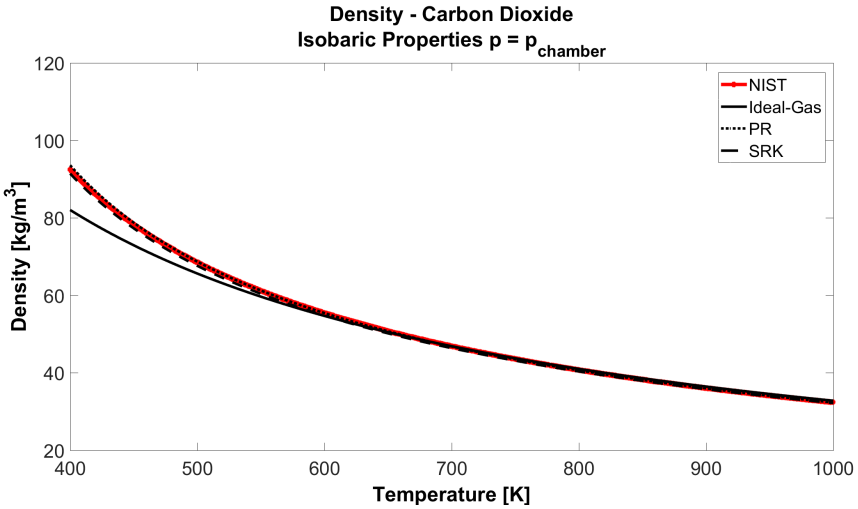

FIGURE A.2: Carbon Dioxide Density/Temperature Plot

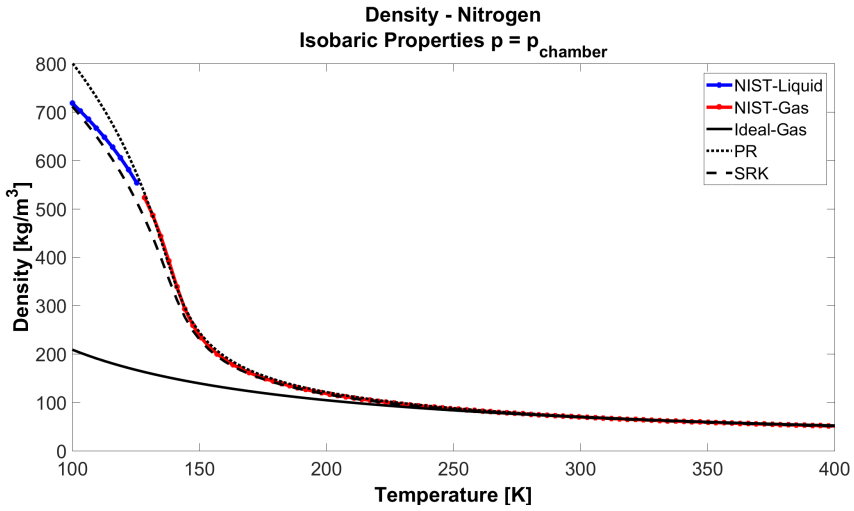

FIGURE A.3: Nitrogen Density/Temperature Plot

A.2 Dynamic Viscosity

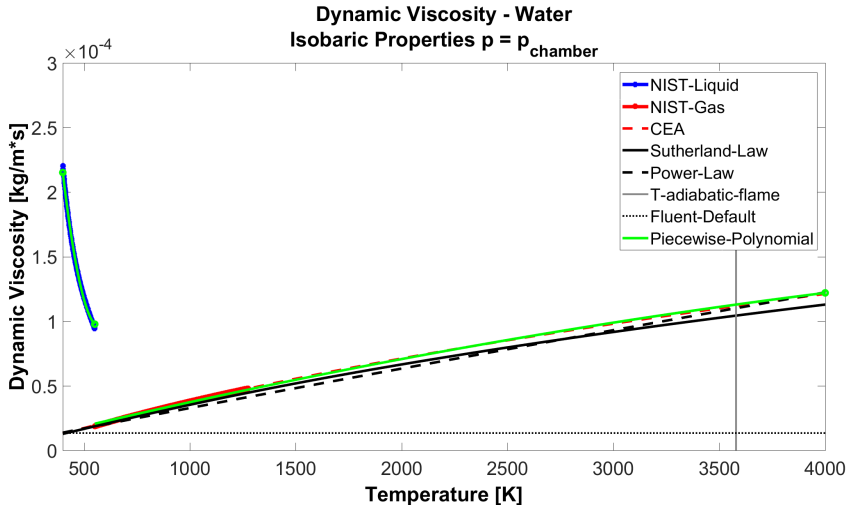

FIGURE A.4: Water Dynamic Viscosity/Temperature Plot

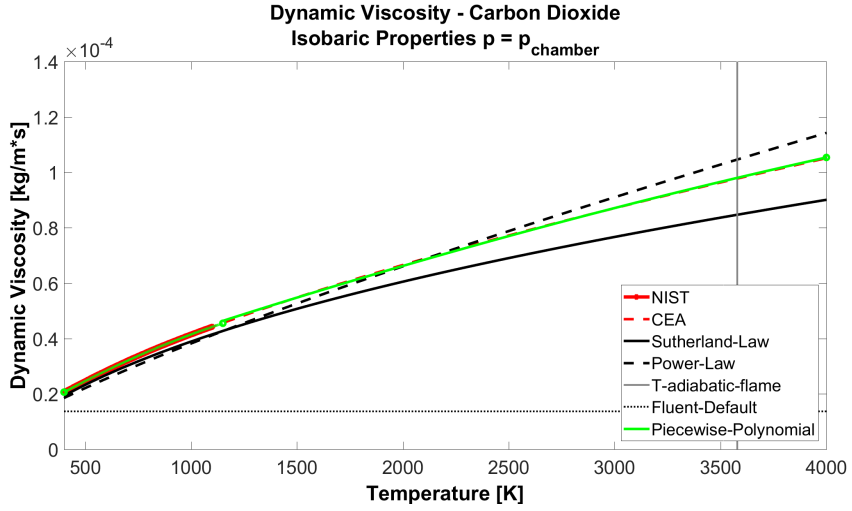

FIGURE A.5: Carbon Dioxide Dynamic Viscosity/Temperature Plot

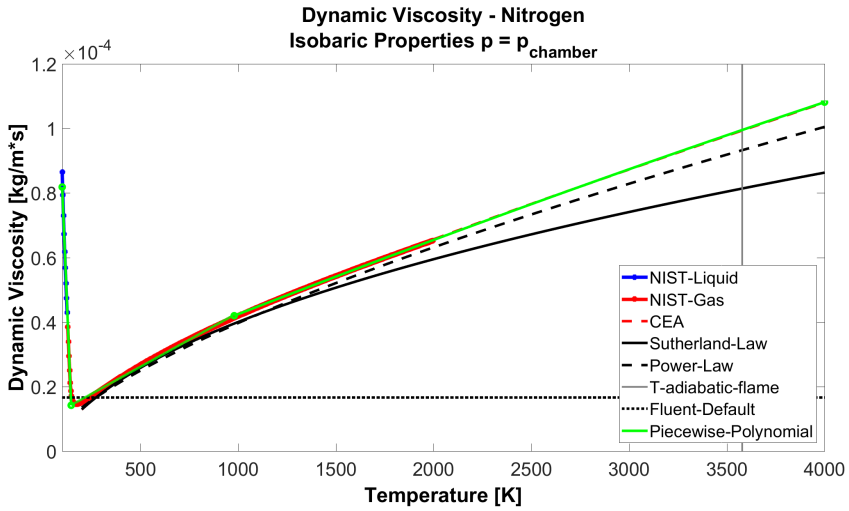

FIGURE A.6: Nitrogen Dynamic Viscosity/Temperature Plot

A.3 Thermal Conductivity

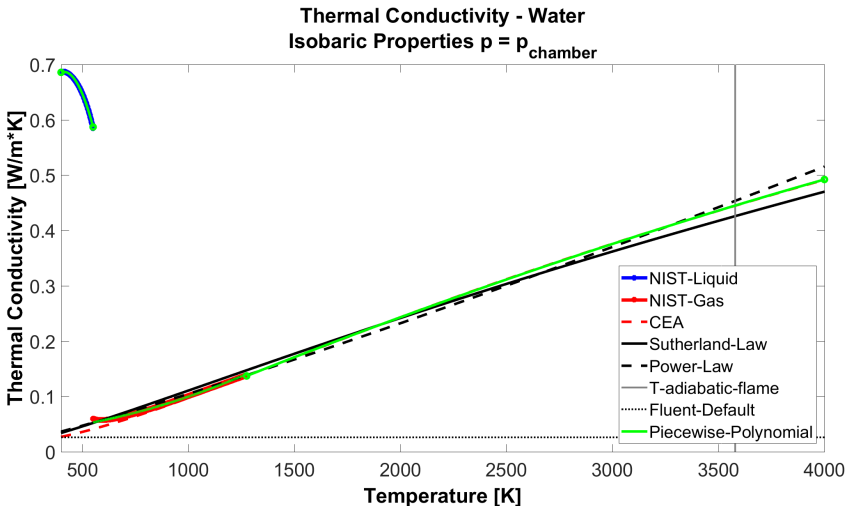

FIGURE A.7: Water Thermal Conductivity/Temperature Plot

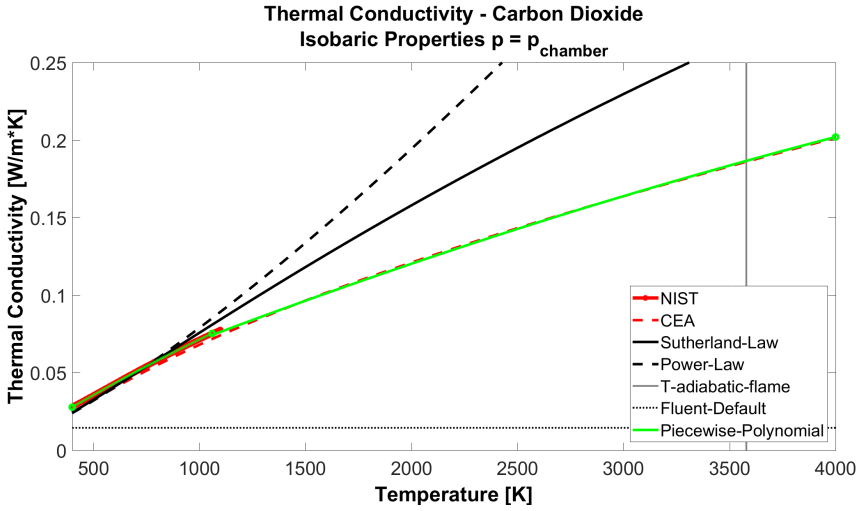

FIGURE A.8: Carbon Dioxide Thermal Conductivity/Temperature Plot

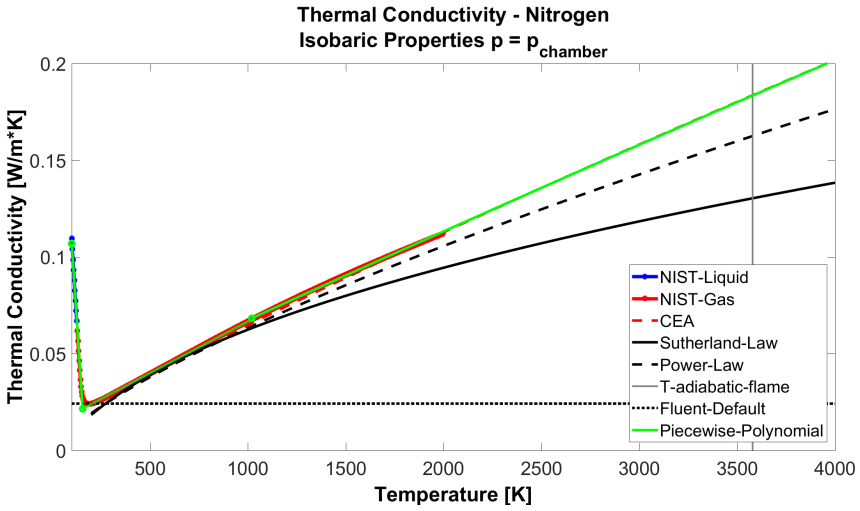

FIGURE A.9: Nitrogen Thermal Conductivity/Temperature Plot

A.4 Specific Heat Capacity

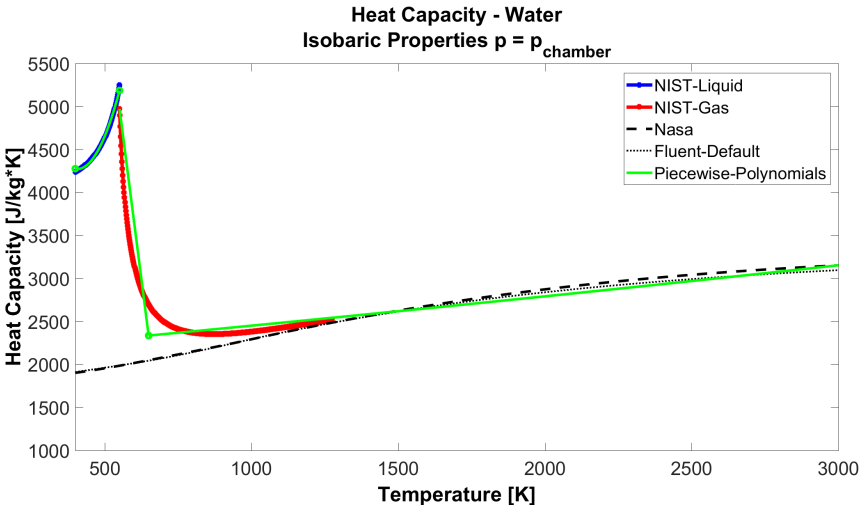

FIGURE A.10: Water Heat Capacity/Temperature Plot

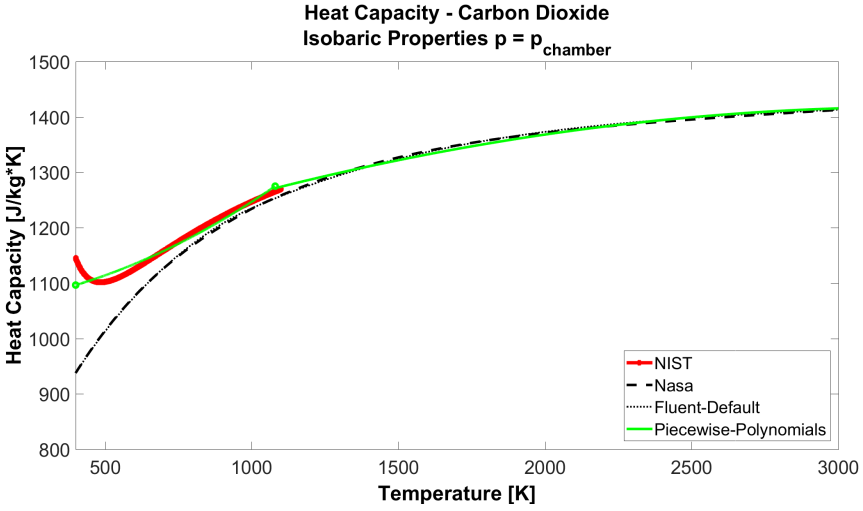

FIGURE A.11: Carbon Dioxide Heat Capacity/Temperature Plot

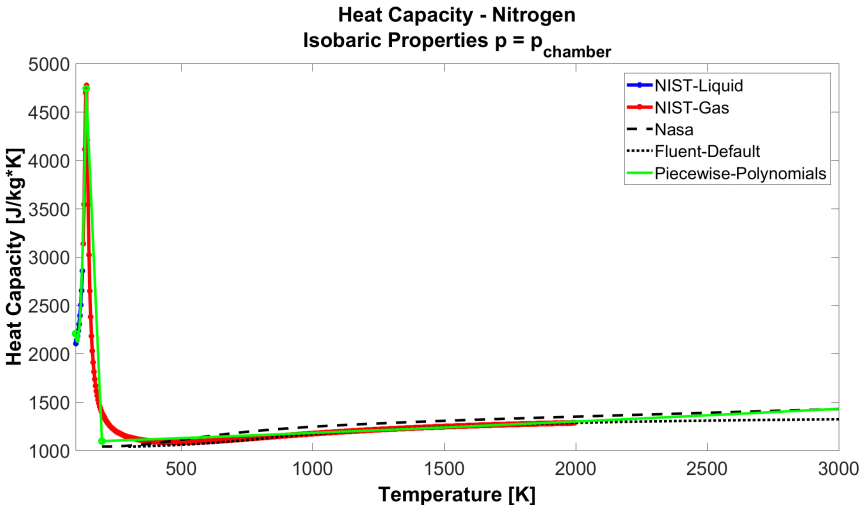

FIGURE A.12: Nitrogen Heat Capacity/Temperature Plot

Appendix B

Results Plots

B.1 Injectors

B.1.1 Inlet and Outlet: 45 and 180 degrees sectors

Methane

Inlet

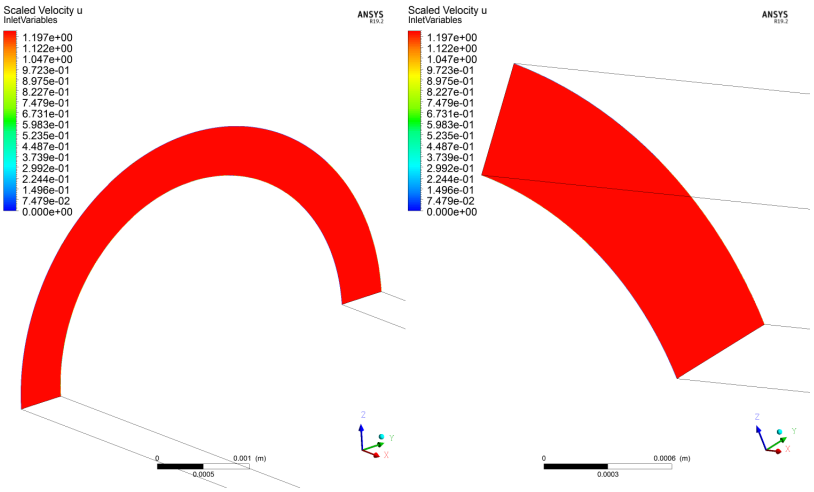

FIGURE B.1: Methane Inlet Velocity

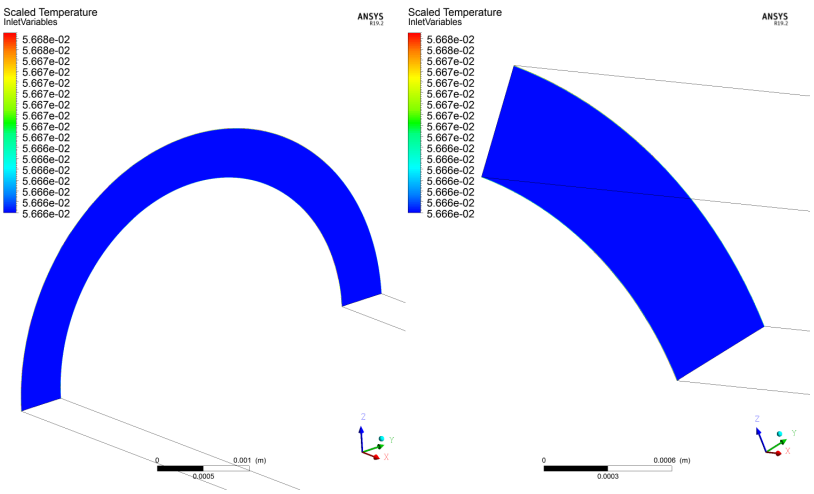

FIGURE B.2: Methane Inlet Temperature

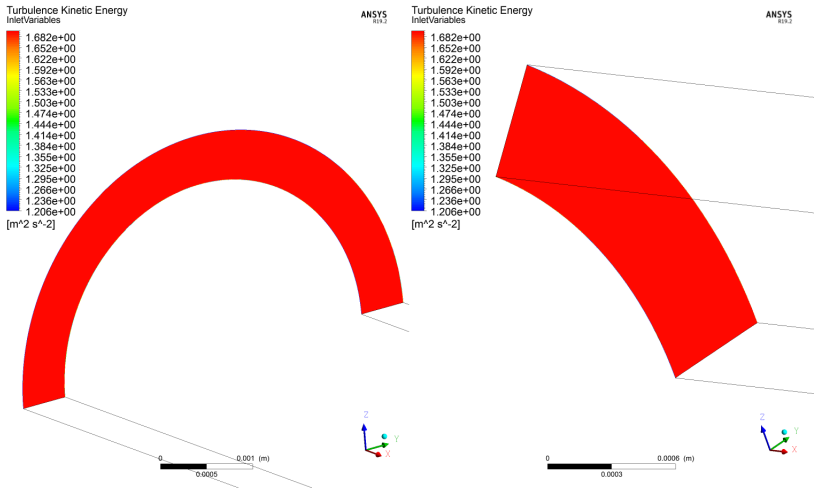

FIGURE B.3: Methane Inlet Turbulent Kinetic Energy

Outlet

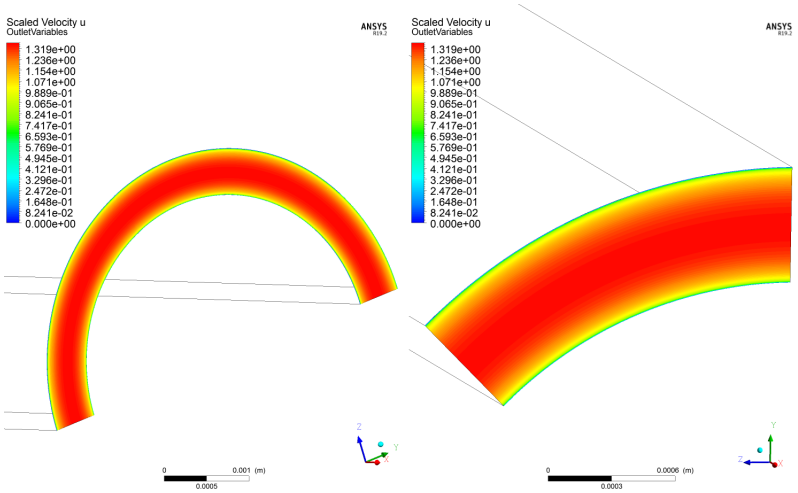

FIGURE B.4: Methane Outlet Velocity u

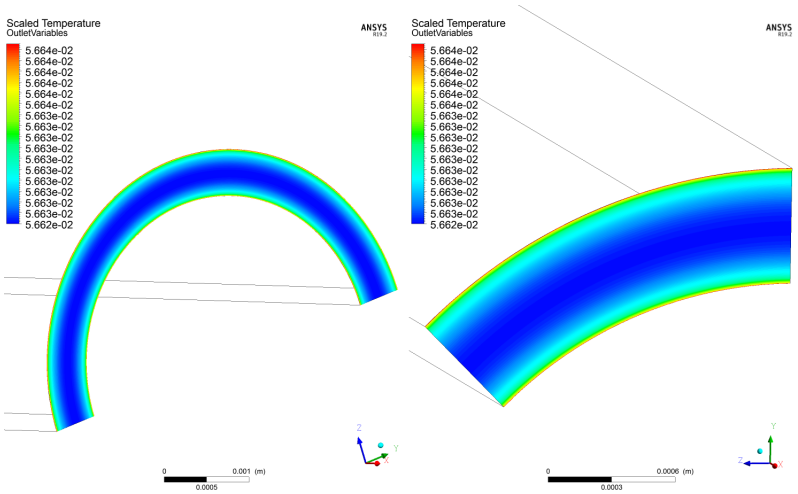

FIGURE B.5: Methane Outlet Temperature

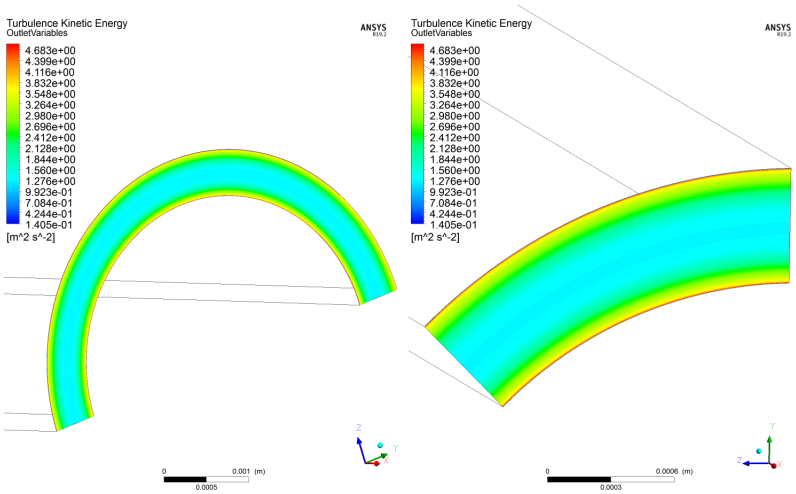

FIGURE B.6: Methane Outlet Turbulent Kinetic Energy

Oxygen

Inlet

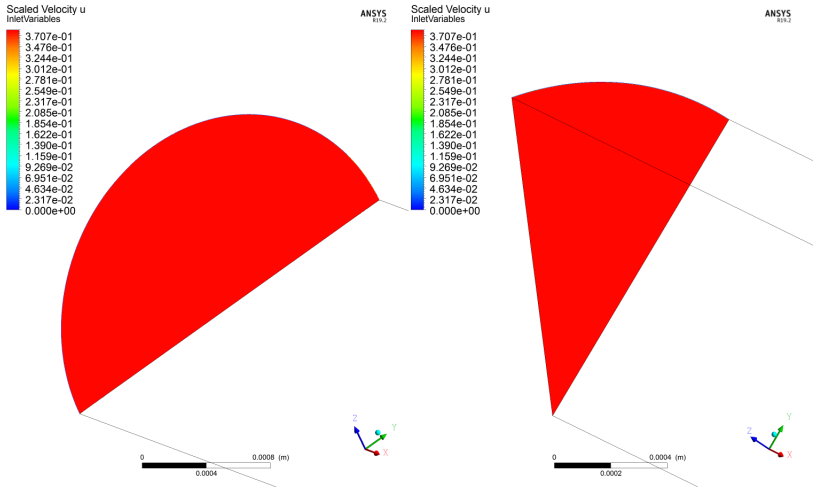

FIGURE B.7: Oxygen Inlet Velocity

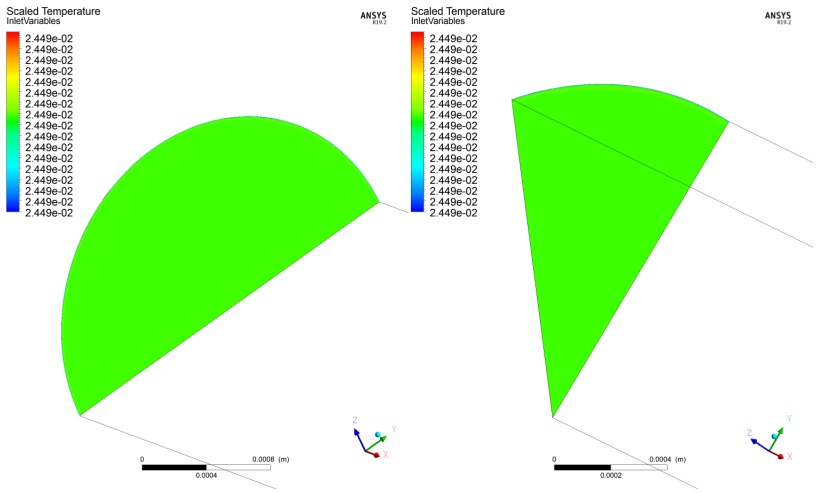

FIGURE B.8: Oxygen Inlet Temperature

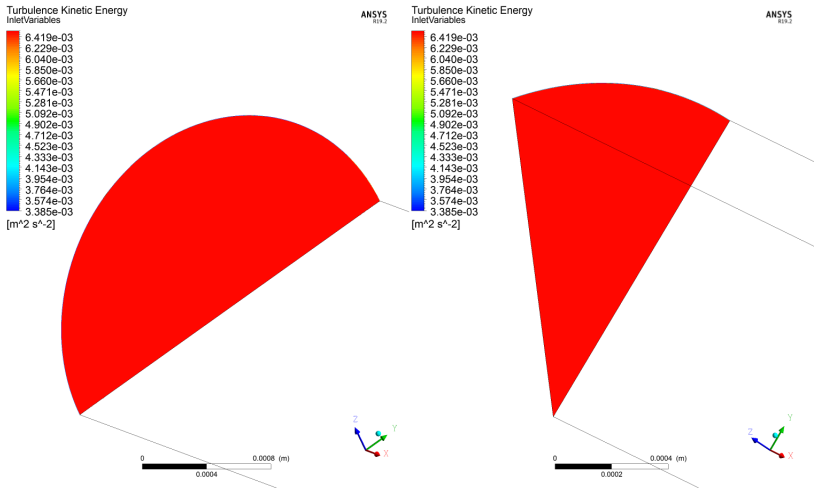

FIGURE B.9: Oxygen Inlet Turbulent Kinetic Energy

Outlet

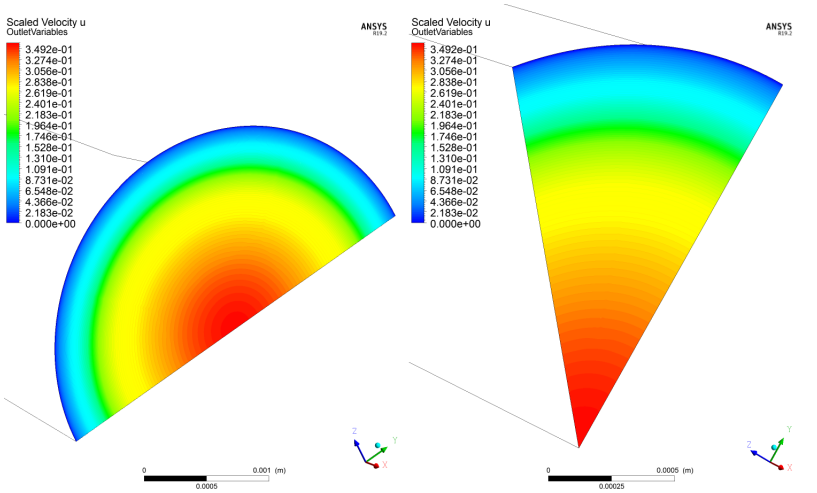

FIGURE B.10: Oxygen Outlet Velocity u

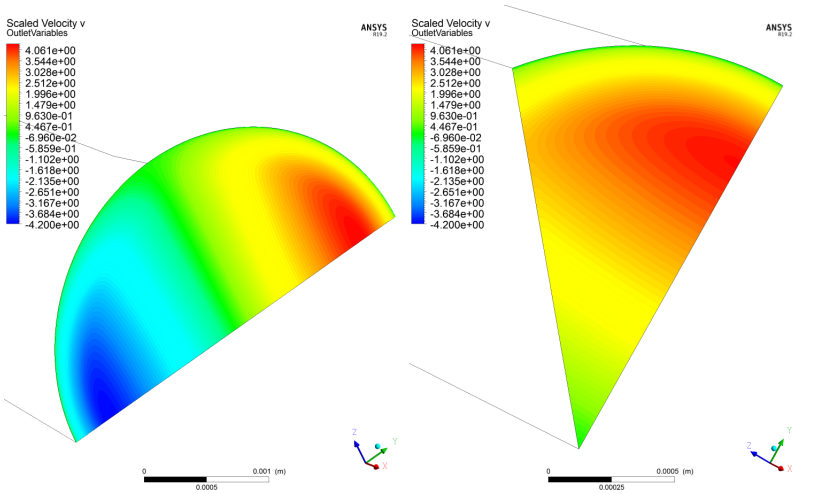

FIGURE B.11: Oxygen Outlet Velocity v

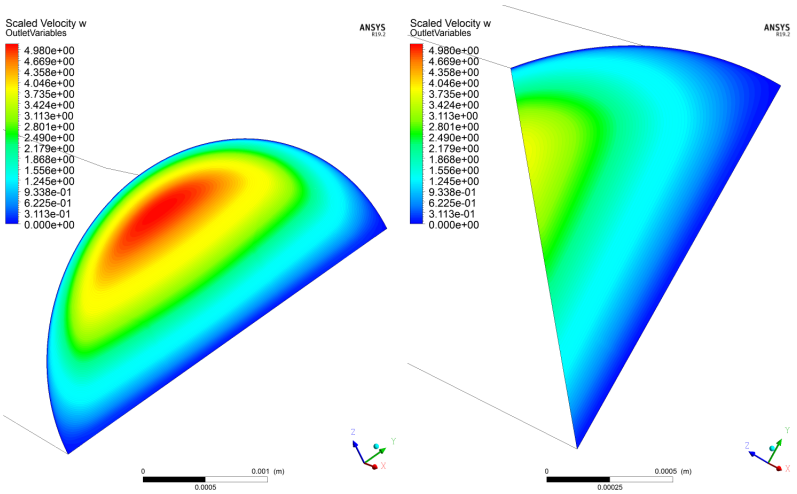

FIGURE B.12: Oxygen Outlet Velocity w

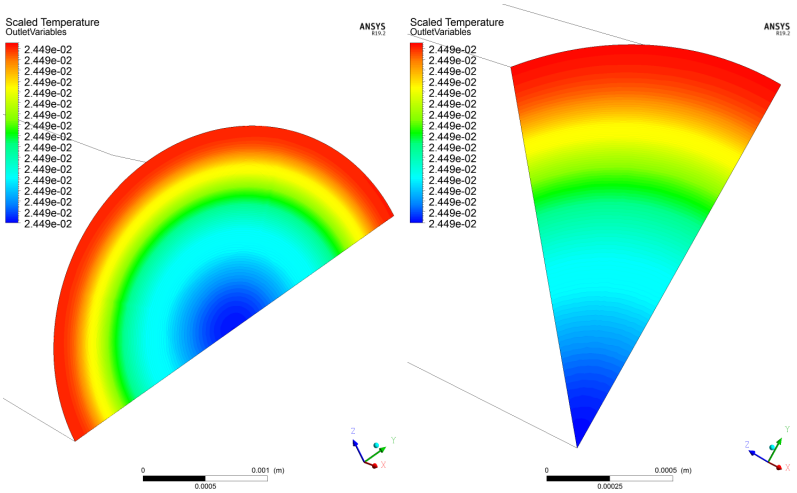

FIGURE B.13: Oxygen Outlet Temperature

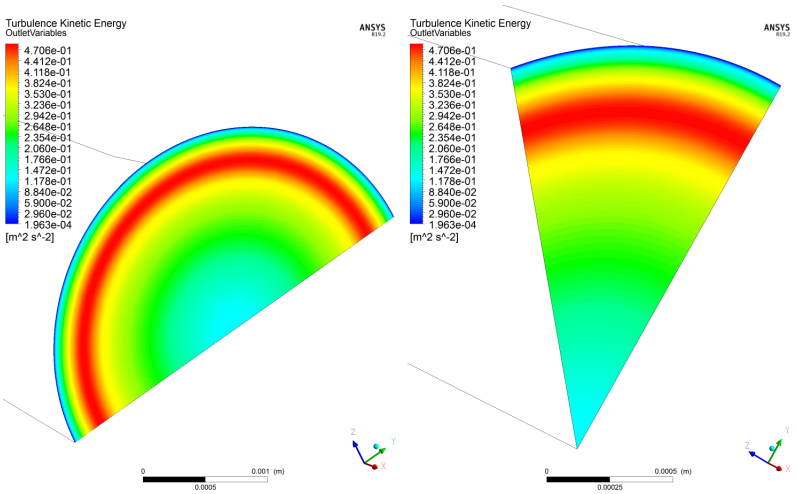

FIGURE B.14: Oxygen Outlet Turbulent Kinetic Energy

B.2 Combustion

B.2.1 Ideal Combustion

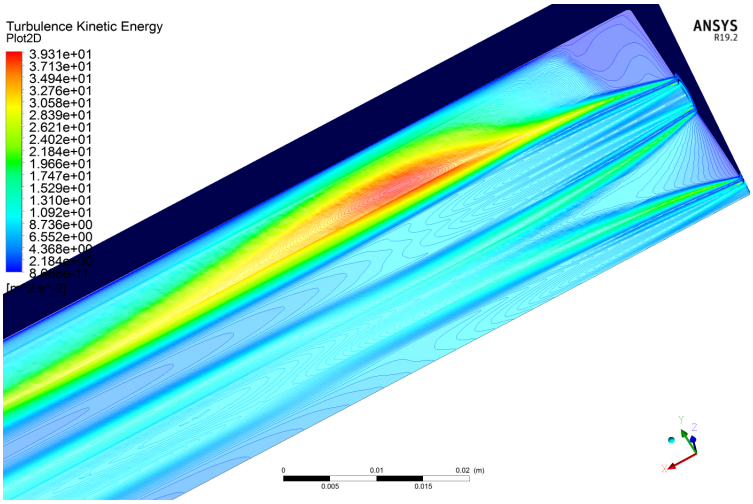

FIGURE B.15: Ideal Combustion Turbulent Kinetic Energy (Inlet Profiles)

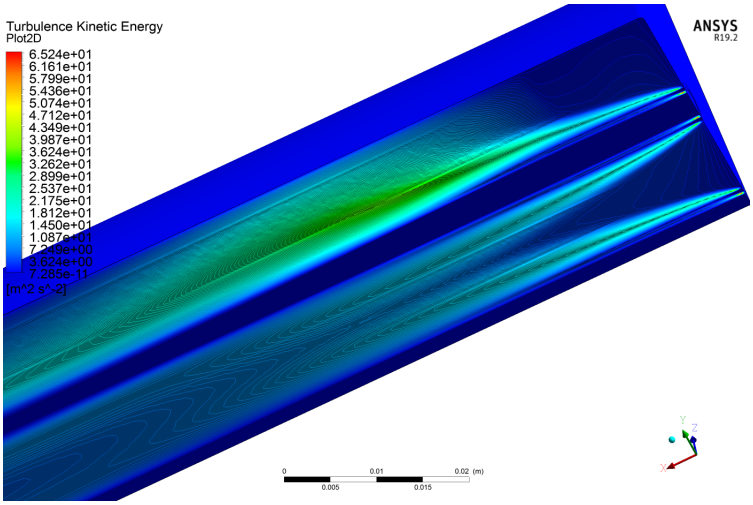

FIGURE B.16: Ideal Combustion Turbulent Kinetic Energy ($I = 1\%$)

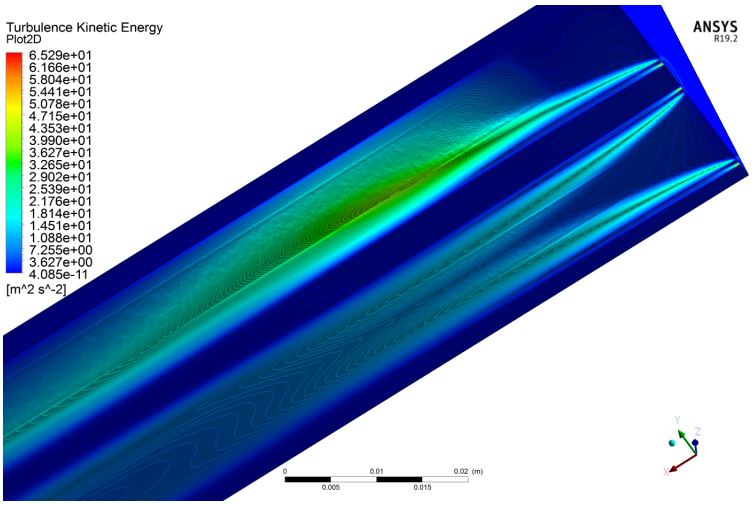

FIGURE B.17: Ideal Combustion Turbulent Kinetic Energy ($I = 5\%$)

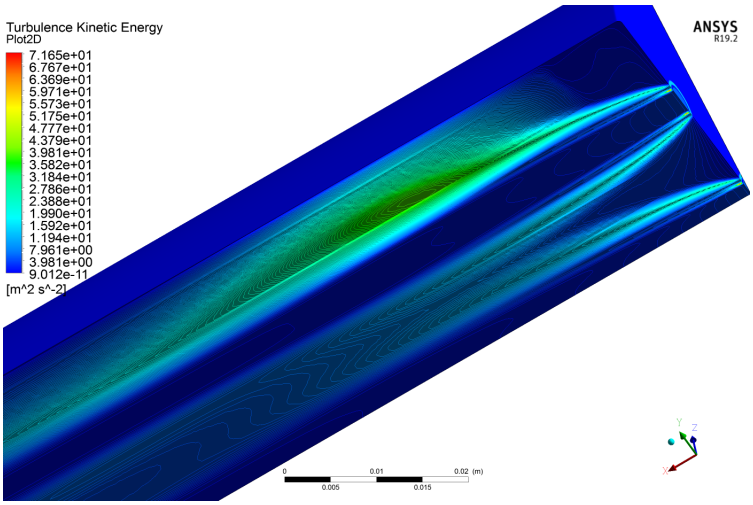

FIGURE B.18: Ideal Combustion Turbulent Kinetic Energy ($I = 10\%$)

B.2.2 SRK Combustion

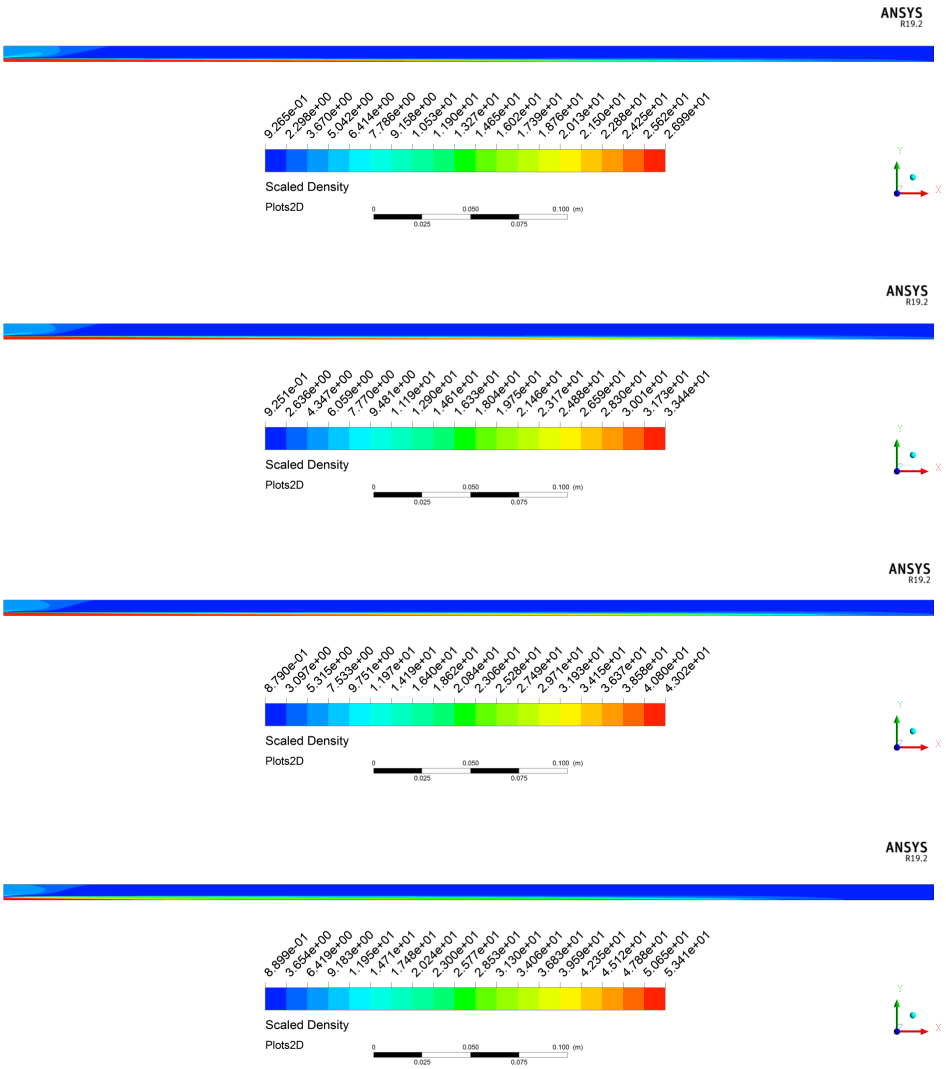

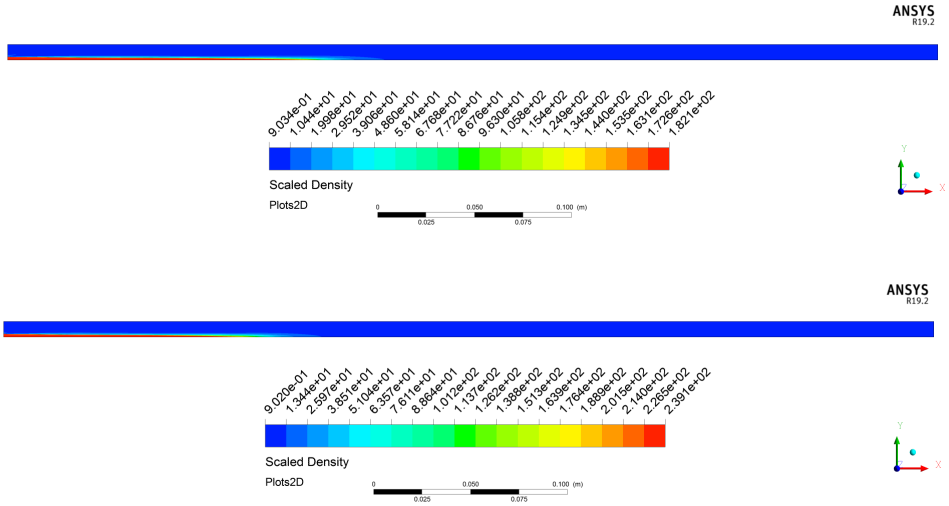

FIGURE B.19: SRK Combustion Density 2D

Bibliography

[1] *Adiabatic Flame Temperature Calculator*. 2019. URL: http://elearning.cerfacs.fr/combustion/tools/adiabaticflametemperature/index.php.

[2] *Adiabatic flame temperature Computation*. 2019. URL: http://elearning.cerfacs.fr/combustion/n7masterCourses/adiabaticflametemperature/index.php.

[3] Abhishek Sharmaa et all. "Numerical Modelling of Supercritical Combustion in LOX/Methane Multi Element Chamber". In: *IAC* (2018). URL: https://www.researchgate.net/publication/327954630_NUMERICAL_MODELLING_OF_SUPERCRITICAL_COMBUSTION_IN_LOXMETHANE_MULTI_ELEMENT_CHAMBER.

[4] Milada KOZUBKOVÁ et all. "Mathematical Modelling of Methane Combustion". In: *Safety Engineering* (2012). URL: https://www.researchgate.net/publication/311784210_Mathematical_Modeling_of_Methane_Combustion.

[5] Yimer I. et all. "Estimation of the Turbulent Schmidt Number from Experimental Profiles of Axial Velocity and Concentration for High-Reynolds-Number Jet Flows". In: *Canadian Aeronautics and Space Journal* 48.3 (2002), pp. 195–200. URL: https://pubs.casi.ca/doi/abs/10.5589/q02-024.

[6] Peter Bruce. *The Ideal Gas*. 2019. URL: https://slideplayer.com/slide/8042805/.

[7] *Chemical Equilibrium with Application (CEA)*. 2019. URL: https://www.grc.nasa.gov/WWW/CEAWeb/.

[8] "CHEMKIN Tutorials Manual". In: *Reaction Design* (Dec. 2011). URL: https://personal.ems.psu.edu/~radovic/ChemKin_Tutorial_2-3-7.pdf.

[9] U.S. Secretary of Commerce on behalf of the United States of America. *WebBook de Chimie NIST*. 2018. URL: https://webbook.nist.gov/chemistry/fluid/.

[10] *Conservation equations for combustion (part 1)*. 2019. URL: http://elearning.cerfacs.fr/combustion/n7masterCourses/conservationequations/index.php.

[11] *Enhanced Wall Treatment*. 2009. URL: http://www.afs.enea.it/project/neptunius/docs/fluent/html/th/node101.htm.

[12] Esch T. Menter F. "Heat transfer predictions using advanced two-equation turbulence models". In: *European Metallurgical Conference* 3 (2003), pp. 1157–1170. URL: https://www.tib.eu/en/search/id/tema%3ATEMA20040105793/Heat-transfer-predictions-using-advanced-two-equation/.

[13] Kurt Heckman. *Peng-Robinson Equation of State*. 2017. URL: https://www.vcalc.com/wiki/MichaelBartmess/Peng-Robinson+Equation+of+State.

[14] R.W.Dibble J. Warnatz U.Maas. *Combustion*. 2006. Chap. 6, pp. 73–90.

[15] R.W.Dibble J. Warnatz U.Maas. *Combustion*. 2006. Chap. 12, pp. 179–186.

[16] R.W.Dibble J. Warnatz U.Maas. *Combustion*. 2006. Chap. 9, pp. 129–140.

[17] J.D.Anderson. *MODERN COMPRESSIBLE FLOW*. 2013. Chap. 3, pp. 111–117.

[18] J.D.Anderson. *MODERN COMPRESSIBLE FLOW*. 2013. Chap. 5, pp. 191–230.

[19] White F. M. "Preliminary Concepts". In: *2nd ed., McGraw–Hill* (1991), pp. 29–32. URL: https://www.grc.nasa.gov/WWW/CEAWeb/TM-4647.pdf.

[20] Mohammad Reza Mobinipouya and Zahra Barzegar. "Calculation of Density for Refrigerant Mixtures in Sub Critical Regions for Use in the Buildings". In: *Engineering and Technology International Journal of Physical and Mathematical Sciences* 5.3 (). URL: https://zenodo.org/record/1062214/files/6066.pdf.

[21] *Monitoring Residuals*. 2009. URL: http://www.afs.enea.it/project/neptunius/docs/fluent/html/ug/node812.htm.

[22] *NASA Polynomial format for CHEMKIN-II*. 1999. URL: http://combustion.berkeley.edu/gri-mech/version30/files30/thermo30.dat.

[23] *Near-Wall Mesh Guidelines*. 2009. URL: http://www.afs.enea.it/project/neptunius/docs/fluent/html/ug/node410.htm.

[24] *Near-Wall Treatment*. 2009. URL: http://www.afs.enea.it/project/neptunius/docs/fluent/html/th/node98.htm.

[25] *Non-ideal behavior of gas*. 2019. URL: https://www.khanacademy.org/science/chemistry/gases-and-kinetic-molecular-theory/non-ideal-gas-behavior/a/non-ideal-behavior-of-gases.

[26] Zhukov V. P. and Feil M. "Numerical Simulations of Flame of Single Co-Axial Injector". In: *5th European Conference for Aerospace Sciences* (July 2017). URL: https://www.hindawi.com/journals/ijae/2017/5147606/.

[27] *Phase Diagrams*. 2019. URL: https://chem.libretexts.org/Bookshelves/Physical_and_Theoretical_Chemistry_Textbook_Maps/Supplemental_Modules_(Physical_and_Theoretical_Chemistry)/Physical_Properties_of_Matter/States_of_Matter/Phase_Transitions/Phase_Diagrams.

[28] T. J. Poinsot and D. P. Veynante. "Combustion". In: *Encyclopedia of Computational Mechanics* (2004). URL: http://www.cerfacs.fr/~cfdbib/repository/TR_CFD_04_122.pdf.

[29] *Pressure-Velocity Coupling*. 2009. URL: http://www.afs.enea.it/project/neptunius/docs/fluent/html/th/node373.htm.

[30] Rebeca Pupo. "Adiabatic Flame Temperature for Combustion of Methane". In: *Undergraduate Journal of Mathematical Modeling: One + Two* 3 (2011). URL: http://scholarcommons.usf.edu/cgi/viewcontent.cgi?article=4824&context=ujmm.

[31] Inc. Release 12.0 © ANSYS. *Overview of Flow Solvers*. 2009. URL: http://www.afs.enea.it/project/neptunius/docs/fluent/html/th/node360.htm.

[32] Inc. Release 12.0 © ANSYS. *Viscosity as a Function of Temperature*. 2009. URL: http://www.afs.enea.it/project/neptunius/docs/fluent/html/ug/node294.htm.

[33] Mike Schooley. *Fuel Propellants - Storable, and Hypergolic vs. Ignitable*. 1997. URL: https://www.permanent.com/space-transportation-propellants.html.

[34] *Specific turbulence dissipation rate*. 2011. URL: https://www.cfd-online.com/Wiki/Specific_turbulence_dissipation_rate.

[35] *SST*. 2019. URL: https://www.simscale.com/docs/content/simulation/model/turbulenceModel/kOmegaSST.html.

[36] *SST k-omega model*. 2019. URL: https://www.cfd-online.com/Wiki/SST_k-omega_model.

[37] Roger A. Svehla. "Transport Coefficients for the NASA Lewis Chemical Equilibrium Program". In: *NASA Technical Memorandum 4647* (Apr. 1995). URL: https://www.grc.nasa.gov/WWW/CEAWeb/TM-4647.pdf.

[38] *The Aungier-Redlich-Kwong Real Gas Model*. 2009. URL: http://www.afs.enea.it/project/neptunius/docs/fluent/html/ug/node335.htm.

[39] *The Generalized Finite-Rate Formulation for Reaction Modeling*. 2009. URL: http://www.afs.enea.it/project/neptunius/docs/fluent/html/th/node129.htm.

[40] Victor P. Zhukov. "Computational Fluid Dynamics Simulations of GO2/GH2 Single Element Combustor". In: *Journal of Propulsion and Power* (2015). URL: https://arc.aiaa.org/doi/abs/10.2514/1.B35654.

[41] Victor P. Zhukov and Klaus P. Heinrich. "Evaluation of the grid convergence for a rocket combustion chamber with a porous injector". In: *Acta Astronautica* (). URL: https://www.sciencedirect.com/science/article/pii/S0094576518302844.